Evidence of electron neutrino appearance in a muon neutrino beam

K. Abe,[47] N. Abgrall,[14] H. Aihara,[46,*] T. Akiri,[11] J. B. Albert,[11] C. Andreopoulos,[45] S. Aoki,[25] A. Ariga,[2] T. Ariga,[2] S. Assylbekov,[9] D. Autiero,[30] M. Barbi,[39] G. J. Barker,[54] G. Barr,[35] M. Bass,[9] M. Batkiewicz,[15] F. Bay,[13] S. W. Bentham,[27] V. Berardi,[20] B. E. Berger,[9] S. Berkman,[4] I. Bertram,[27] D. Beznosko,[33] S. Bhadra,[58] F. d. M. Blaszczyk,[29] A. Blondel,[14] C. Bojechko,[51] S. Boyd,[54] D. Brailsford,[19] A. Bravar,[14] C. Bronner,[26] D. G. Brook-Roberge,[4] N. Buchanan,[9] R. G. Calland,[28] J. Caravaca Rodríguez,[17] S. L. Cartwright,[43] R. Castillo,[17] M. G. Catanesi,[20] A. Cervera,[18] D. Cherdack,[9] G. Christodoulou,[28] A. Clifton,[9] J. Coleman,[28] S. J. Coleman,[8] G. Collazuol,[22] K. Connolly,[55] L. Cremonesi,[38] A. Curioni,[13] A. Dabrowska,[15] I. Danko,[37] R. Das,[9] S. Davis,[55] M. Day,[40] J. P. A. M. de André,[12] P. de Perio,[49] G. De Rosa,[21] T. Dealtry,[45,35] S. Dennis,[54,45] C. Densham,[45] F. Di Lodovico,[38] S. Di Luise,[13] J. Dobson,[19] O. Drapier,[12] T. Duboyski,[38] F. Dufour,[14] J. Dumarchez,[36] S. Dytman,[37] M. Dziewiecki,[53] M. Dziomba,[55] S. Emery,[6] A. Ereditato,[2] L. Escudero,[18] A. J. Finch,[27] E. Frank,[2] M. Friend,[16,†] Y. Fujii,[16,†] Y. Fukuda,[31] A. Furmanski,[54] V. Galymov,[6] A. Gaudin,[51] S. Giffin,[39] C. Giganti,[36] K. Gilje,[33] T. Golan,[57] J. J. Gomez-Cadenas,[18] M. Gonin,[12] N. Grant,[27] D. Gudin,[24] D. R. Hadley,[54] A. Haesler,[14] M. D. Haigh,[54] P. Hamilton,[19] D. Hansen,[37] T. Hara,[25] M. Hartz,[58,49] T. Hasegawa,[16,†] N. C. Hastings,[39] Y. Hayato,[47,*] C. Hearty,[4,‡] R. L. Helmer,[50] M. Hierholzer,[2] J. Hignight,[33] A. Hillairet,[51] A. Himmel,[11] T. Hiraki,[26] S. Hirota,[26] J. Holeczek,[44] S. Horikawa,[13] K. Huang,[26] A. K. Ichikawa,[26] K. Ieki,[26] M. Ieva,[17] M. Ikeda,[26] J. Imber,[33] J. Insler,[29] T. J. Irvine,[48] T. Ishida,[16,†] T. Ishii,[16,†] S. J. Ives,[19] K. Iyogi,[47] A. Izmaylov,[24,18] A. Jacob,[35] B. Jamieson,[56] R. A. Johnson,[8] J. H. Jo,[33] P. Jonsson,[19] K. K. Joo,[7] C. K. Jung,[33,*] A. Kaboth,[19] H. Kaji,[48] T. Kajita,[48,*] H. Kakuno,[46] J. Kameda,[47] Y. Kanazawa,[46] D. Karlen,[51,50] I. Karpikov,[24] E. Kearns,[3,*] M. Khabibullin,[24] F. Khanam,[9] A. Khotjantsev,[24] D. Kielczewska,[52] T. Kikawa,[26] A. Kilinski,[32] J. Y. Kim,[7] J. Kim,[4] S. B. Kim,[42] B. Kirby,[4] J. Kisiel,[44] P. Kitching,[1] T. Kobayashi,[16,†] G. Kogan,[19] A. Kolaceke,[39] A. Konaka,[50] L. L. Kormos,[27] A. Korzenev,[14] K. Koseki,[16,†] Y. Koshio,[47] K. Kowalik,[32] I. Kreslo,[2] W. Kropp,[5] H. Kubo,[26] Y. Kudenko,[24] S. Kumaratunga,[50] R. Kurjata,[53] T. Kutter,[29] J. Lagoda,[32] K. Laihem,[41] A. Laing,[48] M. Laveder,[22] M. Lawe,[43] M. Lazos,[28] K. P. Lee,[48] C. Licciardi,[39] I. T. Lim,[7] T. Lindner,[50] C. Lister,[54] R. P. Litchfield,[54,26] A. Longhin,[22] G. D. Lopez,[33] L. Ludovici,[23] M. Macaire,[6] L. Magaletti,[20] K. Mahn,[50] M. Malek,[19] S. Manly,[40] A. Marchionni,[13] A. D. Marino,[8] J. Marteau,[30] J. F. Martin,[49] T. Maruyama,[16,†] J. Marzec,[53] P. Masliah,[19] E. L. Mathie,[39] V. Matveev,[24] K. Mavrokoridis,[28] E. Mazzucato,[6] N. McCauley,[28] K. S. McFarland,[40] C. McGrew,[33] T. McLachlan,[48] M. Messina,[2] C. Metelko,[45] M. Mezzetto,[22] P. Mijakowski,[32] C. A. Miller,[50] A. Minamino,[26] O. Mineev,[24] S. Mine,[5] A. Missert,[8] M. Miura,[47] L. Monfregola,[18] S. Moriyama,[47,*] Th. A. Mueller,[12] A. Murakami,[26] M. Murdoch,[28] S. Murphy,[13,14] J. Myslik,[51] T. Nagasaki,[26] T. Nakadaira,[16,†] M. Nakahata,[47,*] T. Nakai,[34] K. Nakajima,[34] K. Nakamura,[16,†] S. Nakayama,[47] T. Nakaya,[26,*] K. Nakayoshi,[16,†] D. Naples,[37] T. C. Nicholls,[45] C. Nielsen,[4] M. Nirkko,[2] K. Nishikawa,[16,†] Y. Nishimura,[48] H. M. O'Keeffe,[35] Y. Obayashi,[47] R. Ohta,[16,†] K. Okumura,[48] T. Okusawa,[34] W. Oryszczak,[52] S. M. Oser,[4] M. Otani,[26] R. A. Owen,[38] Y. Oyama,[16,†] M. Y. Pac,[10] V. Palladino,[21] V. Paolone,[37] D. Payne,[28] G. F. Pearce,[45] O. Perevozchikov,[29] J. D. Perkin,[43] Y. Petrov,[4] E. S. Pinzon Guerra,[58] P. Plonski,[53] E. Poplawska,[38] B. Popov,[36,§] M. Posiadala,[52] J.-M. Poutissou,[50] R. Poutissou,[50] P. Przewlocki,[32] B. Quilain,[12] E. Radicioni,[20] P. N. Ratoff,[27] M. Ravonel,[14] M. A. M. Rayner,[14] M. Reeves,[27] E. Reinherz-Aronis,[9] F. Retiere,[50] A. Robert,[36] P. A. Rodrigues,[40] E. Rondio,[32] S. Roth,[41] A. Rubbia,[13] D. Ruterbories,[9] R. Sacco,[38] K. Sakashita,[16,†] F. Sánchez,[17] E. Scantamburlo,[14] K. Scholberg,[11,*] J. Schwehr,[9] M. Scott,[19] D. I. Scully,[54] Y. Seiya,[34] T. Sekiguchi,[16,†] H. Sekiya,[47] D. Sgalaberna,[13] M. Shibata,[16,†] M. Shiozawa,[47,*] S. Short,[19] Y. Shustrov,[24] P. Sinclair,[19] B. Smith,[19] R. J. Smith,[35] M. Smy,[5,*] J. T. Sobczyk,[57] H. Sobel,[5,*] M. Sorel,[18] L. Southwell,[27] P. Stamoulis,[18] J. Steinmann,[41] B. Still,[38] A. Suzuki,[25] K. Suzuki,[26] S. Y. Suzuki,[16,†] Y. Suzuki,[47,*] T. Szeglowski,[44] M. Szeptycka,[32] R. Tacik,[39,50] M. Tada,[16,†] S. Takahashi,[26] A. Takeda,[47] Y. Takeuchi,[25,*] H. A. Tanaka,[4,‡] M. M. Tanaka,[16,†] M. Tanaka,[16,†] I. J. Taylor,[33] D. Terhorst,[41] R. Terri,[38] L. F. Thompson,[43] A. Thorley,[28] S. Tobayama,[4] W. Toki,[9] T. Tomura,[47] Y. Totsuka,[‖] C. Touramanis,[28] T. Tsukamoto,[16,†] M. Tzanov,[29] Y. Uchida,[19] K. Ueno,[47] A. Vacheret,[35] M. Vagins,[5,*] G. Vasseur,[6] T. Wachala,[9] A. V. Waldron,[35] C. W. Walter,[11,*] D. Wark,[45,19] M. O. Wascko,[19] A. Weber,[45,35] R. Wendell,[47] R. J. Wilkes,[55] M. J. Wilking,[50] C. Wilkinson,[43] Z. Williamson,[35] J. R. Wilson,[38] R. J. Wilson,[9] T. Wongjirad,[11] Y. Yamada,[16,†] K. Yamamoto,[34] C. Yanagisawa,[33,¶] S. Yen,[50] N. Yershov,[24] M. Yokoyama,[46,*] T. Yuan,[8] A. Zalewska,[15] L. Zambelli,[36] K. Zaremba,[53] M. Ziembicki,[53] E. D. Zimmerman,[8] M. Zito,[6] and J. Żmuda[57]

(T2K Collaboration)

[1]*Department of Physics, Centre for Particle Physics, University of Alberta, Edmonton, Alberta, Canada*
[2]*Albert Einstein Center for Fundamental Physics, Laboratory for High Energy Physics (LHEP), University of Bern, Bern, Switzerland*
[3]*Department of Physics, Boston, Boston University, Massachusetts, USA*
[4]*Department of Physics and Astronomy, University of British Columbia, Vancouver, British Columbia, Canada*
[5]*Irvine, Department of Physics and Astronomy, University of California, Irvine, California, USA*
[6]*IRFU, CEA Saclay, Gif-sur-Yvette, France*
[7]*Institute for Universe & Elementary Particles, Chonnam National University, Gwangju, Korea*
[8]*Department of Physics, University of Colorado at Boulder, Boulder, Colorado, USA*
[9]*Department of Physics, Colorado State University, Fort Collins, Colorado, USA*
[10]*Department of Physics, Dongshin University, Naju, Korea*
[11]*Department of Physics, Duke University, Durham, North Carolina, USA*
[12]*Ecole Polytechnique, Laboratoire Leprince-Ringuet, IN2P3-CNRS, Palaiseau, France*
[13]*ETH Zurich, Institute for Particle Physics, Zurich, Switzerland*
[14]*Section de Physique, DPNC, University of Geneva, Geneva, Switzerland*
[15]*H. Niewodniczanski Institute of Nuclear Physics PAN, Cracow, Poland*
[16]*High Energy Accelerator Research Organization (KEK), Tsukuba, Ibaraki, Japan*
[17]*Institut de Fisica d'Altes Energies (IFAE), Bellaterra (Barcelona), Spain*
[18]*IFIC (CSIC & University of Valencia), Valencia, Spain*
[19]*Department of Physics, Imperial College London, London, United Kingdom*
[20]*Dipartimento Interuniversitario di Fisica, INFN Sezione di Bari and Università e Politecnico di Bari, Bari, Italy*
[21]*Dipartimento di Fisica, INFN Sezione di Napoli and Università di Napoli, Napoli, Italy*
[22]*Dipartimento di Fisica, INFN Sezione di Padova and Università di Padova, Padova, Italy*
[23]*INFN Sezione di Roma and Università di Roma "La Sapienza", Roma, Italy*
[24]*Institute for Nuclear Research of the Russian Academy of Sciences, Moscow, Russia*
[25]*Kobe University, Kobe, Japan*
[26]*Department of Physics, Kyoto University, Kyoto, Japan*
[27]*Physics Department, Lancaster University, Lancaster, United Kingdom*
[28]*Department of Physics, University of Liverpool, Liverpool, United Kingdom*
[29]*Department of Physics and Astronomy, Louisiana State University, Baton Rouge, Louisiana, USA*
[30]*IPN Lyon (IN2P3), Université de Lyon, Université Claude Bernard Lyon 1, Villeurbanne, France*
[31]*Department of Physics, Miyagi University of Education, Sendai, Japan*
[32]*National Centre for Nuclear Research, Warsaw, Poland*
[33]*Department of Physics and Astronomy, State University of New York at Stony Brook, Stony Brook, New York, USA*
[34]*Department of Physics, Osaka City University, Osaka, Japan*
[35]*Department of Physics, Oxford University, Oxford, United Kingdom*
[36]*Laboratoire de Physique Nucléaire et de Hautes Energies (LPNHE), CNRS/IN2P3, UPMC, Université Paris Diderot, Paris, France*
[37]*Department of Physics and Astronomy, University of Pittsburgh, Pittsburgh, Pennsylvania, USA*
[38]*School of Physics and Astronomy, Queen Mary University of London, London, United Kingdom*
[39]*Department of Physics, Regina, University of Regina, Saskatchewan, Canada*
[40]*Department of Physics and Astronomy, University of Rochester, Rochester, New York, USA*
[41]*III. Physikalisches Institut, RWTH Aachen University, Aachen, Germany*
[42]*Department of Physics and Astronomy, Seoul National University, Seoul, Korea*
[43]*Department of Physics and Astronomy, University of Sheffield, Sheffield, United Kingdom*
[44]*Institute of Physics, University of Silesia, Katowice, Poland*
[45]*STFC, Rutherford Appleton Laboratory, Harwell Oxford, and Daresbury Laboratory, Warrington, United Kingdom*
[46]*Department of Physics, University of Tokyo, Tokyo, Japan*
[47]*Institute for Cosmic Ray Research, University of Tokyo, Kamioka Observatory, Kamioka, Japan*
[48]*Institute for Cosmic Ray Research, Research Center for Cosmic Neutrinos, University of Tokyo, Kashiwa, Japan*
[49]*Department of Physics, University of Toronto, Toronto, Ontario, Canada*
[50]*TRIUMF, Vancouver, British Columbia, Canada*
[51]*Department of Physics and Astronomy, University of Victoria, Victoria, British Columbia, Canada*
[52]*Faculty of Physics, University of Warsaw, Warsaw, Poland*
[53]*Institute of Radioelectronics, Warsaw University of Technology, Warsaw, Poland*
[54]*Department of Physics, University of Warwick, Coventry, United Kingdom*
[55]*Department of Physics, University of Washington, Seattle, Washington, USA*

[56]Department of Physics, University of Winnipeg, Winnipeg, Manitoba, Canada
[57]Faculty of Physics and Astronomy, Wroclaw University, Wroclaw, Poland
[58]Department of Physics and Astronomy, York University, Toronto, Ontario, Canada
(Received 4 April 2013; published 5 August 2013)

The T2K Collaboration reports evidence for electron neutrino appearance at the atmospheric mass splitting, $|\Delta m^2_{32}| \approx 2.4 \times 10^{-3}$ eV^2. An excess of electron neutrino interactions over background is observed from a muon neutrino beam with a peak energy of 0.6 GeV at the Super-Kamiokande (SK) detector 295 km from the beam's origin. Signal and background predictions are constrained by data from near detectors located 280 m from the neutrino production target. We observe 11 electron neutrino candidate events at the SK detector when a background of 3.3 ± 0.4(syst) events is expected. The background-only hypothesis is rejected with a p value of 0.0009 (3.1σ), and a fit assuming $\nu_\mu \rightarrow \nu_e$ oscillations with $\sin^2 2\theta_{23} = 1$, $\delta_{CP} = 0$ and $|\Delta m^2_{32}| = 2.4 \times 10^{-3}$ eV^2 yields $\sin^2 2\theta_{13} = 0.088^{+0.049}_{-0.039}$(stat + syst).

DOI: 10.1103/PhysRevD.88.032002 PACS numbers: 14.60.Pq, 14.60.Lm, 25.30.Pt, 29.40.Ka

I. INTRODUCTION

The phenomena of neutrino oscillations through the mixing of massive neutrinos have been well established by experiments observing neutrino interaction rates from solar [1–7], atmospheric [8–13], reactor [14] and accelerator [15–18] sources. With few exceptions, such as the results from the LSND [19] and MiniBooNE collaborations [20], the observations are consistent with the mixing of three neutrinos, governed by three mixing angles: $\theta_{12} \approx 34°$, $\theta_{23} \approx 45°$ and θ_{13}; and an as-yet-undetermined CP-violating phase, δ_{CP}. Neutrino mixing also depends on three mass states, m_i, and therefore two independent mass splittings, $|\Delta m^2_{32}| \approx 2.4 \times 10^{-3}$ eV^2 (atmospheric) and $\Delta m^2_{21} \approx 7.6 \times 10^{-5}$ eV^2 (solar), where $\Delta m^2_{ij} = m^2_i - m^2_j$. Additional understanding of neutrino mixing can be gained by observing the appearance of one flavor of neutrino interactions in a beam of another flavor through charged current interactions. Recently, T2K [21] has reported on the appearance of electron neutrinos in a beam of muon neutrinos, and the OPERA [22] and Super-Kamiokande [23] collaborations have reported on the appearance of tau neutrinos from accelerator-based and atmospheric muon neutrino sources, respectively.

The oscillations of $\nu_\mu \rightarrow \nu_e$ that T2K searches for are of particular interest since the observation of this mode at a baseline over energy ratio (L/E) of $\sim$1 GeV/500 km implies a nonzero value for the mixing angle θ_{13}. Until recently, the mixing angle θ_{13} had only been constrained to be less than 11° by reactor [24] and accelerator [25,26] neutrino experiments. With data collected through 2011, the T2K experiment found the first indication of nonzero θ_{13} in the oscillation of muon neutrinos to electron neutrinos [21]. Since then, a nonzero value of $\theta_{13} = 9.1° \pm 0.6°$ [27] has been confirmed from the disappearance of reactor electron antineutrinos observed by the Daya Bay [28], RENO [29] and Double Chooz [30] experiments. In this paper, T2K updates its measurement of electron neutrino appearance using additional data collected through 2012 and improved analysis methods.

The probability for electron neutrino appearance in a muon neutrino beam with energy E_ν of $\mathcal{O}(1)$ GeV propagating over a baseline L of $\mathcal{O}(100)$ km is dominated by the term (in units of c, $\hbar = 1$):

$$P_{\nu_\mu \rightarrow \nu_e} \approx \sin^2\theta_{23} \sin^2 2\theta_{13} \sin^2 \frac{\Delta m^2_{32} L}{4E_\nu}. \quad (1)$$

This leading term is identical for neutrino and antineutrino oscillations. Since the probability depends on $\sin^2\theta_{23}$, a precise determination of θ_{13} requires measurements of θ_{23}. The dependence on $\sin^2\theta_{23}$ can lift the degeneracy of solutions with $\theta_{23} > \pi/4$ and $\theta_{23} < \pi/4$ that are present when θ_{23} is measured from muon neutrino survival, which depends on $\sin^2 2\theta_{23}$.

The electron neutrino appearance probability also includes subleading terms which depend on δ_{CP} and terms that describe matter interactions [31]:

$$\begin{aligned} P_{\nu_\mu \rightarrow \nu_e} = & \frac{1}{(A-1)^2} \sin^2 2\theta_{13} \sin^2\theta_{23} \sin^2[(A-1)\Delta] \\ & - (+) \frac{\alpha}{A(1-A)} \cos\theta_{13} \sin 2\theta_{12} \sin 2\theta_{23} \sin 2\theta_{13} \\ & \times \sin\delta_{CP} \sin\Delta \sin A\Delta \sin[(1-A)\Delta] + \frac{\alpha}{A(1-A)} \\ & \times \cos\theta_{13} \sin 2\theta_{12} \sin 2\theta_{23} \sin 2\theta_{13} \\ & \times \cos\delta_{CP} \cos\Delta \sin A\Delta \sin[(1-A)\Delta] \\ & + \frac{\alpha^2}{A^2} \cos^2\theta_{23} \sin^2 2\theta_{12} \sin^2 A\Delta. \end{aligned} \quad (2)$$

Here $\alpha = \frac{\Delta m^2_{21}}{\Delta m^2_{32}} \ll 1$, $\Delta = \frac{\Delta m^2_{32} L}{4E_\nu}$ and $A = 2\sqrt{2} G_F N_e \frac{E_\nu}{\Delta m^2_{32}}$, where N_e is the electron density of Earth's crust. In the

*Also at Kavli IPMU, University of Tokyo, Kashiwa, Japan.
†Also at J-PARC Center.
‡Also at Institute of Particle Physics, Canada.
§Also at JINR, Dubna, Russia.
‖Deceased.
¶Also at BMCC/CUNY, New York, New York, USA.

three-neutrino paradigm CP violation can only occur when all three mixing angles, including θ_{13}, have nonzero values. The second term has a negative sign for neutrinos and a positive sign for antineutrinos and violates CP, which suggests the possibility of observing CP violation by measuring the difference in the electron neutrino appearance probabilities for neutrinos and antineutrinos. Since the CP-violating term can only appear in an appearance probability, a measurement of ν_e appearance, such as the one described in this paper, is an important milestone towards future searches for CP violation. The A dependence in the oscillation probability arises from matter effects and introduces a dependence on the sign of Δm^2_{32}. We refer to $\Delta m^2_{32} > 0$ as the normal mass hierarchy and $\Delta m^2_{32} < 0$ as the inverted mass hierarchy.

This paper is organized as follows. Section II is a brief overview of the T2K experiment and the data-taking periods. Section III summarizes the analysis method and components, including the flux (Sec. IV), neutrino interaction model (Sec. V) and near detector and far detector data samples (Secs. VI and VIII, respectively). The fit to near detector data, described in Sec. VII, is used to constrain the far detector rate and associated uncertainties. Finally, Sec. IX describes how the far detector ν_e sample is used to estimate $\sin^2 2\theta_{13}$.

II. EXPERIMENTAL OVERVIEW AND DATA COLLECTION

The T2K experiment [32] is optimized to observe electron neutrino appearance in a muon neutrino beam. We sample a beam of muon neutrinos generated at the J-PARC accelerator facility in Tokai-mura, Japan, at baselines of 280 m and 295 km from the neutrino production target. The T2K neutrino beam line accepts a 31 GeV/c proton beam from the J-PARC accelerator complex. The proton beam is delivered in 5 μs long spills with a period that has been decreased from 3.64 s to 2.56 s over the data-taking periods described in this paper. Each spill consists of 8 equally spaced bunches (a significant subset of the data was collected with 6 bunches per spill) that are $\sim$15 ns wide. The protons strike a 91.4 cm long graphite target, producing hadrons including pions and kaons, and positively charged particles are focused by a series of three magnetic horns operating at 250 kA. The pions, kaons and some muons decay in a 96 m long volume to produce a predominantly muon neutrino beam. The remaining protons and particles which have not decayed are stopped in a beam dump. A muon monitor situated downstream of the beam dump measures the profile of muons from hadron decay and monitors the beam direction and intensity.

We detect neutrinos at both near (280 m from the target) and far (295 km from the target) detectors. The far detector is the Super-Kamiokande (SK) water Cherenkov detector. The beam is aimed 2.5° (44 mrad) away from the target-to-SK axis to optimize the neutrino energy spectrum for the oscillation measurements. The off-axis configuration [33–35] takes advantage of the kinematics of pion decays to produce a narrow band beam. The angle is chosen so that the spectrum peaks at the first oscillation maximum, as shown in Fig. 1, maximizing the signal in the oscillation region and minimizing feed-down backgrounds from high energy neutrino interactions. This optimization is possible because the value of $|\Delta m^2_{32}|$ is already relatively well known.

The near detectors measure the properties of the beam at a baseline where oscillation effects are negligible. The on-axis INGRID detector [36,37] consists of 16 modules of interleaved scintillator/iron layers in a cross configuration centered on the nominal neutrino beam axis, covering ± 5 m transverse to the beam direction along the horizontal and vertical axes. The INGRID detector monitors the neutrino event rate stability at each module, and the neutrino beam direction using the profile of event rates across the modules.

The off-axis ND280 detector is a magnetized multipurpose detector that is situated along the same direction as SK. It measures the neutrino beam composition and energy spectrum prior to oscillations and is used to study neutrino interactions. The ND280 detector utilizes a 0.2 T magnetic field generated by the refurbished UA1/NOMAD magnet and consists of a number of subdetectors: side muon range

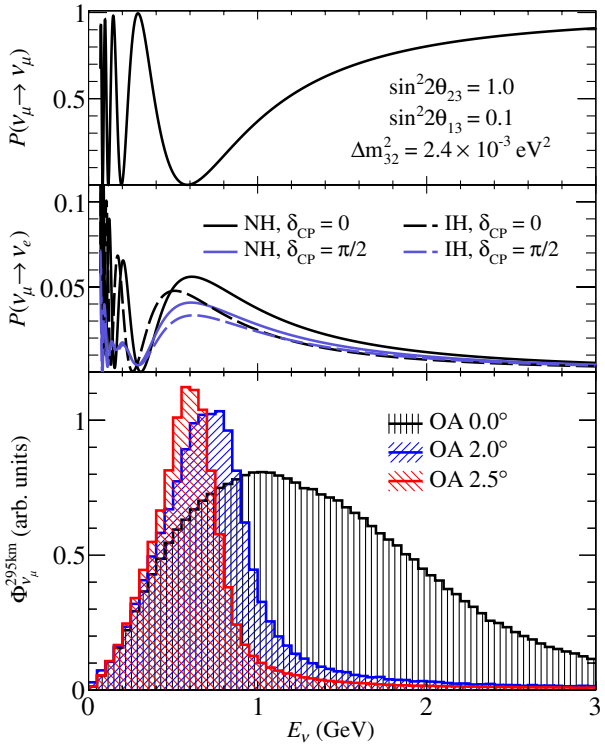

FIG. 1 (color online). The muon neutrino survival probability (top) and electron neutrino appearance probabilities (middle) at 295 km, and the unoscillated neutrino fluxes for different values of the off-axis angle (OA) (bottom). The appearance probability is shown for two values of the phase δ_{CP}, and for normal (NH) and inverted (IH) mass hierarchies.

detectors (SMRDs [38]), electromagnetic calorimeters (ECALs), a π^0 detector (P0D [39]) and a tracking detector. The tracking detector is composed of two fine-grained scintillator bar detectors (FGDs [40]) sandwiched between three gaseous time projection chambers (TPCs [41]). The first FGD primarily consists of polystyrene scintillator and acts as the target for most of the near detector neutrino interactions that are treated in this paper. Hence, neutrino interactions in the first FGD are predominantly on carbon nuclei. The ND280 detector is illustrated in Fig. 2, where the coordinate convention is also indicated. The x and z axes are in the horizontal plane, and the y axis is vertical. The origin is at the center of the magnet, and the magnetic field is along the x direction. The z axis is the direction to the far detector projected to the horizontal plane.

The SK far detector [42], as illustrated in Fig. 3, is a 50 kt water Cherenkov detector located in the Kamioka Observatory. The cylindrically shaped water tank is optically separated to make two concentric detectors: an inner detector (ID) viewed by 11129 inward-looking 20 inch photomultipliers, and an outer detector (OD) with 1885 outward-facing 8 inch photomultipliers. The fiducial volume is defined to be a cylinder whose surface is 2 m away from the ID wall, providing a fiducial mass of 22.5 kt. Cherenkov photons from charged particles produced in neutrino interactions form ring-shaped patterns on the detector walls, and are detected by the photomultipliers. The ring topology can be used to identify the type of particle and, for charged current interactions, the flavor of the neutrino that interacted. For example, electrons from electron neutrino interactions undergo large multiple scattering and induce electromagnetic showers, resulting in fuzzy ring patterns. In contrast, the heavier muons from

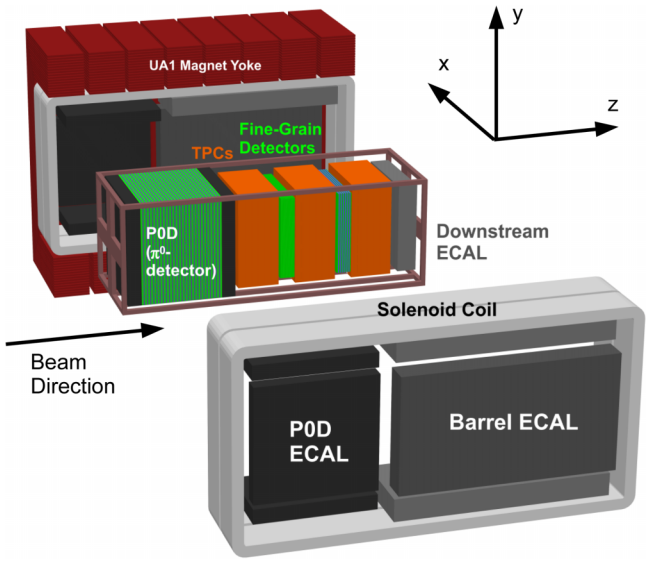

FIG. 2 (color online). An exploded illustration of the ND280 detector. The description of the component detectors can be found in the text.

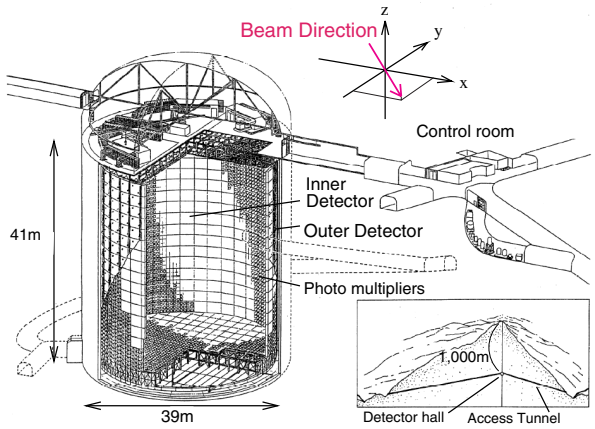

FIG. 3 (color online). An illustration of the SK detector.

muon neutrino interactions produce Cherenkov rings with sharp edges.

The T2K experiment uses a special software trigger to associate neutrino interactions in SK to neutrinos produced in the T2K beam. The T2K trigger records all the photomultiplier hits within ± 500 μs of the beam arrival time at SK. Beam timing information is measured spill-by-spill at J-PARC and immediately passed to the online computing system at SK. The time synchronization between the two sites is done using the Global Positioning System with <150 ns precision and is monitored with the common-view method [43]. Spill events recorded by the T2K triggers are processed offline to apply the usual SK software triggers used to search for neutrino events, and any candidate events found are extracted for further T2K data analysis. Spills used for the far detector data analysis are selected by beam and SK quality cuts. The primary reason spills are rejected at SK is due to the requirement that there are no events in the 100 μs before the beam window, which is necessary to reject decay electrons from cosmic-ray muons.

In this paper we present neutrino data collected during the three run periods listed in Table I. The total SK data set corresponds to 3.01×10^{20} protons on target (POT) or 4% of the T2K design exposure. About 50% of the data, the Run 3 data, were collected after T2K and J-PARC recovered from the 2011 Tohoku earthquake. A subset of data corresponding to 0.21×10^{20} POT from Run 3 was collected with the magnetic horns operating at 205 kA instead of the nominal value of 250 kA. The size of the total data

TABLE I. T2K data-taking periods and the integrated protons on target for SK data collected in those periods.

Run period	Dates	Integrated POT by SK
Run 1	Jan. 2010–Jun. 2010	0.32×10^{20}
Run 2	Nov. 2010–Mar. 2011	1.11×10^{20}
Run 3	Mar. 2012–Jun. 2012	1.58×10^{20}

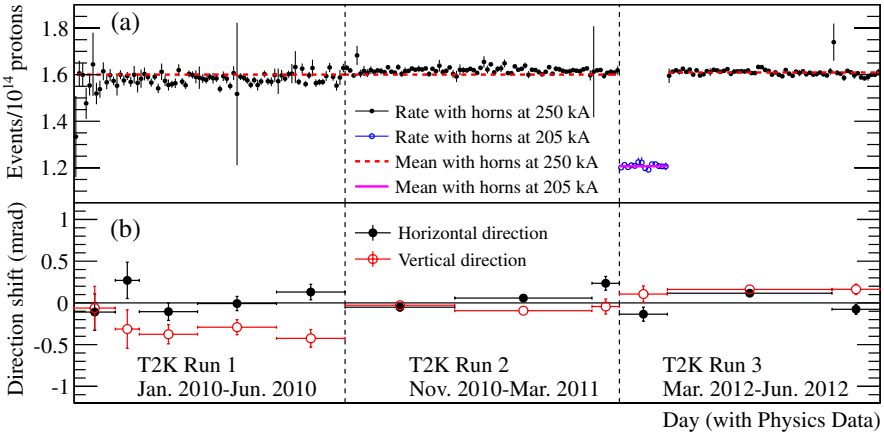

FIG. 4 (color online). The time dependence of the POT-normalized reconstructed neutrino event rate (a) and the beam direction (b) measured by INGRID. The error bars show the statistical uncertainty only. The points shown for the direction measurement include sequential data grouped in periods of stable beam conditions.

set is approximately two times that of T2K's previously published electron neutrino appearance result [21].

We monitor the rate and direction of the neutrino beam over the full data-taking period with the INGRID detector. As illustrated in Fig. 4, the POT-normalized neutrino event rate is stable to within 1%, and the beam direction is controlled well within the design requirement of 1 mrad, which corresponds to a 2% shift in the peak energy of the neutrino spectrum.

III. ANALYSIS OVERVIEW

We search for $\nu_\mu \rightarrow \nu_e$ oscillations via charged current quasielastic (CCQE) interactions of ν_e at SK. Since the recoil proton from the target nucleus is typically below Cherenkov threshold, these events are characterized by a single electronlike ring and no other activity. The most significant background sources are ν_e from muon and kaon decays that are intrinsic to the neutrino beam, and neutral current π^0 (NCπ^0) events where the detector response to the photons from the π^0 decay is consistent with a single electronlike ring. The selection of ν_e candidates is described in Sec. VIII.

We estimate the oscillation parameters and produce confidence intervals using a model that describes the probabilities to observe ν_e candidate events at SK in bins of electron momentum (magnitude and direction), as described in Sec. IX. The probabilities depend on the values of the oscillation parameters as well as many nuisance parameters that arise from uncertainties in neutrino fluxes, neutrino interactions, and detector response. The point where the likelihood is maximum for the observed data sample gives the oscillation parameter estimates, and the likelihood ratio at other points is used to construct confidence intervals on the parameters.

We model the neutrino flux with a data-driven simulation that takes as inputs measurements of the proton beam, hadron interactions and the horn fields [44]. The uncertainties on the flux model parameters arise largely from the uncertainties on these measurements. The flux model and its uncertainties are described in Sec. IV.

We model the interactions of neutrinos in the detectors assuming interactions on a quasifree nucleon using a dipole parametrization for vector and axial form factors. The nuclei are treated as a relativistic Fermi gas, and outgoing hadrons are subject to interactions in the nucleus, so-called "final state interactions." We validate the neutrino interaction model with comparisons to independent neutrino cross section measurements at $\mathcal{O}(1)$ GeV and pion scattering data. We set the uncertainties on the interaction model with comparisons of the model to data and alternate models. The neutrino interaction model and its uncertainties are described in Sec. V.

We further constrain the flux and interaction model parameters with a fit to samples of neutrino interaction candidates in the ND280 detector. Selections containing a negative muonlike particle provide high purity samples of ν_μ interactions, which constrain both the ν_μ flux that determines signal and NCπ^0 backgrounds at SK, and the intrinsic ν_e flux. In the energy range of interest, the intrinsic ν_e are predominantly produced from the decay chain $\pi^+ \rightarrow \mu^+ + \nu_\mu$, $\mu^+ \rightarrow e^+ + \nu_e + \bar{\nu}_\mu$, and to a lesser extent by three-body kaon decays. Hence, the ν_e flux is correlated with the ν_μ flux through the production of pions and kaons in the T2K beam line. The charged current interactions that make up most of the ND280 samples constrain the charged current interaction model. While ν_e interactions are indirectly constrained by ν_μ interactions, we also include uncertainties which account for differences between the ν_μ and ν_e cross section model. The ND280 neutrino interaction sample selection is described in Sec. VI, and the fit of the neutrino flux and interaction models to this data is described in Sec. VII.

IV. NEUTRINO FLUX MODEL

We simulate the T2K beam line to calculate the neutrino flux at the near and far detectors in the absence of neutrino oscillations, and this flux model is used as an input to predict neutrino interaction event rates at the detectors.

The flux simulation begins with the primary proton beam upstream of the collimator that sits in front of the T2K target. The interactions of particles in the target, beam line components, decay volume walls and beam dump, and their decays, are simulated. The simulation and its associated uncertainties are driven by measurements of the primary proton beam profile, measurements of the magnetic fields of the T2K horns, and hadron production data, including NA61/SHINE measurements [45,46]. First, we model the interactions of the primary beam protons and subsequently produced particles in the graphite target with a FLUKA 2008 [47,48] simulation. We pass any particles that exit the target into a GEANT3 [49] simulation that tracks particles through the magnetic horns and decay region, and decays hadrons and muons to neutrinos. The hadron interactions in the GEANT3 simulation are modeled with GCALOR [50]. To improve agreement between selected hadron interaction measurements and the simulation, we weight simulated events based on the stored information of the true initial and final state hadron kinematics for hadron interactions in events producing neutrinos.

The predicted flux at the SK and ND280 detectors, including systematic errors, is shown in Fig. 5. Here we describe the methods for weighting the flux and evaluating uncertainties based on proton beam measurements, hadron interaction data, alignment measurements, horn current and field measurements, and the beam direction measurement from the INGRID detector. More details of the flux calculation are described in Ref. [44].

A. Weighting and systematic error evaluation methods

To tune the flux model and study its uncertainties, adjustments are made by weighting events based on kinematics of the hadron interactions or the primary proton. The sensitivities to nuisance parameters that arise from such uncertainties as the hadron production model, proton beam profile, or horn currents, are evaluated by their effect on the predicted neutrino spectrum.

We use one of two approaches for each uncertainty source, depending on whether the uncertainty source has correlations that need to be treated. For error sources described by a number of correlated underlying parameters, we use weighting methods when possible. The nuisance parameters are sampled according to their covariance and the corresponding flux predictions for the k samples, ϕ^k, are calculated. A large number of parameters sets, N (typically 500 or more), are used to calculate the fractional covariance using:

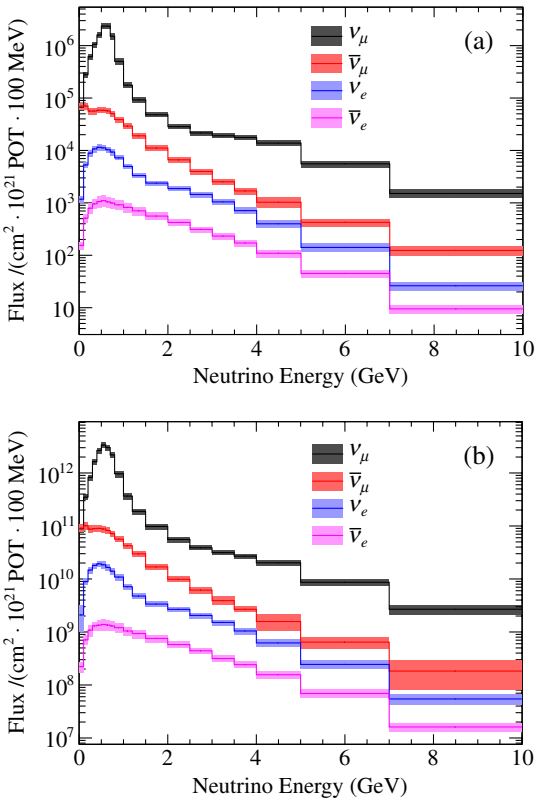

FIG. 5 (color online). The T2K flux prediction at SK (a) and ND280 (b) for neutrinos and antineutrinos with systematic error bars. The flux above $E_\nu = 10$ GeV is not shown; the flux is simulated up to $E_\nu = 30$ GeV.

$$v_{ij} = \frac{1}{N}\sum_{k=1}^{N}\frac{(\phi_i^{\mathrm{nom}} - \phi_i^k)(\phi_j^{\mathrm{nom}} - \phi_j^k)}{\phi_i^{\mathrm{nom}}\phi_j^{\mathrm{nom}}}. \tag{3}$$

Here ϕ_i^{nom} is the nominal flux prediction and i specifies a neutrino energy bin, flavor and detector at which the flux is evaluated. We evaluate hadron interaction and proton beam profile uncertainties with this method.

For systematic variations that cannot be treated by weighting simulated events, such as misalignment of beam line elements or changes to the horn currents, we produce new simulated event samples with $\pm 1\sigma$ variations of the nuisance parameters and calculate the fractional covariance matrix:

$$v_{ij} = \frac{1}{2}\frac{(\phi_i^{\mathrm{nom}} - \phi_i^+)(\phi_j^{\mathrm{nom}} - \phi_j^+)}{\phi_i^{\mathrm{nom}}\phi_j^{\mathrm{nom}}} + \frac{1}{2}\frac{(\phi_i^{\mathrm{nom}} - \phi_i^-)(\phi_j^{\mathrm{nom}} - \phi_j^-)}{\phi_i^{\mathrm{nom}}\phi_j^{\mathrm{nom}}}. \tag{4}$$

ϕ_i^+ and ϕ_i^- are the flux prediction for $+1\sigma$ and -1σ variations of the nuisance parameter. We evaluate horn and target alignment and horn current and field uncertainties with this method.

The total fractional flux covariance matrix is the sum of fractional flux covariance matrices calculated for each source of uncertainty. For the fits to data described in Secs. VII and IX, variations of the flux prediction are modeled with parameters b_i that scale the normalization of the flux in bins of neutrino energy and flavor at a given detector. The covariance matrix of the b_i, $(V_b)_{ij}$, is simply the total fractional flux covariance matrix described here. Since the b_i are separated for the near and far detectors, their covariances account for the correlations between the flux predictions at the two detectors. The covariances can therefore be used directly in simultaneous fits of near and far detector data or to calculate the uncertainty on the ratio of flux spectra at the two detectors.

The following sections describe each source of flux systematic uncertainty.

B. Proton beam monitoring and simulation

We simulate the proton beam according to the proton orbit and optics parameters measured by the proton beam position and profile monitors, and the number of protons measured by the intensity monitors. These monitors are described elsewhere [32,51]. We measure proton beam properties for each run period by reconstructing the beam profile at the upstream end of the collimator that sits before the T2K target for each beam spill. The sum of profiles for each beam spill, weighted by the number of protons, gives the proton beam profile that we input to the flux simulation. Table II summarizes the measured mean position, angle, emittance, Twiss α parameter [52] and width of the proton beam at the collimator, and their uncertainties for a typical run period. The largest contributions to the flux uncertainty from the proton beam simulation arise from the alignment uncertainties of the beam monitors.

The effect of the proton beam profile uncertainty on the flux is studied by varying the parameters in Table II within their uncertainties while accounting for the parameter correlations. The uncertainties on Y and Y' are dominant and are studied on a simulated "wide beam" flux sample that has a profile in the $y - y'$ (proton vertical position and angle) plane that covers the measured uncertainties. The wide beam sample is weighted for variations of Y and Y' and the effect on the flux is studied. The variations correspond to shifts in the off-axis angle of $\sim$0.35 mrad, or shifts in the off-axis spectrum peak of $\sim$10 MeV.

TABLE II. Summary of measured proton beam profile parameters and uncertainties at the collimator for a typical run period: mean position (X, Y) and angle (X', Y'), width (σ), emittance (ϵ), and Twiss parameter (α).

	X profile		Y profile	
Parameter	Central value	Error	Central value	Error
X, Y (mm)	0.00	0.35	−0.37	0.38
X', Y' (mrad)	0.03	0.07	0.07	0.28
σ (mm)	4.03	0.14	4.22	0.12
ϵ (π mm mrad)	4.94	0.54	6.02	3.42
α	0.33	0.08	0.34	0.41

C. Hadron production data, weighting and uncertainties

The pion and kaon differential production measurements we use to weight the T2K flux predictions are summarized in Table III.

We weight charged meson differential production multiplicities to the NA61/SHINE π^+/π^- [45] and K^+ [46] thin target production data, which covers most of phase space relevant for the off-axis flux. We use additional kaon differential production data from Eichten *et al.* [53] and Allaby *et al.* [54] to weight K^+ multiplicities in the phase space not covered by the NA61/SHINE measurements, and for K^- multiplicities. To estimate the uncertainty of pion production by secondary protons, we use differential pion production data from the BNL-E910 experiment [55] that were collected in interactions with proton beam energies less than the T2K primary proton beam energy.

We use measurements of the inelastic cross sections for proton, pion, and kaon beams with carbon and aluminum targets [56–66] to weight based on particle interaction and absorption rates in the flux prediction. In particular, NA61/SHINE measures the inclusive "production" cross section of 31 GeV/c protons on carbon: $\sigma_{\text{prod}} = 229.3 \pm 9.2$ mb [45]. The production cross section is defined as

$$\sigma_{\text{prod}} = \sigma_{\text{inel}} - \sigma_{\text{qe}}. \tag{5}$$

Here, σ_{qe} is the quasielastic scattering cross section, i.e. scattering off of individual bound nucleons that breaks up or excites the nucleus, but does not produce additional hadrons. The inclusive production cross section is used in the weighting of the flux prediction, and the quasielastic cross section is subtracted from measurements where necessary.

We apply hadron interaction-based weights to simulated events in two steps. The multiplicity of pions and kaons produced in interactions of nucleons on the target nuclei is defined as

$$\frac{dn}{dp}(p, \theta) = \frac{1}{\sigma_{\text{prod}}} \frac{d\sigma}{dp}(p, \theta). \tag{6}$$

Here p and θ are the momentum and angle relative to the incident particle of the produced particle in the lab frame.

TABLE III. Differential hadron production data relevant for the T2K neutrino flux predictions.

Experiment	Beam mom.	Target	Particles
NA61/SHINE [45,46]	31 GeV/c	C	$\pi^{\pm}$, K^+
Eichten *et al.* [53]	24 GeV/c	Be, Al, ...	p, $\pi^{\pm}$, $K^{\pm}$
Allaby *et al.* [54]	19.2 GeV/c	Be, Al, ...	p, $\pi^{\pm}$, $K^{\pm}$
BNL-E910 [55]	6.4–17.5 GeV/c	Be	$\pi^{\pm}$

We apply multiplicity weights that are the ratio of the measured and simulated differential multiplicities:

$$W(p,\theta) = \frac{[\frac{dn}{dp}(p,\theta)]_{\text{data}}}{[\frac{dn}{dp}(p,\theta)]_{\text{MC}}}. \quad (7)$$

We adjust the interaction rates of protons, charged pions and charged kaons as well, with weights that account for attenuation in the target:

$$W = \frac{\sigma'_{\text{prod}}}{\sigma_{\text{prod}}} e^{-x(\sigma'_{\text{prod}}-\sigma_{\text{prod}})\rho}. \quad (8)$$

Here ρ is the number density of nuclear targets in the material, σ_{prod} is the original inclusive production cross section in the simulation, σ'_{prod} is the inclusive production cross section to which the simulation is being weighted, and x is the distance traversed by the particle through the material. The total weight is the product of weights from all materials through which the particle propagates.

For pion and kaon production in secondary nucleon interactions, or in the phase space covered by the alternative kaon production data sets, we converted weights to an $x_F - p_T$ dependence, where p_T is the transverse momentum of the produced particle and x_F is the Feynman x [67] defined as

$$x_F = p_L / p_{\text{max}}. \quad (9)$$

Here p_L is the longitudinal momentum of the produced particle in the center of mass frame, and p_{max} is the maximum momentum the produced particle can have. We apply the $x_F - p_T$ dependent weights after converting simulated hadron interactions to the $x_F - p_T$ basis. This method assumes that the pion and kaon multiplicities expressed in the $x_F - p_T$ basis are independent of the collision center of mass energy.

The effect of the hadron interaction weighting on the SK ν_μ and ν_e flux are shown as the ratios of weighted to nominal flux in Fig. 6. The weighting of pion multiplicities is a 10% effect at low energy, while the weighting of kaon multiplicities affects the flux by as much as 40% in the high energy tail. The large weighting effect for kaons is due to the underestimation of kaon production above kaon momenta of 3 GeV/c in the simulation. The effect of the inclusive production cross section weighting on the flux prediction is less than 4% for all energies.

The uncertainties on the hadron multiplicity measurements contribute to the total uncertainty on the flux. Typical NA61/SHINE $\pi^\pm$ data points have ~7% systematic error, corresponding to a maximum uncertainty of 6% on the flux. In addition, we evaluate uncertainties on the x_F scaling assumption (less than 3%), and regions of the pion phase space not covered by data (less than 2%). The dominant source of uncertainty on the kaon production is the statistical uncertainty on the NA61/SHINE measurements.

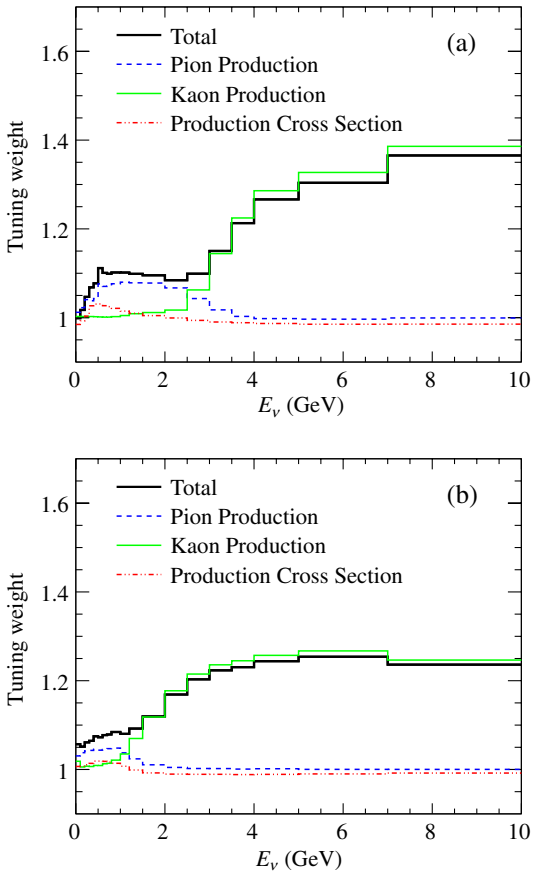

FIG. 6 (color online). Ratio of the hadron interaction weighted flux to the nominal flux for ν_μ (a), ν_e (b) flux predictions at SK. The effects of the pion production, kaon production and inclusive production cross section weighting are shown separately and in total.

The uncertainties on the inclusive production cross section measurements reflect the discrepancies that are seen between different measurements at similar incident particle energies. These discrepancies are similar in size to σ_{qe} and may arise from ambiguities in the actual quantity being measured by each experiment. We apply an uncertainty equal to the σ_{qe} component to the inclusive production cross section measurements (typically larger than the individual measurement errors), and the uncertainty propagated to the flux is less than 8% for all energies.

We apply an additional uncertainty to the production of secondary nucleons, for which no adjustments are made in the current flux prediction. The uncertainty is based on the discrepancy between the FLUKA modeling of secondary nucleon production and measurements by Eichten *et al.* [53] and Allaby *et al.* [54]. The uncertainty propagated to the flux is less than 10% for all energies.

The neutrino energy-dependent hadron interaction uncertainties on the SK ν_μ and ν_e flux predictions are summarized in Fig. 7, and represent the dominant source of uncertainty on the flux prediction.

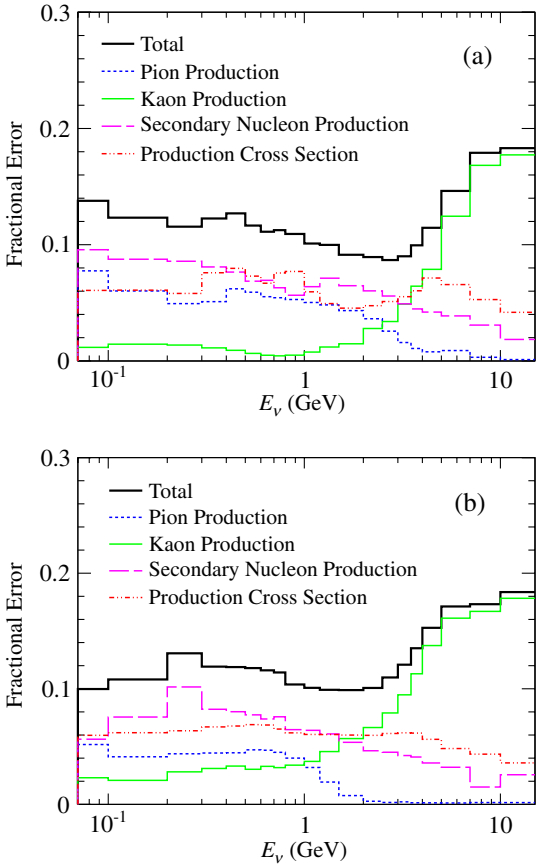

FIG. 7 (color online). The fractional hadron interaction errors on ν_μ (a), ν_e (b) flux predictions at SK.

D. Horn and target alignment and uncertainties

The horns are aligned relative to the primary beam line with uncertainties of 0.3 mm in the transverse x direction and 1.0 mm in the transverse y direction and beam direction. The precision of the horn angular alignment is 0.2 mrad. After installation in the first horn, both ends of the target were surveyed, and the target was found to be tilted from its intended orientation by 1.3 mrad. We have not included this misalignment in the nominal flux calculation, but the effect is simulated and included as an uncertainty. We also simulate linear and angular displacements of the horns within their alignment uncertainties and evaluate the effect on the flux. The total alignment uncertainty on the flux is less than 3% near the flux peak.

E. Horn current, field and uncertainties

We assume a $1/r$ dependence of the magnetic field in the flux simulation. The validity of this assumption is confirmed by measuring the horn field using a Hall probe. The maximum deviation from the calculated values is 2% for the first horn and less than 1% for the second and third horns. Inside the inner conductor of a spare first horn, we observe an anomalous field transverse to the horn axis with a maximum strength of 0.065 T. Flux simulations including the anomalous field show deviations from the nominal flux of up to 4%, but only for energies greater than 1 GeV.

The absolute horn current measurement uncertainty is 2% and arises from the uncertainty in the horn current monitoring. We simulate the flux with ± 5 kA variations of the horn current, and the effect on the flux is 2% near he peak.

F. Off-axis angle constraint from INGRID

The muon monitor indirectly measures the neutrino beam direction by detecting the muons from meson decays, while the INGRID on-axis neutrino detector directly measures the neutrino beam direction. The dominant source of uncertainty on the beam direction constraint is the systematic uncertainty on the INGRID beam profile measurement, corresponding to a 0.35 mrad uncertainty. We evaluate the effect on the flux when the SK or ND280 off-axis detectors are shifted in the simulation by 0.35 mrad.

G. Summary of flux model and uncertainties

The T2K flux predictions at the ND280 and SK detectors have been described and are shown in Fig. 5. We use the flux predictions as inputs to calculate event rates at both the ND280 and SK detectors. To evaluate the flux related uncertainties on the event rate predictions, we evaluate the fractional uncertainties on the flux prediction in bins of energy for each neutrino flavor. The bin edges are

(i) ν_μ: 0.0, 0.4, 0.5, 0.6, 0.7, 1.0, 1.5, 2.5, 3.5, 5.0, 7.0, 30.0 GeV
(ii) $\bar{\nu}_\mu$: 0.0, 1.5, 30.0 GeV
(iii) ν_e: 0.0, 0.5, 0.7, 0.8, 1.5, 2.5, 4.0, 30.0 GeV
(iv) $\bar{\nu}_e$: 0.0, 2.5, 30.0 GeV

We choose coarse binning for the antineutrino fluxes since they make a negligible contribution for the event samples described in this paper. The neutrino flux has finer bins around the oscillation maximum and coarser bins where the flux prediction uncertainties are strongly correlated.

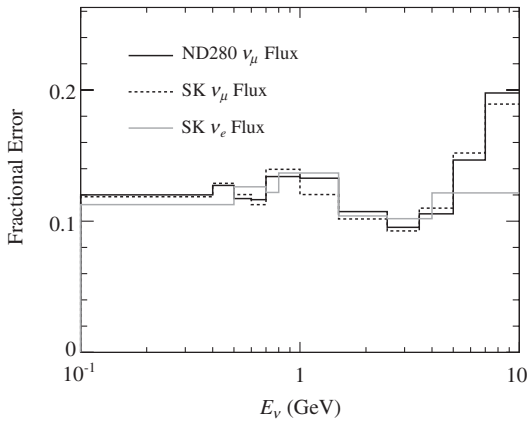

FIG. 8. The fractional uncertainties on the ND280 ν_μ, SK ν_μ and SK ν_e flux evaluated for the binning used in this analysis. This binning is coarser than the binning shown in Fig. 7 and includes the correlations between merged bins.

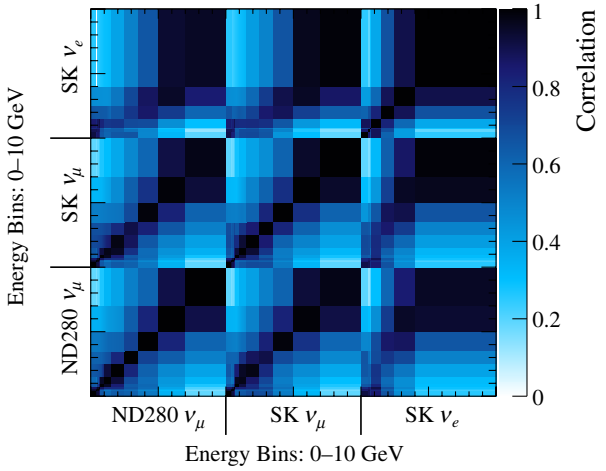

FIG. 9 (color online). The correlations of the flux uncertainties in the b_i bins for the ND280 ν_μ and SK ν_μ and ν_e fluxes. The axes are the bins in neutrino energy for each flavor/detector combination and are proportional to the neutrino energy up to 10 GeV.

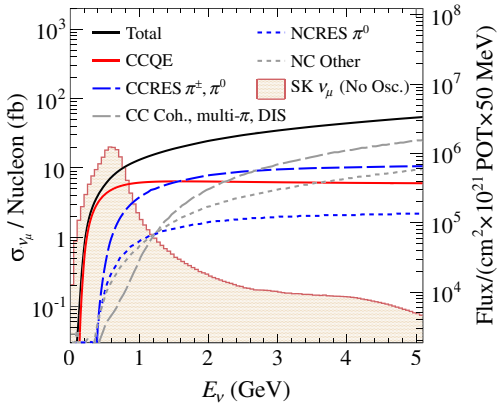

FIG. 10 (color online). The NEUT ν_μ interaction cross section per nucleon on ^{16}O with a breakdown by interaction process. The "NC Other" curve includes neutral current coherent pion production, resonant charged pion production, multipion production and deep inelastic scattering. The predicted ν_μ flux spectrum at SK with no oscillations is shown for comparison.

The uncertainties on the ND280 ν_μ, SK ν_μ and SK ν_e flux predictions are shown in Fig. 8 and the correlations are shown in Fig. 9. The correlations shown are evaluated for the binning described above. The ND280 ν_μ and SK ν_μ flux predictions have large correlations, indicating the ν_μ interaction rate at the near detector can constrain the unoscillated ν_μ interaction rate at the far detector. The SK ν_e flux is also correlated with the ND280 ν_μ flux, since the ν_μ and ν_e both originate from the $\pi \rightarrow \mu + \nu_\mu$ decay chain or kaon decays. This correlation also allows us to constrain the expected intrinsic ν_e rate at the far detector by measuring ν_μ interactions at the near detector.

V. NEUTRINO INTERACTION MODEL

We input the predicted neutrino flux at the ND280 and SK detectors to the NEUT [68] neutrino interaction generator to simulate neutrino interactions in the detectors. Figure 10 illustrates the neutrino-nucleon scattering processes modeled by NEUT at the T2K beam energies. The dominant interaction at the T2K beam peak energy is charged current quasielastic scattering:

$$\nu_\ell + N \rightarrow \ell + N', \tag{10}$$

where ℓ is the corresponding charged lepton associated with the neutrino's flavor (electron or muon), and N and N' are the initial and final state nucleons. Above the pion production threshold, single pion production contributes to charged current interactions (CC1π):

$$\nu_\ell + N \rightarrow \ell + N' + \pi, \tag{11}$$

and neutral current interactions (NC1π):

$$\nu + N \rightarrow \nu + N' + \pi. \tag{12}$$

In the high energy tail of the T2K flux, multipion and deep inelastic scattering (DIS) processes become dominant.

A. NEUT simulation models

CCQE interactions in NEUT are simulated using the model of Llewellyn Smith [69], with nuclear effects described by the relativistic Fermi gas model of Smith and Moniz [70,71]. Dipole forms for the vector and axial-vector form factors in the Llewellyn Smith model are used, with characteristic masses $M_V = 0.84$ GeV and $M_A = 1.21$ GeV, respectively, in the default simulation. The Fermi momentum p_F is set to 217 MeV/c for carbon and 225 MeV/c for oxygen, and the binding energy is set to 25 MeV for carbon and 27 MeV for oxygen.

NEUT simulates the production of pions via the excitation of hadronic resonances using the model of Rein and Sehgal [72]. The simulation includes 18 resonances below 2 GeV, along with interference terms. In the energy range relevant for T2K, resonance production is dominated by the $\Delta(1232)$. For 20% of the Δs produced within a nucleus, NEUT also simulates pionless Δ decay, in which the Δ deexcites in the nuclear medium without the emission of pions. NEUT includes the production of pions in coherent scattering of the neutrino on the target nucleus based on the Rein and Sehgal model.

Multipion and DIS interactions in NEUT are simulated using the GRV98 parton distribution functions [73]. Where the invariant mass of the outgoing hadronic system (W) is in the range $1.3 < W < 2.0$ GeV/c^2, a custom program is used [74], and only pion multiplicities of greater than one are considered to avoid double counting with the Rein and Sehgal model. For $W > 2.0$ GeV/c^2, PYTHIA/JETSET [75] is used. Corrections to the small Q^2 region developed by Bodek and Yang are applied [76].

NEUT uses a cascade model to simulate the interactions of hadrons as they propagate through the nucleus. For

pions with momentum below 500 MeV/c, the method of Salcedo *et al.* [77] is used. Above pion momentum of 500 MeV/c the scattering cross sections are modeled using measurements of $\pi^{\pm}$ scattering on free protons [78].

Additional details on the NEUT simulation can be found elsewhere [32].

B. Methods for varying the NEUT model

Uncertainties in modeling neutrino interactions are a significant contribution to the overall systematic uncertainty in the ν_e appearance analysis reported in this paper. In the rest of this section, we describe these uncertainties with nuisance parameters that vary the NEUT interaction models. The parameters, listed in Table IV, are chosen and their central values and uncertainties are set to cover the systematic uncertainties on the interaction models derived from comparisons of NEUT to external data or alternative models. They are a combination of free parameters in the NEUT model and *ad hoc* empirical parameters. The parameter values and uncertainties are further constrained by the fit to neutrino data from the T2K ND280 detector, as described in Sec. VII. To tune the NEUT model parameters and evaluate the effect of neutrino interaction uncertainties, adjustments are carried out by applying weights to simulated NEUT event samples from T2K or external experiments, such as MiniBooNE.

C. NEUT model comparisons to external data and tuning

A detailed description of the NEUT model tuning using external data comparisons can be found in the Appendix. Here we provide a brief summary.

1. FSI model tuning and uncertainty

The NEUT final state interaction (FSI) model includes parameters which alter the microscopic pion interaction probabilities in the nuclear medium. The central values of these parameters and their uncertainties are determined

TABLE IV. The parameters used to vary the NEUT cross section model and a brief description of each parameter.

CCQE cross section	
M_A^{QE}	The mass parameter in the axial dipole form factor for quasielastic interactions.
x_1^{QE}	The normalization of the quasielastic cross section for $E_\nu < 1.5$ GeV.
x_2^{QE}	The normalization of the quasielastic cross section for $1.5 < E_\nu < 3.5$ GeV.
x_3^{QE}	The normalization of the quasielastic cross section for $E_\nu > 3.5$ GeV.
Nuclear model for CCQE interactions (separate parameters for interactions on O and C)	
x_{SF}	Smoothly changes from a relativistic Fermi gas nuclear model to a spectral function model.
p_F	The Fermi surface momentum in the relativistic Fermi gas model.
Resonant pion production cross section	
M_A^{RES}	The mass parameter in the axial dipole form factor for resonant pion production interactions.
$x_1^{\mathrm{CC1}\pi}$	The normalization of the CC resonant pion production cross section for $E_\nu < 2.5$ GeV.
$x_2^{\mathrm{CC1}\pi}$	The normalization of the CC resonant pion production cross section for $E_\nu > 2.5$ GeV.
$x^{\mathrm{NC1}\pi^0}$	The normalization of the NC1π^0 cross section.
$x_{1\pi E_\nu}$	Varies the energy dependence of the 1π cross section for better agreement with MiniBooNE data.
W_{eff}	Varies the distribution of $N\pi$ invariant mass in resonant production.
$x_{\pi\text{-less}}$	Varies the fraction of Δ resonances that decay or are absorbed without producing a pion.
Other	
$x^{\mathrm{CC\ coh}}$	The normalization of CC coherent pion production.
$x^{\mathrm{NC\ coh}}$	The normalization of NC coherent pion production.
$x^{\mathrm{NC\ other}}$	The normalization of NC interactions other than NC1π^0 production.
$x_{\mathrm{CC\ other}}$	Varies the CCmulti-π cross section normalization, with a larger effect at lower energy.
$\vec{x}_{\mathrm{FSI}}$	Parameters that vary the microscopic pion scattering cross sections used in the FSI model.
x_{ν_e/ν_μ}	Varies the ratio of the CC ν_e and ν_μ cross sections.

from fits to pion scattering data [79–81]. We consider variations of the FSI parameters within the uncertainties from the fit of the pion scattering data, and evaluate the uncertainties on the predicted event rates for ND280 and SK selections.

2. CCQE model uncertainty

The most detailed measurement of CCQE scattering on light nuclei in the region of 1 GeV neutrino energy has been made by MiniBooNE, which has produced double-differential cross sections in the muon kinetic energy and angle $(T_\mu, \cos\theta_\mu)$ [82]. We compare the agreement of NEUT to the MiniBooNE CCQE data in addition to our own near detector measurement of CCQE events (Sec. VI) since the MiniBooNE detector has 4π acceptance, providing a kinematic acceptance of the leptons that more closely matches the SK acceptance for the selection described in Sec. VIII. This is illustrated in Fig. 11, which compares the predicted true Q^2 distributions for CCQE events in the ND280 CCQE selection, the MiniBooNE CCQE selection, and the SK selection for ν_e appearance candidates.

In order to allow the ND280 data to constrain the CCQE model, we use the difference of the NEUT nominal value and the best-fit value from fit to MiniBooNE data to set the uncertainty on M_A^{QE}, $\sigma_{M_A^{\mathrm{QE}}} = 0.43$ GeV. We also set the uncertainty on the low energy CCQE normalization, x_1^{QE}, to the size of the MiniBooNE flux uncertainty, 11%. The results of the MiniBooNE fit are discussed in more detail in the Appendix.

To allow for the discrepancy in CCQE cross section at $\mathcal{O}(1)$ GeV measured by MiniBooNE and at $\mathcal{O}(10)$ GeV measured by NOMAD [83], we employ independent CCQE normalization factors for $(1.5 < E_\nu < 3.5)$ GeV (x_2^{QE}) and $E_\nu > 3.5$ GeV (x_3^{QE}), each with a prior uncertainty of 30% and a nominal value of unity.

Alternate explanations have been proposed to reconcile the MiniBooNE data with a $M_A^{\mathrm{QE}} \approx 1.0$ GeV derived from electron scattering and NOMAD data [84–88]. These models typically modify the cross section either by enhancing the transverse component of the cross section, or by adding an additional multinucleon process to the existing cross section, where the neutrino interacts on a correlated pair of nucleons. Future improvements to the NEUT generator may include a full implementation of alternate CCQE models. However, these models would also require modifications to the kinematics of the exiting nucleons, but no consensus has been reached yet in the field as to how the nucleons should be treated. We consider two possible effects of alternate CCQE models on the ν_e appearance analysis. First, the effect in Q^2 for these models is often similar to increasing M_A^{QE} and [88] shows that other improvements to the CCQE cross section can be represented by an experiment-specific M_A^{QE} (effective), so the increase to the overall cross section from these models is approximately covered by the uncertainty on M_A^{QE}. Second, a multinucleon process would appear as a CCQE-like interaction in the SK detector, but the relationship between the neutrino energy and the lepton kinematics is different than for quasielastic scatters, which may affect the determination of oscillation parameters [89,90]. Other processes also appear CCQE-like and have a different relationship between lepton kinematics and neutrino energy, such as non-QE events with no pions in the final state (pionless Δ decay). The uncertainty on these events indirectly accounts for the effect of multinucleon models as these events affect the extracted oscillation parameters in a way similar to how multinucleon models would.

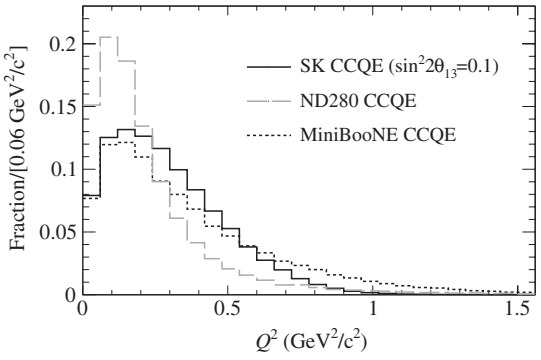

FIG. 11. The predicted Q^2 distributions for CCQE interactions in the ND280 CCQE selection, the MiniBooNE CCQE selection, and the SK ν_e appearance selection.

3. Single pion production model tuning and uncertainty

Measurements of single pion production cross sections on light nuclei in the T2K energy range have been made by MiniBooNE [91–93], and K2K, which used a 1000 ton water Cherenkov detector [94]. We perform a joint fit to the MiniBooNE measurements of charged current single π^+ production (CC1π^+), charged current single π^0 production (CC1π^0) and neutral current single π^0 production (NC1π^0). As shown in the Appendix, we compare the NEUT best-fit derived from the MiniBooNE single pion data with the K2K measurement, which is of particular interest since it is the same nuclear target as SK.

The parameters listed in Table V are varied in the fit to the MiniBooNE single pion data and their best-fit values and uncertainties are listed. The parameters include M_A^{RES}, the axial mass in the Rein and Sehgal model, the empirical parameter, W_{eff}, discussed in the next paragraph, and parameters that vary the normalization of various interaction modes. Contributions to the samples from CC multipion/DIS ($x_{\mathrm{CC\,other}}$) interactions, NC coherent interactions, NC1$\pi^\pm$ interactions and NC multipion/DIS interactions are relatively small, so the MiniBooNE samples have little power to constrain the associated parameters which are discussed in Sec. V C 4. Penalty terms for these parameters are applied using the prior uncertainties listed in Table V.

The W_{eff} parameter alters the single pion differential cross section as a function of pion-nucleon invariant mass W, providing a means to change the shape of the

TABLE V. Parameters used in the single pion fits, and their best-fit values and uncertainties. The 1σ value of the penalty term is shown for parameters which are penalized in the fit. Where parameters are defined in a manner consistent with the T2K data fits, the same parameter name is used.

	Nominal value	Penalty	Best-fit	Error
M_A^{RES} (GeV)	1.21		1.16	0.10
W_{eff}	1		0.48	0.14
$x_{\mathrm{CC\ other}}$	0	0.40	0.36	0.39
Normalizations:				
$x^{\mathrm{CC\ coh}}$	1		0.66	0.70
$x_1^{\mathrm{CC1}\pi}$	1		1.63	0.32
$x^{\mathrm{NC\ coh}}$	1	0.30	0.96	0.30
$x^{\mathrm{NC1}\pi^0}$	1		1.19	0.36
NC $1\pi^{\pm}$	1	0.30	0.98	0.30
NC multipion/DIS	1	0.30	0.99	0.30

NEUT prediction for NC$1\pi^0$ $\mathrm{d}\sigma/\mathrm{d}p_{\pi^0}$ differential cross section. Uncertainties in the NC$1\pi^0$ pion momentum distribution enter into the ν_e appearance analysis, as the momentum and angular distributions of ν_e candidates from NC$1\pi^0$ interactions depend on the kinematic distribution of the π^0. The NEUT predicted p_{π^0} spectrum, shown in the bottom plot of Fig. 12, is broader than the observed MiniBooNE data. A decrease to the W_{eff} parameter results in a more sharply peaked p_{π^0} spectrum, and achieves agreement between the NEUT prediction and the measured cross section; W_{eff} does not alter the total cross section. Future changes to the NEUT model that may eliminate the need for W_{eff} include refinements of the treatment of formation time effects, which have been shown to affect the pion momentum distribution [95], or modifications to the contribution of higher order resonances relative to $\Delta(1232)$.

The fitted data and NEUT model are shown in Fig. 12. We propagate the fitted parameter values for M_A^{RES}, $x_1^{\mathrm{CC1}\pi}$ and $x^{\mathrm{NC1}\pi^0}$ and their correlated uncertainties to the fits of ND280 and SK data. The remaining parameters from the fit to MiniBooNE data are marginalized. We evaluate additional uncertainties on these parameters by rerunning the fit to MiniBooNE data with variations of the FSI model and pionless Δ decay turned off. The deviations of the fitted parameter values due to these FSI or pionless Δ decay variations are applied as parameter uncertainties, increasing the uncertainties on M_A^{RES}, $x_1^{\mathrm{CC1}\pi}$ and $x^{\mathrm{NC1}\pi^0}$ to 0.11 GeV, 0.43 and 0.43, respectively. The fitted W_{eff} parameter value is not applied to the T2K predictions, but the difference between the nominal value of W_{eff} and the best-fit value from the MiniBooNE data fit is treated as an uncertainty.

An additional uncertainty in the energy-dependent pion production cross section is considered since we observe a discrepancy between the fitted NEUT model and the MiniBooNE CC$1\pi^+$ data, as shown in Fig. 13. We introduce a parameter $x_{1\pi E_\nu}$ that represents the energy-dependent tuning which brings the NEUT prediction into agreement with the MiniBooNE data. Uncertainties on the ND280 and SK predictions include the difference between the resonant pion production with and without this energy-dependent tuning.

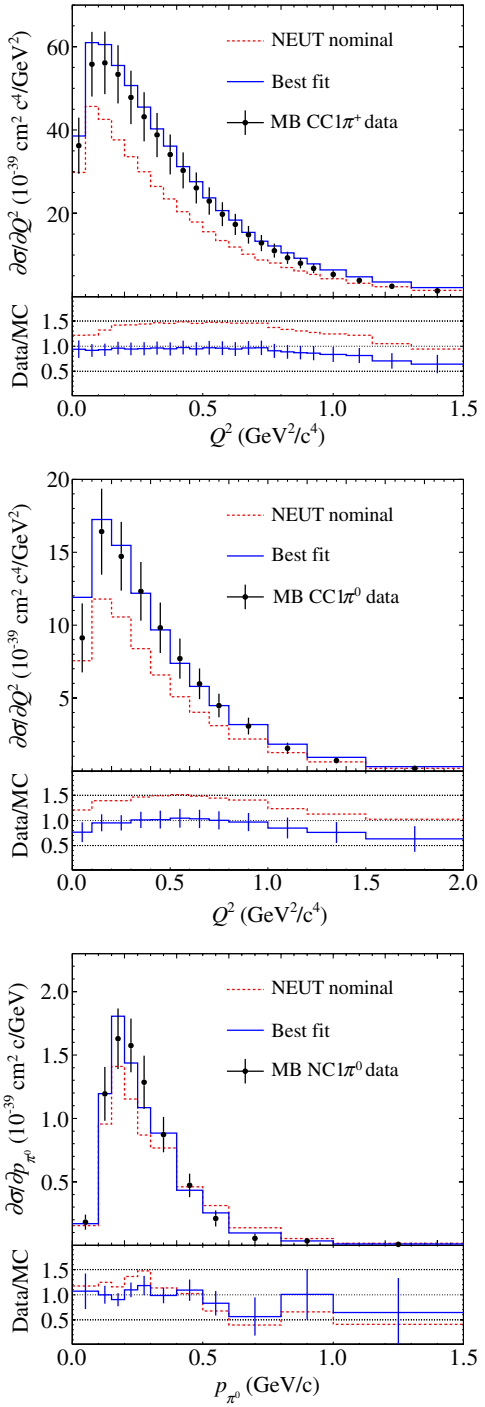

FIG. 12 (color online). Differential cross sections for CC$1\pi^+Q^2$ (top), CC$1\pi^0Q^2$ (middle) and NC$1\pi^0p_{\pi^0}$ (bottom) used in the single-pion fits to MiniBooNE data, and the NEUT nominal and best-fit predictions. The MiniBooNE data point errors are statistical + systematic.

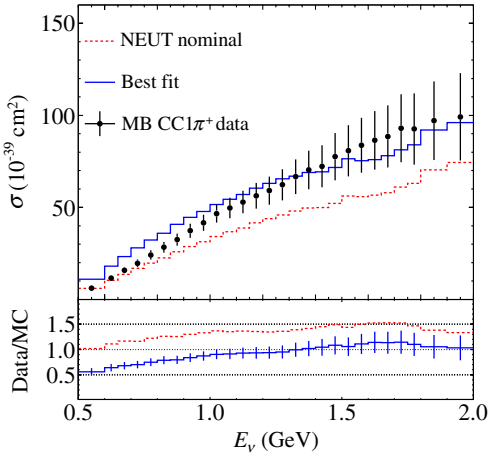

FIG. 13 (color online). The CC1π^+ cross section as a function of energy as measured by MiniBooNE, with the NEUT nominal and best-fit models. The treatment in the analysis of the disagreement between the best-fit NEUT and data is discussed in the text.

The fits to MiniBooNE data constrain the normalization of CC1π resonant production below 2.5 GeV. Above 2.5 GeV, we apply a separate normalization uncertainty of 40% on the parameter $x_2^{\mathrm{CC1}\pi}$. This uncertainty covers the maximum difference between MiniBooNE CC1π^+ data and NEUT at $E_\nu \approx 2$ GeV and is conservative given the CC inclusive cross section measurements [96] made at higher energies.

4. Other interaction channels

We evaluate the uncertainty on CC coherent pion production based on measurements by K2K [97] and SciBooNE [98] which place upper limits on the CC coherent production that are significantly less than the Rein and Sehgal model prediction. Since no clear CC coherent signal has been observed at $\mathcal{O}(1)$ GeV, we apply a 100% normalization uncertainty to the NEUT CC coherent pion production ($x^{\mathrm{CC\,coh}}$).

SciBooNE's measurement of the NC coherent pion cross section at $\mathcal{O}(1)$ GeV [99] is in good agreement with the Rein and Sehgal model prediction; the uncertainty on this channel is set to 30% based on the SciBooNE measurement and is represented by a normalization parameter, $x^{\mathrm{NC\,coh}}$. We define a single parameter $x^{\mathrm{NC\,other}}$ that varies the normalization of the NC resonant $\pi^\pm$, NC elastic and NC multipion/DIS/other resonant modes. The uncertainty on this normalization parameter is set to 30%. As there is little NC resonant $\pi^\pm$ data, the uncertainty on the NC resonant $\pi^\pm$ processes is set to be the same size as the agreement shown in Sec. V C 3 for the NC resonant 1π^0 cross section (30%). The NC multipion and DIS model was tuned to agree with the CC/NC data using the NEUT predicted CC DIS cross section; the uncertainties on this phenomenological model are set to cover the size of the uncertainties of the CC/NC data [100,101] (30%).

The CC multipion/DIS interactions contribute to the ND280 samples discussed in Sec. VI. At energies greater than 4 GeV, these modes dominate the inclusive cross section and are constrained by measurements of the inclusive cross section [102] with $\approx 10\%$ uncertainties. At lower energies the constraint from the inclusive cross section measurements is weaker since other interactions modes are significant. Hence, we apply an uncertainty that is 10% at high energies and increases to 40% near the threshold for multipion production. The model is adjusted by applying a weight:

$$w = 1 + \frac{x_{\mathrm{CC\,other}}}{E_\nu(\mathrm{GeV})}. \tag{13}$$

The parameter $x_{\mathrm{CC\,other}}$ is allowed to vary around a nominal value of 0 with a prior uncertainty of 0.4 GeV.

D. Nuclear model uncertainties

NEUT models nuclei with a relativistic Fermi gas model (RFG) using a Fermi momentum p_F from electron scattering data [103]. We evaluate the uncertainty on the CCQE cross section for variations of p_F within its uncertainty of 30 MeV/c. This uncertainty covers the uncertainty from the electron scattering data and has been inflated to cover possible discrepancies in the CCQE cross section at low Q^2. The uncertainty is applied independently for interactions on carbon and oxygen targets.

We also consider alternatives to the RFG model of the nuclei by making comparisons to a spectral function nuclear model implemented in the NuWro neutrino interaction generator [104]. The discrepancy in CCQE interactions models with the RFG and spectral function are assigned as uncertainty and represented by the parameter x_{SF} which smoothly varies the predicted lepton kinematics between the RFG ($x_{\mathrm{SF}} = 0$) and spectral function ($x_{\mathrm{SF}} = 1$) models. We apply the uncertainties for the nuclear model independently for carbon and oxygen cross sections.

E. ν_e cross section uncertainty

Differences between ν_μ and ν_e in the cross section are also considered, as the CC ν_μ sample at ND280 is used to infer the CC ν_e rate at the far detector. The spectral function uncertainty is calculated separately for ν_μ and ν_e as well as target material. In addition, an overall 3% uncertainty on the ratio of ν_μ and ν_e CC neutrino-nucleon cross sections (x_{ν_e/ν_μ}) is included, based on calculations [105] over T2K's energy range.

F. Summary of the neutrino cross section model, tuning and uncertainties

The cross section model parameters values and uncertainties are listed in Table VI. These priors are used as inputs to fits to the T2K ND280 and SK data sets, and include the results of the MiniBooNE single pion model fit.

TABLE VI. The parameters used to vary the NEUT cross section model along with the values used in the ND280 fit (input value) and uncertainties prior to the ND280 and SK data fits.

Parameter	Input value	Uncertainty
M_A^{QE} (GeV)	1.21	0.43
x_1^{QE}	1.00	0.11
x_2^{QE}	1.00	0.30
x_3^{QE}	1.00	0.30
x_{SF}	0.0	1.0
$p_F(^{12}\mathrm{C})$ (MeV/c)	217	30
$p_F(^{16}\mathrm{O})$ (MeV/c)	225	30
M_A^{RES} (GeV)	1.16	0.11
$x_1^{\mathrm{CC1}\pi}$	1.63	0.43
$x_2^{\mathrm{CC1}\pi}$	1.00	0.40
$x^{\mathrm{NC1}\pi^0}$	1.19	0.43
$x_{1\pi E_\nu}$	off	on
W_{eff}	1.0	0.51
$x_{\pi\text{-less}}$	0.2	0.2
$x^{\mathrm{CC\ coh}}$	1.0	1.0
$x^{\mathrm{NC\ coh}}$	1.0	0.3
$x^{\mathrm{NC\ other}}$	1.0	0.3
$x_{\mathrm{CC\ other}}$ (GeV)	0.0	0.4
x_{ν_e/ν_μ}	1.0	0.03

For parameters related to the nuclear modeling, such as x_{SF}, $p_F(^{12}\mathrm{C})$ and $p_F(^{16}\mathrm{O})$, we apply separate uncorrelated parameters for the modeling of interactions on $^{12}\mathrm{C}$ and $^{16}\mathrm{O}$. Hence, the fit to ND280 data does not constrain the nuclear modeling parameters used when modeling interactions at SK. Of the remaining parameters, we treat them as correlated for ND280 and SK if they are strongly constrained by ND280 data. These parameters include the CCQE cross section parameters, M_A^{QE}, x_1^{QE}, and the CC1π cross section parameters, M_A^{RES}, $x_1^{\mathrm{CC1}\pi}$. To preserve the correlations between NC and CC parameters from the fit to MiniBooNE single pion data, $x^{\mathrm{NC1}\pi^0}$ is also propagated. All other parameters are not well constrained by the ND280 data and are applied separately for ND280 and SK interaction modeling.

VI. ND280 NEUTRINO DATA

We select samples of CC ν_μ interactions in the ND280 detector, which are fitted to constrain the flux and cross section models, as described in Sec. VII. CC ν_μ interaction candidates are divided into two selections, one enhanced in CCQE-like events, and the second consisting of all other CC interactions, which we refer to as the CCnonQE-like selection. While the ν_e flux and interaction models are constrained by the CC ν_μ data, we also select a sample enhanced in CC ν_e interactions to directly verify the modeling of the intrinsic ν_e rate.

A. ND280 simulation

The ND280 detector response is modeled with a GEANT4-based [106,107] Monte Carlo (MC) simulation, using the neutrino flux described in Sec. IV and the NEUT simulation. The MC predictions presented in this section are not calculated with the cross section parameter tuning described in Table V. Neutrino interactions are generated up to 30 GeV for all flavors from the unoscillated flux prediction, with a time distribution matching the beam bunch structure. The ND280 subdetectors and magnet are represented with a detailed geometrical model. To properly represent the neutrino flux across a wider range of off-axis angles, a separate simulation is run to model neutrino interactions in the concrete and sand which surround ND280. The scintillator detectors, including the FGD, use custom models of the scintillator photon yield, photon propagation including reflections and attenuation, and electronics response and noise. The gaseous TPC detector simulation includes the gas ionization, transverse and longitudinal diffusion of the electrons, propagation of the electrons to the readout plane through the magnetic and electric field, and a parametrization of the electronics response. Further details of the simulation of the individual detectors of ND280 can be found in Refs. [32,40].

B. ν_μ candidate selection

We select CC ν_μ interactions by identifying the muons from $\nu_\mu N \rightarrow \mu^- X$ interactions, which may be accompanied by hadronic activity X from the same vertex. Of all negatively charged tracks, we identify the highest momentum track in each event that originates in the upstream FGD (FGD1) and enters the middle TPC (TPC2) as the μ^- candidate. The negatively charged track is identified using curvature and must start inside the FGD1 fiducial volume (FV) that begins 48 mm inward from the edges of FGD1 in x and y and 21 mm inward from the upstream FGD1 edge in z. In this analysis we use only selected tracks with a vertex in FGD1, since it provides a homogeneous target for neutrino interactions. To reduce the contribution from neutrino interactions upstream of the FGD1 FV, any tracks which pass through both the upstream TPC (TPC1) and FGD1 are rejected. This also has the consequence of vetoing backward-going particles from the CC interaction vertex, so the resulting selection is predominantly forward-going μ^-.

The μ^- candidate track energy loss is required to be consistent with a muon. The identification of particles (PID) is based on a truncated mean of measurements of energy loss in the TPC gas, from which a discriminator function is calculated for different particle hypotheses. We apply the discriminator to select muon candidates and reject electron and proton tracks. The TPC PID and TPC performance are described in more detail elsewhere [41].

Events passing the previously described cuts comprise the CC-inclusive sample, and the number of selected events and the MC predictions are listed in Table VII.

TABLE VII. Number of data and predicted events for the ND280 CC-inclusive selection criteria.

	Data	MC
Good negative track in FV	21503	21939
Upstream TPC veto	21479	21906
μ PID	11055	11498

These data correspond to 2.66×10^{20} POT. The predictions include a correction for the event pileup that is not directly modeled by the Monte Carlo simulation of the detector. The pileup correction takes into account the presence of neutrino interactions in the same beam bunch originating in the sand and material surrounding the detector. The size of this correction ranges between 0.5% and 1% for the different run periods. Of CC ν_μ interactions in the FGD1 FV, 47.6% are accepted by the CC-inclusive selection, and the resulting selection is 88.1% pure. The largest inefficiency of the CC-inclusive selection is from high angle particles which do not traverse a sufficient distance through the TPC to pass the selection criteria.

We divide the CC-inclusive ν_μ events into two mutually exclusive samples sensitive to different neutrino interaction types: CCQE-like and CCnonQE-like. As the CCQE neutrino interaction component typically has one muon and no pions in the final state, we separate the two samples by requiring the following for the CCQE-like events:

(i) only one muonlike track in the final state,
(ii) no additional tracks which pass through both FGD1 and TPC2,
(iii) no electrons from muon decay at rest in FGD1 (Michel electron).

A Michel electron will typically correspond to a stopped or low energy pion that decays to a muon which stops in FGD1, and is identified by looking for a time-delayed series of hits in FGD1. The Michel electron tagging efficiency is 59%. Events in the CC-inclusive selection which do not pass the CCQE-like selection comprise the CCnonQE-like sample. Example event displays for ND280 events are shown in Fig. 14.

The numbers of selected events in the data and nominal prediction for the CCQE-like and CCnonQE-like selections are shown in Table VIII. Table IX shows the composition of the CC, CCQE-like and CCnonQE-like selections according to the generated neutrino interaction categories in the Monte Carlo. The CCQE-like sample contains 40.0% of all CCQE interactions in the FGD1 FV, and CCQE interactions comprise 69.5% of the CCQE-like sample.

Figure 15 shows the distributions of events binned in the muon momentum (p_μ) and cosine of the angle between the muon direction and the z axis ($\cos\theta_\mu$) for both data and the prediction. In addition, we check the stability of the neutrino interaction rate with a Kolmogorov-Smirnov (KS) test of the accumulated data and find p values of 0.20, 0.12, and 0.79 for the CC-inclusive, CCQE-like and CCnonQE-like samples, respectively.

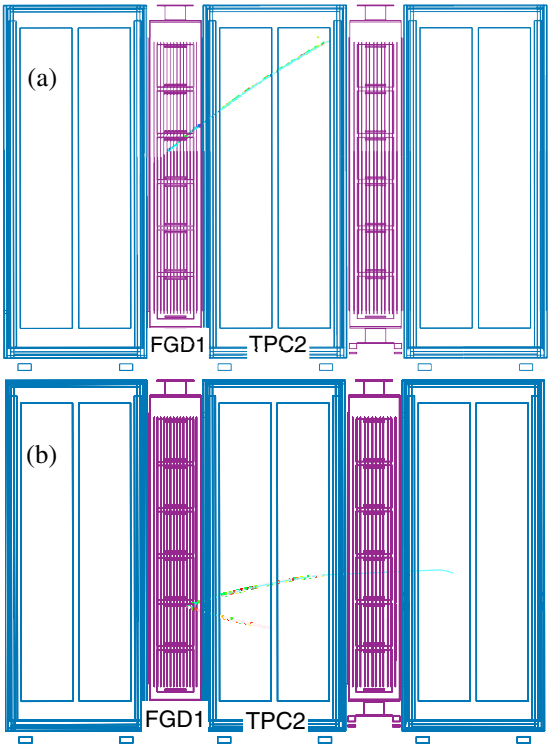

FIG. 14 (color online). Event displays of example ND280 CCQE-like (a) and CCnonQE-like (b) selected events.

Both CCQE-like and CCnonQE-like samples provide useful constraints on the neutrino flux and neutrino interaction models. The CCQE-like sample includes the dominant neutrino interaction process at the T2K beam peak energy (CCQE) and the CCnonQE-like sample is sensitive

TABLE VIII. Number of data and predicted events for the ND280 CCQE-like and CCnonQE-like selection criteria, after the CC-inclusive selection has been applied.

	CCQE-like		CCnonQE-like	
	Data	MC	Data	MC
TPC-FGD track	6238	6685	4817	4813
Michel electron	5841	6244	5214	5254

TABLE IX. Breakdown of the three ND280 CC samples by true interaction type as predicted by the MC simulation.

Event type	CC-inclusive	CCQE-like	CCnonQE-like
CCQE	44.4	69.5	14.7
CC resonant 1π	21.4	14.5	29.6
CC coherent π	2.8	1.7	4.0
All other CC	18.8	3.7	36.8
NC	3.0	1.3	5.1
$\bar{\nu}_\mu$	0.7	0.2	1.2
Out of FV	7.8	7.6	8.0
Sand interactions	1.1	1.6	0.5

to the high energy tail of the neutrino flux, where relatively few CCQE interactions occur. The fit of the flux and cross section models to these data, further described in Sec. VII, uses two-dimensional p_μ and $\cos\theta_\mu$ distributions for the CCQE-like and CCnonQE-like samples. We use a total of 20 bins per each sample, where p_μ is split into 5 bins and $\cos\theta_\mu$ is split into 4 bins. The data and the expected number of events for this binning are shown in Table X.

C. Detector response modeling uncertainties

We consider systematic uncertainties on the modeling of the detection efficiency and reconstruction of events which affect

(i) the overall efficiency for selecting CC interactions,
(ii) the reconstructed track properties $(p_\mu, \cos\theta_\mu)$,
(iii) the sample (either CCQE-like or CCnonQE-like) in which the event is placed.

We estimate uncertainties from each category with a variety of control samples that include beam data, cosmic events and simulated events.

The uncertainty on the efficiency for selecting CC ν_μ interactions is propagated from uncertainties on the data quality criteria applied to the tracks, track reconstruction and matching efficiencies, PID, and determination of the track curvature. We also consider the uncertainty on the detector mass.

The systematic uncertainty on the track momentum determination is from uncertainties on the magnetic field absolute value and field nonuniformity. Small imperfections in the magnetic and electric fields can affect the path of the drift electrons, causing a distorted image of the track and a possible bias in the reconstructed momentum. The size of these distortions is constrained from laser calibration data and MC simulations using magnetic field

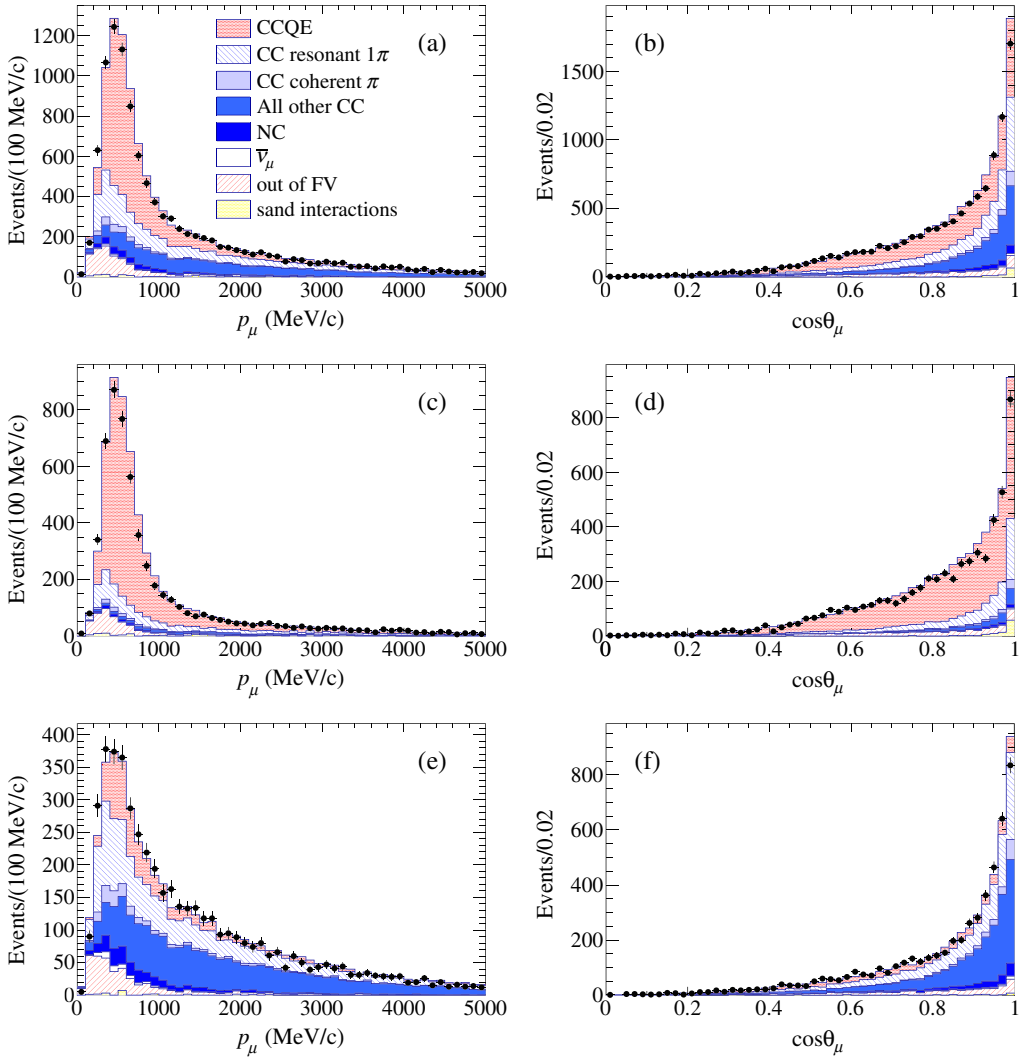

FIG. 15 (color online). Muon momentum for the CC-inclusive (a), CCQE-like (c), and CCnonQE-like (e) samples. Cosine of the muon angle for the CC-inclusive (b), CCQE-like (d), and CCnonQE-like (f) samples. The errors on the data points are the statistical errors.

TABLE X. Data (MC) p_μ and $\cos\theta_\mu$ events split in bins as used by the fit described in Sec. VII at ND280.

	p_μ (MeV/c)				
	0–400	400–500	500–700	700–900	>900
CCQE-like sample					
$-1 < \cos\theta_\mu \leq 0.84$	854 (807.7)	620 (655.6)	768 (821.2)	222 (255.0)	222 (233.0)
$0.84 < \cos\theta_\mu \leq 0.90$	110 (107.2)	110 (116.3)	235 (270.6)	133 (153.5)	159 (194.7)
$0.90 < \cos\theta_\mu \leq 0.94$	62 (69.1)	67 (74.0)	142 (179.0)	90 (121.4)	228 (274.6)
$0.94 < \cos\theta_\mu \leq 1.0$	92 (95.4)	73 (85.4)	184 (216.5)	160 (174.8)	1310 (1339.0)
CCnonQE-like sample					
$-1 < \cos\theta_\mu \leq 0.84$	560 (517.9)	262 (272.2)	418 (400.3)	256 (237.8)	475 (515.0)
$0.84 < \cos\theta_\mu \leq 0.90$	83 (80.3)	42 (35.8)	83 (80.2)	86 (74.8)	365 (389.8)
$0.90 < \cos\theta_\mu \leq 0.94$	46 (58.6)	37 (33.8)	60 (63.1)	39 (56.4)	462 (442.6)
$0.94 < \cos\theta_\mu \leq 1.00$	75 (76.6)	33 (43.2)	91 (93.4)	85 (87.2)	1656 (1694.7)

measurements made prior to detector installation. The overall momentum scale is determined from the magnitude of the magnetic field component transverse to the beam direction, B_x, which is inferred from the measured magnetic coil current. The momentum resolution is determined in data from studies of tracks which traverse multiple TPCs; the individual momentum calculated for a single TPC can be compared to the momentum determined by nearby TPCs to infer the momentum resolution in data and MC simulation.

The primary causes of event migration between the CCQE-like and CCnonQE-like samples are external backgrounds or interactions of pions. External backgrounds in the samples are due to three sources: cosmic rays, neutrino interactions upstream in the surrounding sand and concrete, and neutrino interactions in the ND280 detector outside the FV (out of FV). Interactions from the sand or concrete contribute to the number of tracks in the selected event, which can change a CCQE-like event to a CCnonQE-like event. Interactions that occur outside of the FGD1 FV are about 7.6% of the total selected CC-inclusive sample. Sources include neutrino interactions in FGD1 outside of the FV, or particles produced in interactions downstream of FGD1 that travel backwards to stop in the FGD1 FV. Pion absorption and charge exchange interactions in the FGD material can also reduce the probability that a charged pion produces a track in TPC2, affecting the identification of an event as CCQE-like or CCnonQE-like. The uncertainty on the GEANT4 modeling of pion inelastic scattering is evaluated by comparing the GEANT4 model to pion scattering data.

For each source of systematic uncertainty, we generate a 40×40 covariance matrix with entries for each pair of $(p_\mu, \cos\theta_\mu)$ bins. These matrices represent the fractional uncertainty on the predicted numbers of events in each $(p_\mu, \cos\theta_\mu)$ bin for each error source. The binning used is the same as that shown in Table X, where the first 20 bins correspond to the CCQE-like sample and the second 20 correspond to the CCnonQE-like sample. The total covariance matrix V_d is generated by linearly summing the covariance matrices for each of the systematic uncertainties. Figure 16 shows the bin-to-bin correlations from the covariance matrix, which displays the feature of anticorrelations between bins in the CCQE-like and CCnonQE-like samples arising from systematic error sources, such as the pion absorption uncertainty, that migrate simulated events between samples. Table XI summarizes the range of uncertainties across the $(p_\mu, \cos\theta_\mu)$ bins and the uncertainty on the total number of events.

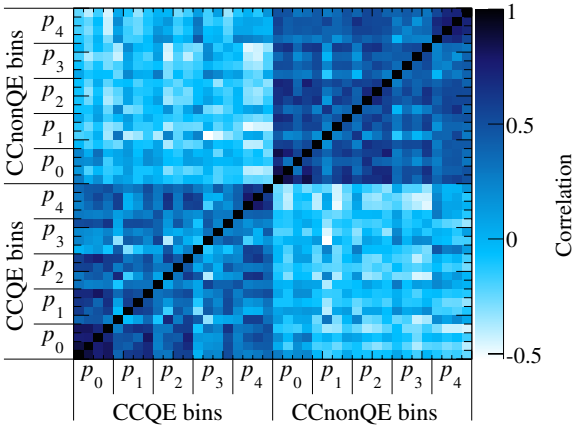

FIG. 16 (color online). The bin-to-bin correlation matrix from the systematic covariance matrix for the ν_μ selected sample at ND280. The bins are ordered by increasing $\cos\theta_\mu$ in groups of increasing muon momentum (p_0 to p_4) for the two selections.

TABLE XI. Minimum and maximum fractional errors among all the $(p_\mu, \cos\theta_\mu)$ bins, including the largest error sources. The last column shows the fractional error on the total number of events, taking into account the correlations between the $(p_\mu, \cos\theta_\mu)$ bins.

	Error Size (%)	
Systematic error	Minimum and maximum fractional error	Total fractional error
B-field distortions	0.3–6.9	0.3
Momentum scale	0.1–2.1	0.1
Out of FV	0–8.9	1.6
Pion interactions	0.5–4.7	0.5
All others	1.2–3.4	0.4
Total	2.1–9.7	2.5

D. Intrinsic ν_e candidate selection

We also select a sample of CC ν_e interactions to check the consistency of the predicted and measured intrinsic ν_e rates. The CC ν_μ selections described earlier provide the strongest constraint on the expected intrinsic ν_e rate, through the significant correlation of the ν_μ flux to the ν_e flux. However, a CC ν_e selection at the near detector provides a direct and independent measurement of the intrinsic ν_e rate.

We select CC ν_e interactions by applying the same criteria as described in Sec. VI B, except that the energy loss for the highest momentum negatively charged particle is required to be consistent with an electron instead of a muon, and interactions in FGD2 are used to increase the sample size. For electrons of momenta relevant to T2K, the energy loss is 30%–40% larger than for muons at the same momenta, and so electrons and muons are well separated since the TPC energy loss resolution is less than 8% [41]. In addition, for tracks which reach the downstream ECAL, we use the information from the ECAL to remove events in which the lepton candidate is consistent with a muon. A muon that crosses the ECAL produces a narrow track while an electron releases a large part of its energy, producing an electromagnetic shower. We developed a neural network to distinguish between tracklike and showerlike events. For this analysis we select only showerlike events.

The total number of selected events in the electron candidate sample is 927. The signal efficiency for selecting CC ν_e interactions in the FGD1 and FGD2 FV is 31.9% with an overall 23.7% purity. For higher momenta the relative purity of the selection increases (42.1% for $p_e > 300$ MeV/c).

The majority of selected ν_e are from kaon decay (80%). The dominant background events (78% of the total background) are low energy electrons produced by photon conversion in the FGDs, called the γ background. The photons come from π^0 decays, where the π^0s are generated in ν_μ interactions either in the FGD or in the material which surrounds the FGD. A total of 7% of the remaining background events are misidentified muons coming from ν_μ interactions. The probability for a muon to be misidentified as an electron is estimated to be less than 1% across most of the relevant momentum range. This probability is determined using a highly pure (>99%) sample of muons from neutrino-sand interactions. Finally, background not belonging to the two previous categories is mainly due to protons and pions produced in NC and CC ν_μ interactions in the FGD. Figure 17(a) shows the momentum distribution of the highest momentum track with negative charge for each event in the selected electron candidate sample.

We estimate the uncertainties on the detector response modeling for the electron candidate sample in the same manner as described in Sec. VI C, with additional uncertainties considered for the FGD2 interactions in the selection, and for electron-PID selection. The total detector response systematic uncertainty on the electron candidate sample is 5.7%, with the TPC PID (3.8%) uncertainty as the largest.

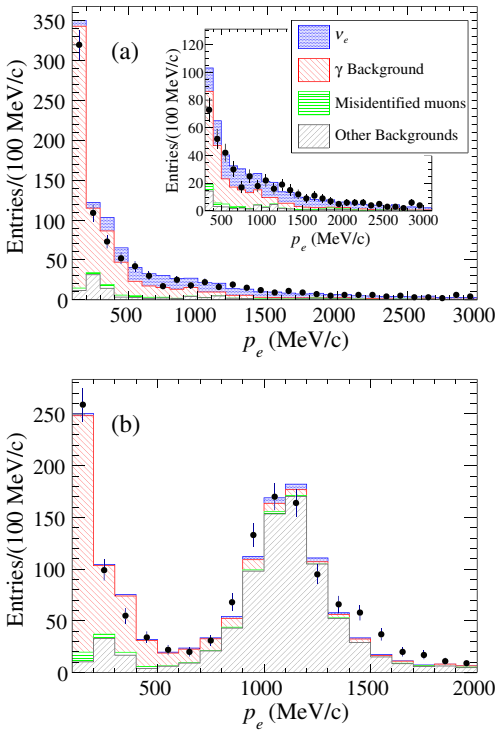

FIG. 17 (color online). (a) Momentum distribution of the highest momentum track with negative charge for each event in the electron candidate sample at ND280. The inset shows the region with momentum ≥ 300 MeV/c. (b) Momentum distribution of the highest momentum track with positive charge for each event of the positron candidate control sample. The "Other Backgrounds" component is mainly due to protons and pions from NC and CC ν_μ interactions in the FGD. The energy loss of positrons and protons (pions) is similar at $p \approx 1000$ MeV/c (200 MeV/c), resulting in the presence of these particles in the positron candidate sample.

The rate of intrinsic ν_e interactions is determined with a likelihood fit to reconstructed momenta of electron candidate events. To constrain the large background from photons, a control sample of positron (positive charge, electron PID tracks) candidates is used. Figure 17(b) shows the momentum distribution of candidate positrons. The sample is composed of positrons at lower energies and protons at higher energies. We simultaneously fit the electron and positron candidate samples to determine the photon background and ν_e signal rate normalizations. The misidentified muon background component is fixed according to the estimate from the pure muon control sample, and other smaller background sources are fixed according to the nominal predictions. Neutrino flux, neutrino cross section, and detector response uncertainties are included in the likelihood fit.

The inferred rate of CC ν_e events in data from the likelihood fit normalized by the prediction is $0.88 \pm 0.10(\text{stat}) \pm 0.15(\text{syst})$. The measured ν_e rate at the near detector is consistent with the prediction within systematic uncertainties. The neutrino flux and cross section systematic uncertainties are the dominant contributions to the total systematic error on the ν_e rate. In Sec. VII we show the ν_e rate after the flux and cross section parameters are tuned by the fit to the CC ν_μ data.

VII. ND280 CONSTRAINT ON THE NEUTRINO FLUX AND CROSS SECTION MODELS

The rate of neutrino interactions measured at the ND280 detector has power to constrain the neutrino flux and interaction models used to predict the ν_e candidate event rate at the SK detector. The predicted SK ν_e signal and neutral current background both depend directly on the unoscillated ν_μ flux, while the intrinsic ν_e background depends on the ν_e flux. As shown in Fig. 9, both the SK ν_μ and ν_e flux predictions are correlated to the ND280 ν_μ flux prediction through the underlying data and assumptions applied in the flux calculation. Both the SK ν_e signal and intrinsic ν_e background also depend on the charged current interaction model. Hence, a fit to the CC-inclusive events from ND280 can constrain flux and cross section nuisance parameters relevant to the SK prediction.

We fit the near detector CCQE-like and CCnonQE-like ν_μ data to determine tuned values of the ν_μ and ν_e flux parameters and cross section model parameters, described in Secs. IV and V, respectively. The fit includes the marginalization of nuisance parameters describing uncertainties in the simulation of the detector response and parameters describing parts of the neutrino interaction model that are not correlated for ND280 and SK selections. The tuned parameters are then applied to predict the ν_e signal and background interactions at SK. The fit also incorporates constraints on the flux and cross section models determined independently from the ND280 data constraint to properly propagate all constraints to the SK event rate predictions.

TABLE XII. Prior and fitted values and uncertainties of the propagated neutrino flux and cross section model parameters.

Parameter	Prior value	Fitted value
ν_μ 0.0–0.4 GeV	1.00 ± 0.12	0.98 ± 0.09
ν_μ 0.4–0.5 GeV	1.00 ± 0.13	0.99 ± 0.10
ν_μ 0.5–0.6 GeV	1.00 ± 0.12	0.98 ± 0.09
ν_μ 0.6–0.7 GeV	1.00 ± 0.13	0.93 ± 0.08
ν_μ 0.7–1.0 GeV	1.00 ± 0.14	0.84 ± 0.08
ν_μ 1.0–1.5 GeV	1.00 ± 0.12	0.86 ± 0.08
ν_μ 1.5–2.5 GeV	1.00 ± 0.10	0.91 ± 0.08
ν_μ 2.5–3.5 GeV	1.00 ± 0.09	0.95 ± 0.07
ν_μ 3.5–5.0 GeV	1.00 ± 0.11	0.98 ± 0.08
ν_μ 5.0–7.0 GeV	1.00 ± 0.15	0.99 ± 0.11
$\nu_\mu > 7.0$ GeV	1.00 ± 0.19	1.01 ± 0.15
$\bar{\nu}_\mu$ 0.0–1.5 GeV	1.00 ± 0.12	0.95 ± 0.10
$\bar{\nu}_\mu > 1.5$ GeV	1.00 ± 0.11	0.95 ± 0.10
ν_e 0.0–0.5 GeV	1.00 ± 0.13	0.96 ± 0.10
ν_e 0.5–0.7 GeV	1.00 ± 0.12	0.96 ± 0.10
ν_e 0.7–0.8 GeV	1.00 ± 0.14	0.96 ± 0.11
ν_e 0.8–1.5 GeV	1.00 ± 0.10	0.94 ± 0.08
ν_e 1.5–2.5 GeV	1.00 ± 0.10	0.97 ± 0.08
ν_e 2.5–4.0 GeV	1.00 ± 0.12	0.99 ± 0.09
$\nu_e > 4.0$ GeV	1.00 ± 0.17	1.01 ± 0.13
$\bar{\nu}_e$ 0.0–2.5 GeV	1.00 ± 0.19	0.97 ± 0.18
$\bar{\nu}_e > 2.5$ GeV	1.00 ± 0.14	1.02 ± 0.11
M_A^{QE} (GeV)	1.21 ± 0.45	1.33 ± 0.20
M_A^{RES} (GeV)	1.16 ± 0.11	1.15 ± 0.10
x_1^{QE}	1.00 ± 0.11	0.96 ± 0.09
$x_1^{\text{CC1}\pi}$	1.63 ± 0.43	1.61 ± 0.29
$x_1^{\text{NC1}\pi^0}$	1.19 ± 0.43	1.19 ± 0.40

A. ND280 likelihood

The fit maximizes a likelihood that includes the binned likelihood of the ND280 data and the prior constraints on the flux model, the interaction model, and the detector response model:

$$\mathcal{L}_{\text{ND}}(\vec{b}, \vec{x}, \vec{d}|N_i^d) = \pi_{\text{flux}}(\vec{b})\pi_{x\,\text{sec}}(\vec{x})\pi_{\text{det}}(\vec{d}) \times \prod_{i=1}^{N_{\text{bins}}} \frac{[N_i^p(\vec{b}, \vec{x}, \vec{d})]^{N_i^d} e^{-N_i^p(\vec{b},\vec{x},\vec{d})}}{N_i^d!}. \quad (14)$$

$\pi_{\text{flux}}(\vec{b})$, $\pi_{x\,\text{sec}}(\vec{x})$, $\pi_{\text{det}}(\vec{d})$ are multivariate normal distributions that are functions of the flux ($\vec{b}$), neutrino cross section ($\vec{x}$) and detector response ($\vec{d}$) nuisance parameters. These functions encode the prior constraints on the nuisance parameters and depend on the nominal parameter values and the parameter errors or covariance matrices described in previous sections. The likelihood includes the product of the Poisson probabilities for the $N_{\text{bins}} = 40$ bins of the CCQE-like and CCnonQE-like selections. For each bin the predicted number of events, $N_i^p(\vec{b}, \vec{x}, \vec{d})$, is evaluated based

on the values of the nuisance parameters, and compared to the measurement, N_i^d. To obtain fit results that more closely follow a χ^2 distribution [108], we define the likelihood ratio:

$$\mathcal{L}_{\text{ratio}} = \frac{\mathcal{L}_{\text{ND}}(\vec{b}, \vec{x}, \vec{d}|N_i^d)}{\mathcal{L}_{\text{ND}}(\vec{b}^0, \vec{x}^0, \vec{d}^0, N_i^p = N_i^d|N_i^d)}. \quad (15)$$

Here the denominator is the likelihood evaluated with N_i^p set equal to N_i^d and the nuisance parameters set to their nominal values: $\vec{b}^0 = 1$, $\vec{x}^0$, $\vec{d}^0 = 1$; both $\vec{b}$ and $\vec{d}$ have nominal values of 1. The quantity that is minimized is $-2\ln(\mathcal{L}_{\text{ratio}})$:

$$-2\ln(\mathcal{L}_{\text{ratio}}) = 2\sum_{i=1}^{N_{\text{bins}}} N_i^p(\vec{b}, \vec{x}, \vec{d}) - N_i^d + N_i^d \ln[N_i^d/N_i^p(\vec{b}, \vec{x}, \vec{d})] + \sum_{i=1}^{N_b}\sum_{j=1}^{N_b}(1_i - b_i)(V_b^{-1})_{i,j}(1 - b_j) + \sum_{i=1}^{N_x}\sum_{j=1}^{N_x}(x_i^0 - x_i)$$
$$\times (V_x^{-1})_{i,j}(x_j^0 - x_j) + \sum_{i=1}^{N_{\text{bins}}}\sum_{j=1}^{N_{\text{bins}}}(1 - d_i)(V_d(\vec{b}, \vec{x})^{-1})_{i,j}(1 - d_j) + \ln\left(\frac{|V_d(\vec{b}, \vec{x})|}{|V_d(\vec{b}^0, \vec{x}^0)|}\right). \quad (16)$$

The predicted number of events in each observable bin $N^p(\vec{b}, \vec{x}, \vec{d})$ depends on the value of the $\vec{b}, \vec{x} = (\vec{x}^{\text{norm}}, \vec{x}^{\text{resp}})$, and $\vec{d}$ nuisance parameters:

$$N_i^p = d_i \sum_j^{E_\nu\text{bins}} \sum_k^{\text{Int modes}} b_j x_k^{\text{norm}}(E_j) w_{i,j,k}(\vec{x}^{\text{resp}}) T_{i,j,k}^p. \quad (17)$$

The $T_{i,j,k}^p$ are the nominal Monte Carlo templates that predict the event rate for bins in the observables, i, true neutrino energy, j, and neutrino interaction modes, k. The $\vec{b}$ parameters multiply the flux prediction in bins of true neutrino energy. The detector response parameters, $\vec{d}$, multiply the expected number of events in each observable $(p_\mu, \cos\theta_\mu)$ bin. The $\vec{x}$ are included in the prediction in one of two ways. The x_k^{norm} are cross section parameters that multiply the neutrino cross section normalization for a given true neutrino energy bin and one of the k interaction modes. We model the effect of the remaining cross section parameters, $\vec{x}^{\text{resp}}$, with precalculated response functions, $w_{i,j,k}(\vec{x}^{\text{resp}})$, that have a value of 1 for the nominal parameter settings and can have a nonlinear dependence on the cross section parameters.

The remaining terms in Eq. (16) correspond to the prior constraints on the flux, cross section, and detector response models discussed in earlier sections. V_b is the prior fractional covariance matrix, corresponding to Figs. 8 and 9. The covariances of flux predictions at ND280 and SK are included so that the fit to ND280 data can constrain the SK flux parameters. The prior covariance matrix for the neutrino interaction parameters, V_x, is diagonal for most parameters with entries corresponding to the errors listed in

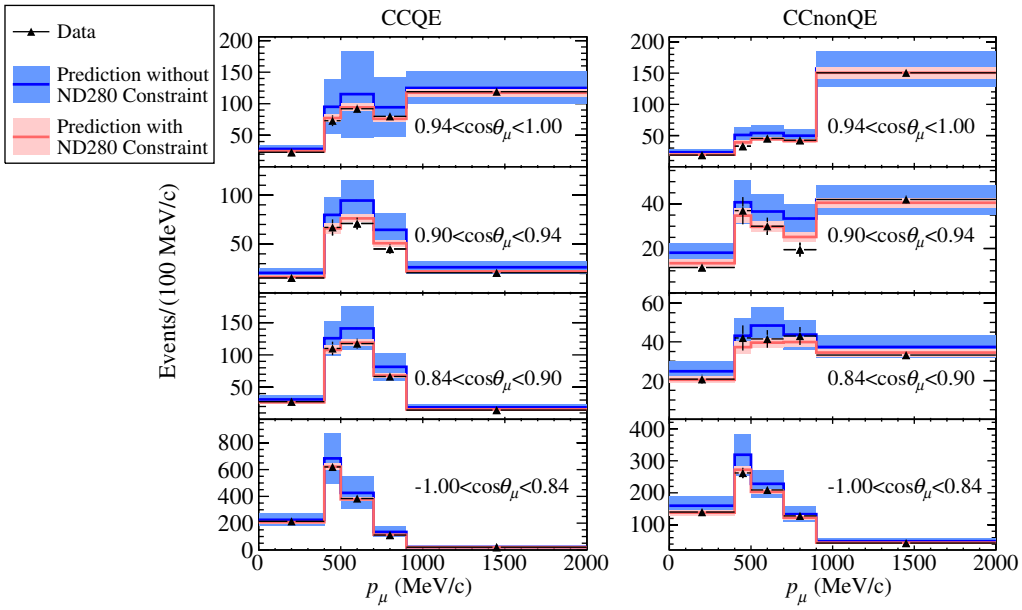

FIG. 18 (color online). The fitted p_μ, $\cos\theta_\mu$ bins from the ND280 CCQE-like (left) and CCnonQE-like (right) samples. All values in the plot are divided by the shown bin width. The $p_\mu > 900$ MeV/c bin additionally contains the overflow bin, and is normalized by a bin width of 1100 MeV/c. The prediction prior to the fit uses the modifications to the NEUT model parameters derived from fits of the MiniBooNE single pion data.

Table VI. Correlations are included for the parameters constrained by the fit to MiniBooNE single pion data. The V_d fractional covariance matrix, with correlations shown in Fig. 16, incorporates the simulated detector efficiency and reconstruction uncertainties, final state interaction errors and Monte Carlo statistical errors. The final term in the likelihood is present since the Monte Carlo statistical errors included in V_d depend on the $\vec{b}$ and $\vec{x}$ parameters through the weights applied to the simulated events. Since V_d is not constant, the determinant from the multivariate normal distribution, $\pi_{\rm det}(\vec{d})$, cannot be dropped from the $-2\ln(\mathcal{L}_{\rm ratio})$.

B. Parameter propagation and marginalization

This fitting method extrapolates the ND280 constraint on the neutrino flux and interaction model to the far detector prediction through the simultaneous variation of ND280 and SK flux parameters, and the constraint on the common interaction model parameters. After the $-2\ln(\mathcal{L}_{\rm ratio})$ is minimized, we apply a subset of the fitted parameter values to the calculation of the expected ν_e candidate rate at SK. The subset of parameters which is substantially constrained by the ND280 data sets and is also relevant to the event rate prediction at SK is listed in Table XII. Since the parameters are not used to calculate the predicted event rates at SK, the flux parameters for ND280, nuclear model-dependent cross section parameters and detector response systematic parameters are marginalized by integrating out their dependence in $-2\ln(\mathcal{L}_{\rm ratio})$ under the assumption of a quadratic dependence near the minimum. The remaining cross section parameters do not affect the SK event prediction substantially and these are also marginalized.

C. ND280 fit results

The resulting $(p_\mu, \cos\theta_\mu)$ distributions from the fit to the ND280 samples are shown in Fig. 18. We evaluate the postfit agreement between model and data by generating 2000 pseudoexperiments with statistical and systematic variations, and fitting them to obtain the minimum $-2\ln(\mathcal{L}_{\rm ratio})$ value for each pseudoexperiment. The distribution of these values resembles a χ^2 distribution of 41 degrees of freedom. Thus the value $[-2\ln(\mathcal{L}_{\rm ratio})]_{\rm min} = 29.7$ from the fit to data indicates that the data are consistent with the prediction within the prior uncertainties assigned for the neutrino flux model, neutrino interaction model, and detector response model.

The propagated neutrino flux and cross section parameter values prior to and after the fit are listed in Table XII. The fit decreases the flux prediction near the spectrum peak to improve agreement with the data. In addition to modifying the parameter central values and uncertainties, the fit also sets the correlations between parameters. Prior to the fit, the flux and cross section model parameters have no correlation, but the fit introduces anticorrelations, as shown in Fig. 19. The anticorrelations arise because the event rate depends on the product of the neutrino flux and the neutrino interaction cross section.

D. Consistency checks with ND280 data

We perform a consistency check of the fit results by applying the fitted parameters to the ND280 MC simulation and investigating the data and predicted rates in more finely binned kinematic distributions. Figure 20 shows the level of agreement in the muon momentum and angle distributions of the CCQE and CCnonQE-like samples before and after the fit constraint to the flux and cross section models are applied. The fitted flux and cross section models show improved agreement with the data.

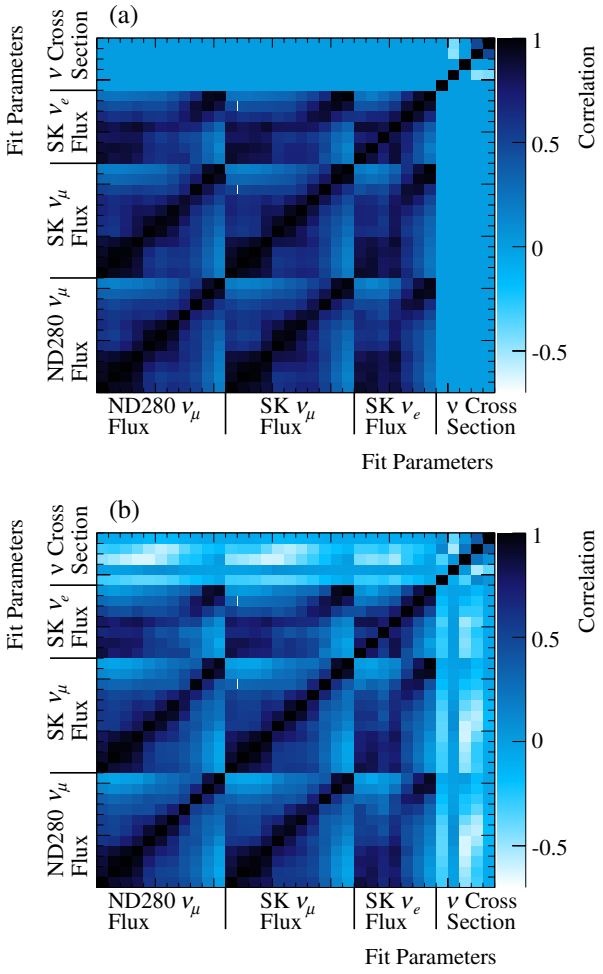

FIG. 19 (color online). The neutrino flux and cross section parameter correlations before (a) and after (b) the fit to the ND280 data. The flux parameters are ordered by increasing energy with the binning listed in Table XII (the correlations of the antineutrino flux parameters are not shown in this figure). The cross section parameter ordering is $M_A^{\rm QE}$, $M_A^{\rm RES}$, CCQE low energy normalization, CC1π low energy normalization and NC1π^0 normalization.

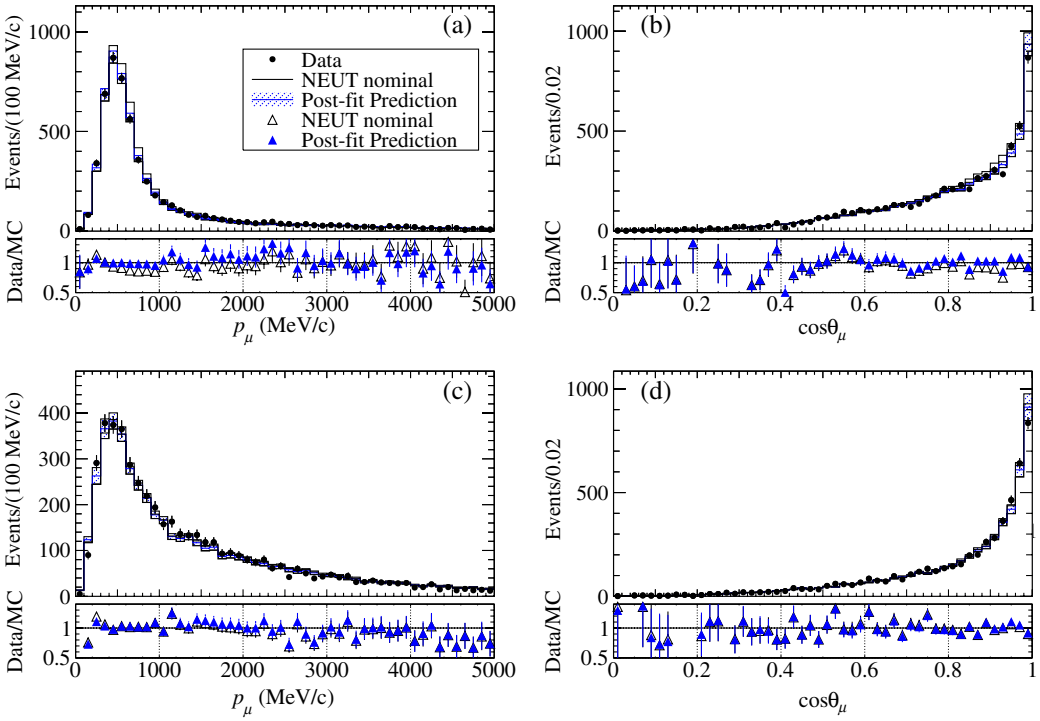

FIG. 20 (color online). Comparisons of the p_μ (left column) and $\cos\theta_\mu$ (right column) distributions for CCQE-like ν_μ selected events in (a) and (b) and CCnonQE-like ν_μ selected events in (c) and (d). The solid line represents the NEUT nominal prediction and the hatched region represents the postfit MC prediction. The dots are the data events. Below each graph, the data/MC ratio is shown for both the NEUT nominal prediction (empty triangle) and postfit MC prediction (full triangle). The error on the points is the statistical error on the data.

We also apply the fitted flux and cross section parameters to the ND280 CC ν_e simulation. Adopting the same analysis as in Sec. VI D while using the fitted cross section and flux parameters, we measure the ratio of inferred to predicted CC ν_e rate to be $0.91 \pm 0.10(\text{stat}) \pm 0.10(\text{syst})$. The CC ν_e rate remains consistent within the reduced systematic uncertainties after tuning.

To check the modeling of NCπ^0 production, we measure the rate of single π^0 with the P0D detector using a data set corresponding to 8.55×10^{19} POT. The ratio of the measured to the predicted rate is found to be $0.84 \pm 0.16(\text{stat}) \pm 0.18(\text{syst})$. When normalized to the corresponding ratio from the ND280 CC ν_μ selection, we measure a ratio of $0.81 \pm 0.15(\text{stat}) \pm 0.14(\text{syst})$, indicating that the predicted rate is consistent with the measured rate within errors.

VIII. SK ELECTRON NEUTRINO SELECTION

For a nonzero value of θ_{13}, we expect an oscillated $\nu_\mu \rightarrow \nu_e$ flux with a peak oscillation probability near 600 MeV at the SK detector. To detect the oscillated ν_e, we select SK events with a single electronlike Cherenkov light ring, providing a sample that is enhanced in CCQE ν_e interactions. Additional cuts are applied to reduce the backgrounds from intrinsic ν_e contamination of the beam and π^0 background. The selection is described here.

A. The SK detector simulation

We simulate the predicted event distributions at the far detector with the neutrino flux prediction up to 30 GeV, the NEUT cross section model, and a GEANT3-based detector simulation. The ν_e signal events from $\nu_\mu \rightarrow \nu_e$ oscillation are produced using the predicted ν_μ spectrum without oscillations, and the ν_e cross section; oscillations probabilities are applied after the simulation. Additionally, the intrinsic ν_μ, $\bar{\nu}_\mu$, ν_e and $\bar{\nu}_e$ components of the beam are generated from the intrinsic flux predictions without oscillations.

SKDETSIM, a GEANT3-based simulation of the SK detector, simulates the propagation of particles produced in the neutrino interactions in the SK detector. We use the GCALOR physics package to simulate hadronic interactions in water since it successfully reproduces pion interaction data around 1 GeV. For pions with momentum below 500 MeV, however, we use custom routines based on the cascade model used by NEUT to simulate interactions of final state hadrons. SKDETSIM models the propagation of light in water, considering absorption, Rayleigh scattering, and Mie scattering as possible interactions. The parameters employed in the models of these processes have been tuned using a number of laser calibration sources [42]. Example event displays for simulated SK events are shown in Fig. 21.

As a final step, we scale the predicted events according to the constrained flux and cross section models from the fit to the ND280 ν_μ CC-inclusive data, and according to the

oscillation probability. The three-neutrino oscillation probability, including matter effects, is calculated for each event with the parameter values shown in Table XIII, unless otherwise noted.

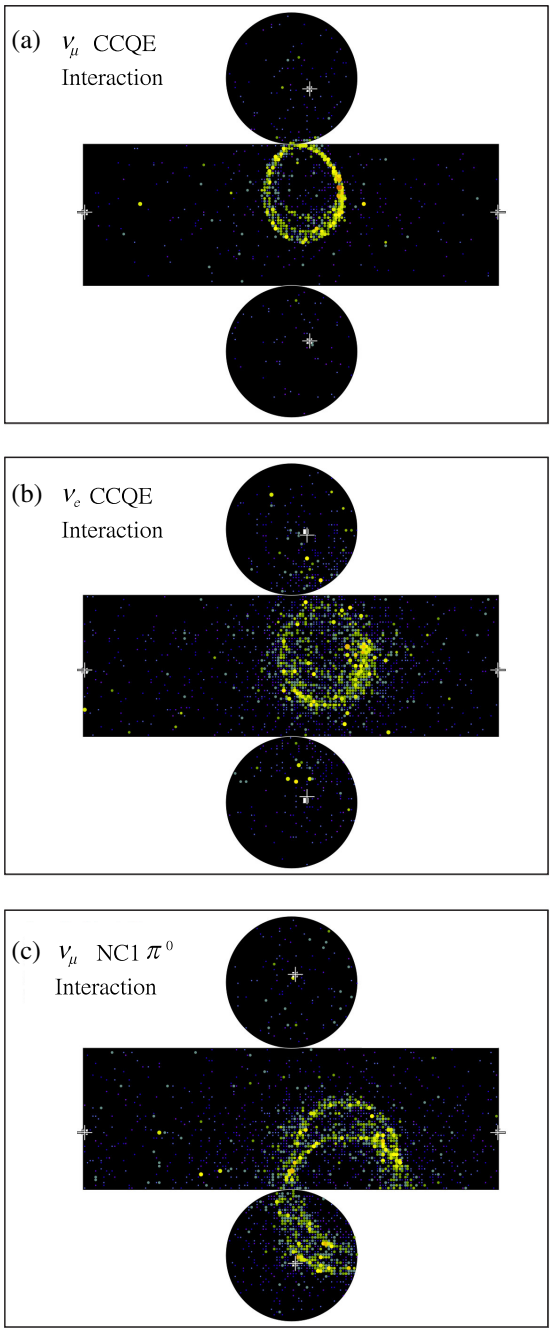

FIG. 21 (color online). Example event displays for the SK simulation of (a) ν_μ CCQE (single well-defined ring from the muon), (b) ν_e CCQE (single diffuse ring from the electron) and (c) ν_μ NC1π^0 interactions (two diffuse rings from the $\pi^0 \rightarrow \gamma\gamma$ decay). The images show the detected light pattern at the ID wall, with the cylindrical SK detector shown as a flat projection. The color indicates the amount of charge detected by the PMT, with purple dots corresponding to the least amount of charge, and red the most.

TABLE XIII. Default neutrino oscillation parameters and Earth matter density used for the MC prediction.

Parameter	Value
Δm^2_{21}	7.6×10^{-5} eV^2
$\lvert\Delta m^2_{32}\rvert$	2.4×10^{-3} eV^2
$\sin^2\theta_{12}$	0.32
$\sin^2 2\theta_{23}$	1.0
δ_{CP}	0
Mass hierarchy	normal
ν travel length	295 km
Earth matter density	2.6 g/cm^3

B. Neutrino event selection

We select fully contained (FC) events, which deposit all of their Cherenkov light inside the SK inner detector (ID), by applying the following selection criteria. First, any photomultiplier tubes (PMTs) which register sufficient charge, a "PMT hit," in the outer detector (OD) are associated with other nearby PMT hits to form clusters. Events with greater than 15 hits in the highest charge OD cluster are rejected. Second, most of the low energy (LE) events are removed by requiring that the total charge from ID PMT hits in a 300 ns time window must be above 200 photoelectrons (p.e.), corresponding to visible energy, $E_{\rm vis}$, above 20 MeV. Visible energy is defined as the energy of an electromagnetic shower that produces the observed amount of Cherenkov light. In order to remove events caused by radioactivity very close to the PMT, a third cut removes events in which a single ID PMT hit has more than half of the total charge in a 300 ns time window.

The final FC selection cut rejects events with ID photomultipliers which produced light because of a discharge around the dynode, called "flasher" events. The cut identifies flasher events from their timing distribution, which is much broader than neutrino events, and from a repeating pattern of light in the detector. However, neutrino events are sometimes misidentified as flasher events when the neutrino interaction vertex is close to the ID wall. There have been a total of eight events that have been rejected by the flasher cut during all run periods. From event time information and visual inspections, it is clear that all eight events are induced by beam neutrino interactions. The predicted number of rejected beam events from this cut is 3.71 events; the probability to observe 8 or more events when 3.71 are expected is 3.6%. All eight events have vertices close to the ID wall, and would be rejected by the fiducial cut.

We define the quantity ΔT_0, which is the timing of the event relative to the leading edge of the spill, accounting for the travel time of the neutrino from production to detection. Figure 22 shows the ΔT_0 distribution of all FC, OD and LE events within ± 500 μs of the beam arrival time; the spill duration is about 5 μs. A clear peak at $\Delta T_0 = 0$ is seen for the FC sample. We observe five FC events outside of the 5 μs spill window. The expected

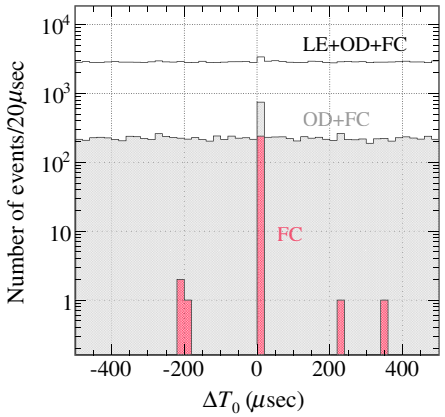

FIG. 22 (color online). ΔT_0 distribution of all FC, OD and LE events observed in the ± 500 μs T2K windows. The OD histogram is stacked on the FC histogram, and the LE histogram is stacked on the OD and FC histograms.

number of such out-of-time FC events, mainly low energy events and atmospheric neutrino events, is estimated to be 3.3 from data collected when the beam is not present. Figure 23 shows the ΔT_0 distribution of FC events within the spill window. We correct the ΔT_0 of each event to account for the position of the neutrino interaction vertex and the photon propagation time from the interaction vertex to the PMTs. The far detector event timing clearly exhibits the eight bunch beam timing structure. The eight dotted vertical lines in the figure represent the eight bunch centers at intervals of 581 ns from a fit to the observed FC event timing. The rms value of the residual time distribution between each FC event and the closest of the fitted bunch center times is about 25 ns.

We require the ΔT_0 for selected FC events to be between -0.2 μs to 10 μs. We observe 240 such in-time fully contained events. We extract a fully contained sample within the fiducial volume (FCFV) by further requiring $E_{\rm vis}$ to be above 30 MeV and the reconstructed vertex be 2 m away from the ID wall. We observe 174 such FCFV events, while the expected accidental contamination from events unrelated to the beam, mostly atmospheric neutrino interactions, is calculated to be 0.005 events.

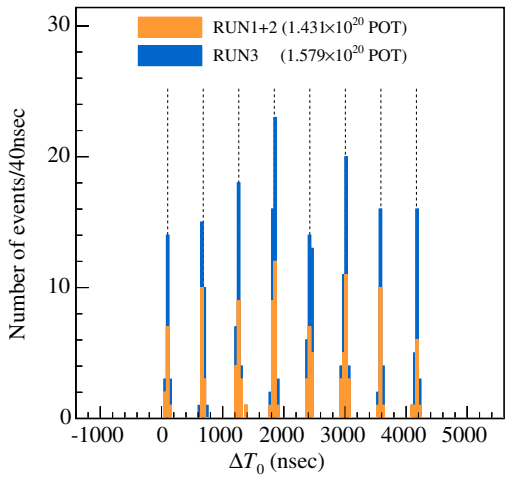

FIG. 23 (color online). ΔT_0 distribution of FC events zoomed in on the spill time observed during T2K Run 1 + 2 and Run 3. The eight dotted vertical lines represent the 581 ns interval bunch center position fitted to the observed FC event times.

CC ν_e interactions ($\nu_e N \rightarrow e^- X$) are identified in SK by detecting a single, electronlike ring; at the energy of the T2K neutrino beam, most of the produced particles other than the electron are below Cherenkov threshold or do not exit the nucleus. The main backgrounds are intrinsic ν_e contamination in the beam and NC interactions with a misidentified π^0. The analysis relies on the well-established reconstruction techniques developed for other data samples in SK [109]. The single, electronlike ring selection criteria are unchanged from our previous measurement of electron neutrino appearance [21], and were determined from MC studies before data-taking commenced. We select CC ν_e candidate events which satisfy the following criteria:

(1) The event is fully contained in the ID and the reconstructed vertex is within the fiducial volume (FCFV).
(2) There is only one reconstructed ring.
(3) The ring is electronlike.
(4) The visible energy, $E_{\rm vis}$, is greater than 100 MeV.
(5) There is no Michel electron
(6) The event's invariant mass is not consistent with a π^0 mass.
(7) The reconstructed neutrino energy, $E_\nu^{\rm rec}$, is less than 1250 MeV.

The $E_{\rm vis}$ cut removes low energy NC interactions and electrons from the decay of unseen muons and pions,

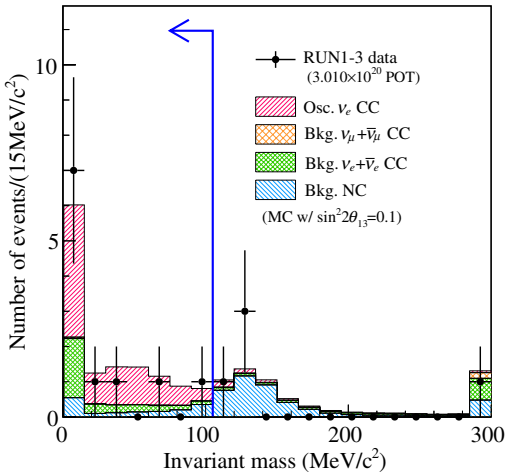

FIG. 24 (color online). Distribution of invariant mass $M_{\rm inv}$ when each event is forced to be reconstructed as two photon rings. The data are shown as points with error bars (statistical only) and the MC predictions are in shaded histograms. The last bin shows overflow entries. The arrow shows the selection criterion $M_{\rm inv} < 105$ MeV/c^2.

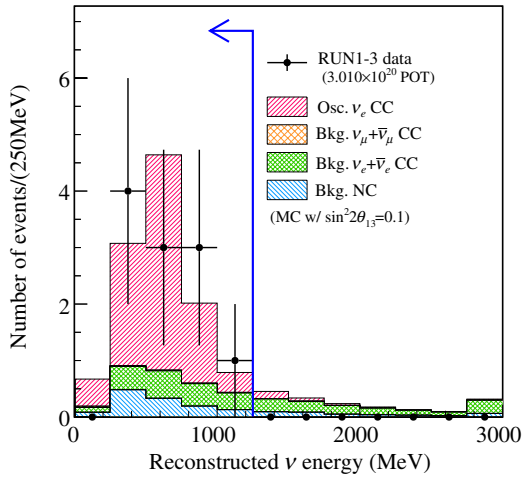

FIG. 25 (color online). Distribution of the reconstructed neutrino energy spectrum of the events which pass all ν_e appearance signal selection criteria with the exception of the energy cut. The data are shown as points with error bars (statistical only) and the MC predictions are in shaded histograms. The arrow shows the selection criterion $E_\nu^{\rm rec} < 1250$ MeV.

such as cosmic muons outside the beam time window or muons below Cherenkov threshold. A Michel electron is an electron from muon decay which is identified by looking for a time-delayed ID-PMT hit peak after the primary neutrino interaction. In order to reduce NC π^0 events, we utilize a special fitter which reconstructs each event with a two photon ring hypothesis. It searches for the direction and energy of the second ring which maximizes the likelihood based on the light pattern of the event [110]. Figure 24 shows the invariant mass $M_{\rm inv}$ distribution of the two photon rings for the data and simulation. As shown in the figure, the NC background component peaks around the π^0 invariant mass, hence events with $M_{\rm inv} > 105$ MeV$/c^2$ are cut. Finally, the energy of the parent neutrino is computed assuming CCQE kinematics and neglecting Fermi motion as follows:

$$E_\nu^{\rm rec} = \frac{m_p^2 - (m_n - E_b)^2 - m_e^2 + 2(m_n - E_b)E_e}{2(m_n - E_b - E_e + p_e \cos\theta_e)}, \quad (18)$$

where m_p is the proton mass, m_n the neutron mass, and $E_b = 27$ MeV is the binding energy of a nucleon inside a ^{16}O nucleus. E_e, p_e, and θ_e are the reconstructed electron energy, momentum, and angle with respect to the beam direction, respectively. We select $E_\nu^{\rm rec} < 1250$ MeV since the signal at high energy is expected to be small for the atmospheric mass splitting, and the intrinsic ν_e background is dominant in this region, as shown in Fig. 25.

The numbers of observed events after each selection criterion, and the MC predictions for $\sin^2 2\theta_{13} = 0.1$ and $\sin^2 2\theta_{13} = 0$, are shown in Tables XIV and XV, respectively. Eleven events remain in the data after all ν_e appearance signal selection criteria are applied. Using the MC simulation, we estimate the ν_e appearance signal efficiency in the SK FV to be 62%, while the rejection rates for CC $\nu_\mu + \bar{\nu}_\mu$, intrinsic CC $\nu_e + \bar{\nu}_e$, and NC are >99.9%, 80%, and 99%, respectively. More than half of the remaining background is due to intrinsic CC ν_e interactions (57% for $\sin^2 2\theta_{13} = 0.1$). The fraction of CCQE events in the CC ν_e signal and background are 80% and 65%, respectively. NC interactions constitute 41% of the total surviving background, 80% of which are due to π^0 mesons and 6% of which originate from NC single photon ($\Delta \to N\gamma$) production.

Additional checks of the 11 data events are performed. From visual inspection, it appears that all events have only a single, electronlike Cherenkov ring. A KS test of the observed number of ν_e candidate events as a function of accumulated POT is compatible with the normalized event rate being constant (p value = 0.48) as shown in Fig. 26. Figure 27 shows the (x, y) and (r^2, z) distributions of the reconstructed vertices of observed ν_e candidate events. As we previously reported, the first 6 candidate events were clustered near the edge of the FV in the upstream beam direction. We observe no such clustering in the newly observed 5 events (pink points in the figure). All event

TABLE XIV. Event reduction for the ν_e appearance search at the far detector. After each selection criterion is applied, the numbers of observed and MC expected events of CC ν_μ, intrinsic CC ν_e, NC, and the CC ν_e signal, are given. All MC samples include three-neutrino oscillations for $\sin^2 2\theta_{13} = 0.1$, $\delta_{CP} = 0$, and normal mass hierarchy.

	Data	MC total	CC ν_μ	CC ν_e	NC	CC $\nu_\mu \to \nu_e$
(0) Interaction in FV	n/a	311.4	158.3	8.3	131.6	13.2
(1) Fully contained in FV	174	180.5	119.6	8.0	40.2	12.7
(2) Single ring	88	95.7	68.4	5.1	11.4	10.8
(3) e-like	22	26.4	2.7	5.0	8.0	10.7
(4) $E_{\rm vis} > 100$ MeV	21	24.1	1.8	5.0	6.9	10.4
(5) No delayed electron	16	19.3	0.3	4.0	5.9	9.1
(6) Not π^0-like	11	13.0	0.09	2.8	1.6	8.5
(7) $E_\nu^{\rm rec} < 1250$ MeV	11	11.2	0.06	1.7	1.2	8.2

TABLE XV. Same as Table XIV but with MC prediction for $\sin^2 2\theta_{13} = 0$.

	Data	MC total	CC ν_μ	CC ν_e	NC	CC $\nu_\mu \to \nu_e$
(0) Interaction in FV	n/a	299.0	158.5	8.6	131.6	0.3
(1) Fully contained in FV	174	168.5	119.8	8.2	40.2	0.3
(2) Single ring	88	85.4	68.5	5.3	11.4	0.2
(3) e-like	22	16.1	2.7	5.2	8.0	0.2
(4) $E_{\rm vis} > 100$ MeV	21	14.1	1.8	5.2	6.9	0.2
(5) No delayed electron	16	10.6	0.3	4.2	5.9	0.2
(6) Not π^0-like	11	4.8	0.09	2.9	1.6	0.2
(7) $E_\nu^{\rm rec} < 1250$ MeV	11	3.3	0.06	1.8	1.2	0.2

vertices are $x < 0$ in the SK coordinate system which is not related to the beam direction. Other T2K neutrino selections with larger event samples, such as the CC ν_μ selection, populate the entire x and y region. Figure 28 shows the distribution of distance from the ID wall to the vertex along the beam direction for events passing all ν_e selection cuts except the FV cut. A KS test to this distribution yields a p value of 0.06. In addition, a dedicated selection of penetrating particles produced in upstream, out-of-FV neutrino interactions shows no indication of an excess.

C. SK efficiency and reconstruction uncertainties

We have studied the systematic uncertainties on the simulation of the SK event selection efficiency and reconstruction using comparisons of data and MC control samples. The error on the FC event selection is estimated to be 1%, with a dominant contribution from the flasher event rejection. We evaluate the flasher rejection uncertainty from the difference in the cut efficiency between the atmospheric neutrino data and MC simulation. We estimate the uncertainty on the fiducial volume definition to be 1% by comparing the reconstructed vertex distributions of observed and simulated cosmic-ray muons which have been independently determined to have stopped inside the ID. We estimate an energy scale uncertainty of 2.3% from comparisons of distributions between cosmic-ray data and simulated samples. These samples include the reconstructed momentum spectrum of electrons from the decay of cosmic ray muons, cosmic-ray muons which stop in SK and have similar energies to the T2K neutrino events, and the reconstructed mass of neutral pions from atmospheric neutrino interactions. The error on the number of ν_e candidate events due to the uncertainty on the delayed, decay-electron tagging efficiency is 0.2%. We evaluate this uncertainty from a comparison of the tagging efficiency between cosmic-ray stopped muon data and MC samples.

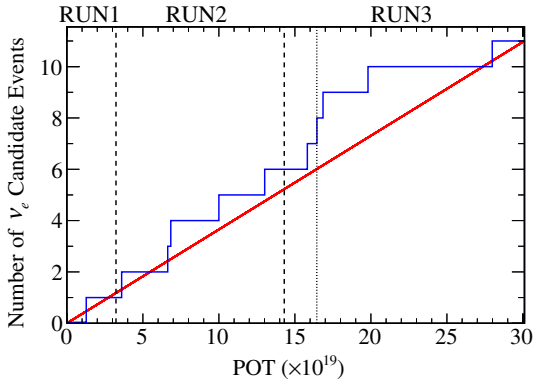

FIG. 26 (color online). The cumulative number of observed ν_e candidate events as a function of accumulated POT. The vertical dashed lines separate the three running periods, and the dotted line indicates the horn current change during Run 3. The solid line indicates a hypothesis of constant event rate.

The remaining uncertainties on the detection efficiency are evaluated in categories corresponding to the particles exiting the target nucleus. The "CC ν_e single electron" category is comprised of interactions where a single electron is emitted and is the only detectable particle in the final state. The "CC ν_e other" category includes all other CC ν_e interactions not in the CC ν_e single electron category. NC events are also classified based on the particle type which exits the nucleus. The "NC single π^0" category includes events with only one π^0 in the detector.

The topological light pattern of the rings provides the information needed to construct quantities used in the selection: the number of rings (cut 2), particle identification (cut 3) and the invariant mass (cut 6). We evaluate the systematic error on the efficiency of each of the three topological cuts on the selection with a fit to SK atmospheric neutrino data using MC simulation-based templates. We create two control samples in the SK atmospheric neutrino data set which are sensitive to CC ν_e single electron and CC ν_e other event types. The ν_e enriched control samples pass the FCFV, $E_{\rm vis} > 100$ MeV criteria; however, the number of decay electrons in the event is used to separate QE-like (single ring) from nonQE-like (multiple rings) instead of the ring-counting algorithm. Each control sample is divided into one "core" subsample, which passes the three topological cuts, and three "tail" subsamples, where events have failed one of the three topological cuts. The subsamples are further divided into 17 bins (labeled with index i) in p_e and θ_e, the reconstructed electron momentum and angle with respect to the beam direction, so that we can evaluate the dependence of the systematic

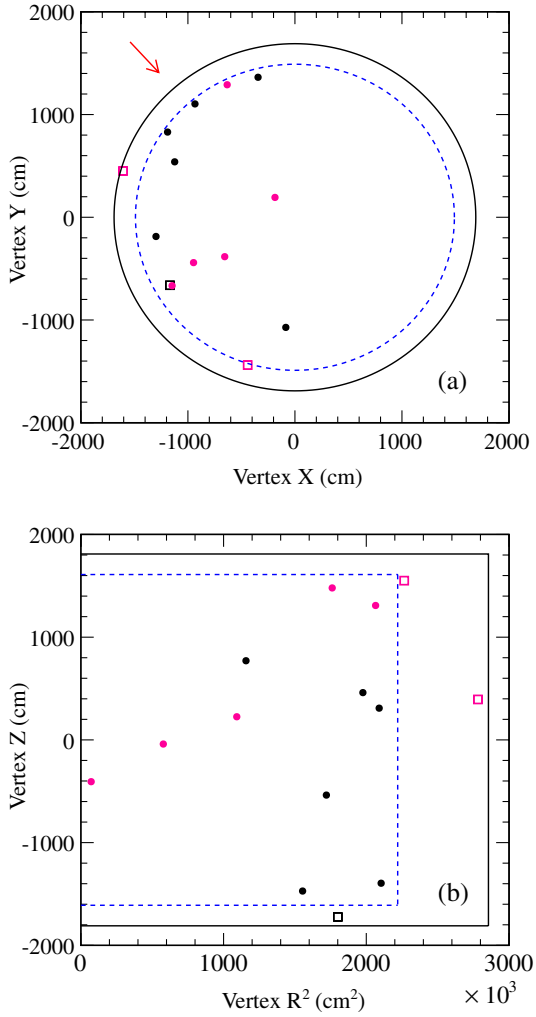

FIG. 27 (color online). (a) Two-dimensional (x, y) distribution of the reconstructed vertex positions of observed ν_e candidate events. (b) Two-dimensional $(r^2 = x^2 + y^2, z)$ distribution of the reconstructed vertex positions of the observed ν_e candidate events. The arrow indicates the neutrino beam direction and the dashed line indicates the fiducial volume boundary. Black markers are events observed during Run 1 + 2, and pink markers are events from Run 3. Open squares represent events which passed all the ν_e selection cuts except for the fiducial volume cut.

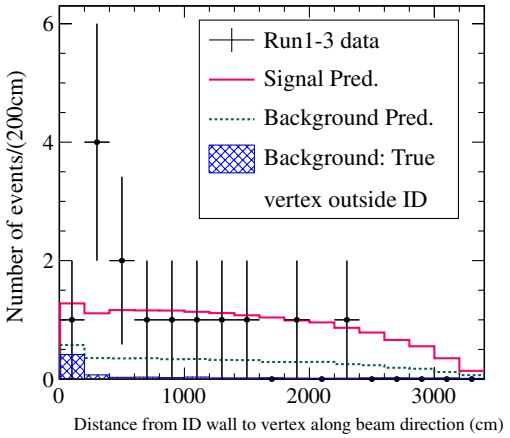

FIG. 28 (color online). Distribution of events which pass ν_e selection cuts except for the FV cut as a function of the distance from the ID wall to the vertex, calculated along the beam direction. The solid line indicates the expected distribution for signal ($\sin^2 2\theta_{13} = 0.1$) and background, and the background prediction is shown with the dashed line. The hatch-filled histogram shows the subset of background whose true vertex is outside the ID.

errors on these kinematic variables. The expected number of events in all subsamples depends on the efficiency of each topological cut, $\vec{\epsilon} = \{\epsilon_{\text{1ring}}, \epsilon_{\text{PID}}, \epsilon_{\text{inv mass}}\}$, and parameters which represent systematic uncertainties on the event rate, $\vec{\alpha}$. The $\vec{\alpha}$ parameters include uncertainties on the atmospheric neutrino flux normalization, the absolute cross section of CC non-QE and NC interactions, the ν_e/ν_μ relative cross section, and the energy dependence of the CCQE cross section. We perform a χ^2 fit to the atmospheric control samples, allowing the $\vec{\epsilon}$ and $\vec{\alpha}$ parameters to vary.

We extract the uncertainties on the CC ν_e single electron and CC ν_e other event categories based on the effect of the selection cuts on the efficiency $\vec{\epsilon}$ within the fit to the control samples. We estimate the bias as the difference between the fitted value and the nominal value of the event rate for two categories (CC ν_e single electron and CC ν_e other) over 17 reconstructed (p_e, θ_e) bins. The correlations between bins are considered. We also include uncertainties on the event categories determined from the fit; the fit uncertainties are treated as uncorrelated between bins. For the CC ν_e single electron category, the bias is estimated to be 1%–9% across all bins, while the fit uncertainty is 4%–8% across all bins. The bias and fit uncertainty for the CC ν_e other category are 27% and 14%, respectively; this component is a small contribution to the signal and background prediction, and so the momentum and angular dependence of the uncertainty is ignored. As described later, we use these errors and their correlations as inputs for deriving the total SK systematic error on the T2K ν_e appearance candidate events.

NC interactions producing a single exclusive photon via radiative decays of Δ resonances (NC1γ) are a background to the ν_e appearance signal, as the photon ring is very similar to an electron ring. We evaluated the difference in the selection efficiency between the single photon MC sample and the single electron MC sample to estimate the uncertainty on the selection efficiency of NC1γ events. The difference in relative efficiencies is no larger than 1%, so we assign an additional 1% uncertainty, added in quadrature to the uncertainty on single electron rings estimated from the CC ν_e single electron sample efficiency, as the uncertainty on the selection efficiency for NC1γ background events.

We evaluate the systematic uncertainty for events where the muon decays in flight with a MC study. The Cherenkov ring of the electron from a muon which decays in flight

tends to be in the same direction as the parent muon, and therefore these events look similar to CC ν_e interactions. We estimate the uncertainty on the expected number of muon-decay-in-flight background events to be 16%, with the largest contribution from the uncertainty on the muon polarization. The fraction of muons which decay in flight in the selected ν_e candidate event sample is estimated to be smaller than 1%, and so this uncertainty does not contribute substantially to the total uncertainty on the ν_e candidates.

The efficiency of NC1π^0 events for the ν_e selection criteria is determined to be 6% from the MC simulation. To evaluate the systematic uncertainty for events with a π^0 in the final state, we construct "hybrid-π^0" control samples. The hybrid-π^0 samples contain events where a π^0 is constructed using one simulated photon ring and a second electronlike ring from the SK atmospheric or cosmic-ray samples. The simulated photon ring kinematics are chosen such that the two rings follow the decay kinematics of a π^0. The hybrid samples are constructed with electron rings from data (hybrid-π^0 data) and the simulation (hybrid-π^0 MC), and the comparison of the two is used to evaluate the systematic uncertainties.

We investigate the systematic error coming from the higher-energy ring and the lower-energy ring separately. The "primary" sample uses electron rings from the SK atmospheric samples, with the electron ring having higher energy than the simulated photon ring. In the "secondary" sample the electron ring has a lower energy than the photon ring. Below 60 MeV, electrons from cosmic-ray muons are used; otherwise the electrons from the SK atmospheric samples are used.

We compare the efficiency of the ν_e selection criteria on π^0 events in the hybrid-π^0 data and hybrid-π^0 MC samples in each of the 17 (p_e, θ_e) bins. We apply the efficiency differences as correlated systematic errors among bins, while the statistical errors on the efficiency differences are applied as uncorrelated systematic errors. For the NC single π^0 component, we estimate correlated errors in each (p_e, θ_e) bin to be between 2%–60%, and uncorrelated errors are between 15%–50%. The assigned errors are larger in the lower momentum bins, where the π^0 selection efficiency is lower. We evaluate the systematic uncertainties on events with one or more charged particles above Cherenkov threshold and a π^0 by using hybrid-π^0 control samples with additional simulated rings for the extra particles.

Finally, we combine all systematic uncertainties on the ν_e appearance signal selection at SK into a single covariance matrix. The covariance matrix has bins in the observable kinematic variables, (p_e, θ_e) or E_ν^{rec}, for the four event categories: signal CC ν_e, background CC ν_μ, CC ν_e, and NC. We use this covariance matrix to model the systematic uncertainties on the simulated detector efficiency and reconstruction in the oscillation fits described in Sec. IX. The fractional errors as a function of the both the electron momentum and angle are shown in Fig. 29.

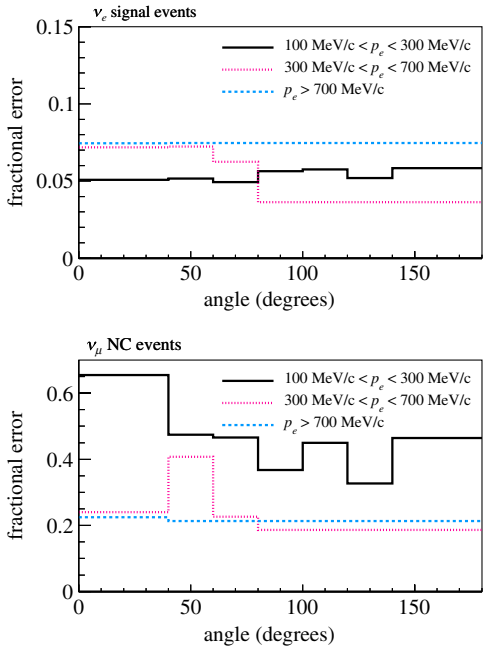

FIG. 29 (color online). The fractional errors on SK ν_e signal (top) and NC background (bottom) predictions from the SK detector response uncertainty as a function of the electron candidate momentum and angle.

IX. OSCILLATION FIT METHOD AND RESULTS

The ν_e appearance oscillation signal is an excess of ν_e candidates over background. Tables XIV and XV show the predicted number of ν_e candidate events after we apply the tuned neutrino flux and cross section parameters discussed in Sec. VII. If $\sin^2 2\theta_{13} = 0.1$, we expect 11.2 events, and if $\sin^2 2\theta_{13} = 0$, we expect 3.3. We evaluate the systematic uncertainties on the expected signal and background event rates due to the uncertainties on the flux model, neutrino interaction cross section model and SK reconstruction efficiencies, as summarized in Sec. IX A.

The probability to observe 11 or more events based on the predicted background of 3.3 ± 0.4(syst) events is 9×10^{-4}, equivalent to an exclusion significance of 3.1σ. This rate-only hypothesis test makes no assumptions about the energy spectrum of the candidate events or their consistency with the neutrino oscillation hypothesis; it is a statement that we observe an excess of electronlike events over background. The background model includes expected $\nu_\mu \rightarrow \nu_e$ oscillation through the solar term shown in Eq. (2), which corresponds to 0.2 events. The reported p value corresponds to the probability to observe 11 or more events from background sources and oscillations that depend on the θ_{12} mixing angle. If instead we consider the probability to observe 11 or more events from background sources only, the p value is 6×10^{-4}.

We fit the ν_e candidate sample in the three-neutrino mixing paradigm to estimate $\sin^2 2\theta_{13}$. The dominant effect of a nonzero $\sin^2 2\theta_{13}$ is to increase the overall rate of

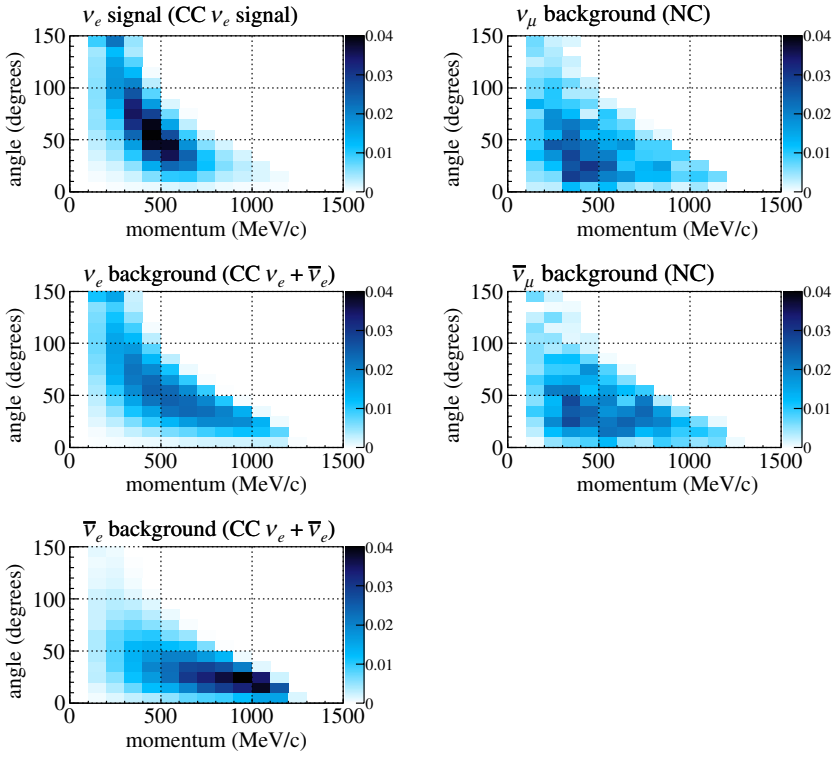

FIG. 30 (color online). (p_e, θ_e) distribution for ν_e signal (top left), ν_μ background (top right), ν_e background (middle left), $\bar{\nu}_\mu$ background (middle right) and $\bar{\nu}_e$ background (bottom left). Each distribution is normalized to unit area.

ν_e events. However, spectral information, e.g. electron momentum and angle with respect to the T2K beam direction, (p_e, θ_e), or reconstructed neutrino energy, $E_\nu^{\rm rec}$, can be used to further separate the signal from background. Figure 30 shows the area-normalized (p_e, θ_e) distribution for the ν_e candidate events predicted by the SK simulation. The signal CC ν_e are predominantly CCQE, and peaked at $E_\nu \approx 0.6$ GeV, near the first oscillation maximum and neutrino flux peak. This results in a clear kinematic correlation across the (p_e, θ_e) distribution for signal events. This peak is also visible in the $E_\nu^{\rm rec}$ distribution for signal events, shown in Fig. 31. Conversely, the backgrounds to the ν_e signal populate a wider range of kinematic space. The NC backgrounds are predominantly photons misidentified as electron neutrino candidates, when one photon from π^0 decay is not reconstructed, or when the two photons are colinear. This background predominantly populates the low momentum and forward angle region as well as the signal region. The intrinsic beam ν_e ($\bar{\nu}_e$) backgrounds have a larger contribution of events at higher energy than the oscillated ν_e, and so more often produce electrons with high momentum in the forward direction.

We find that based on studies of the $E_\nu^{\rm rec}$ and (p_e, θ_e) kinematic distributions that the (p_e, θ_e) distribution has the best power to discriminate signal and background with the minimal cross section model dependence, hence we perform a two-dimensional extended maximum likelihood fit to the (p_e, θ_e) data distribution. Section IX B describes the (p_e, θ_e) likelihood fit to estimate $\sin^2 2\theta_{13}$, and Sec. IX D describes two additional fits using $E_\nu^{\rm rec}$ and rate-only information for comparison to the (p_e, θ_e) fit.

A. ν_e predicted event rate and systematic uncertainties

The predicted number of ν_e candidates and the event shape distribution depend upon the flux, cross section parameters, oscillation probability, and the efficiency and resolution of the SK detector. We calculate the predicted number of events in a given momentum and angular bin (i) as

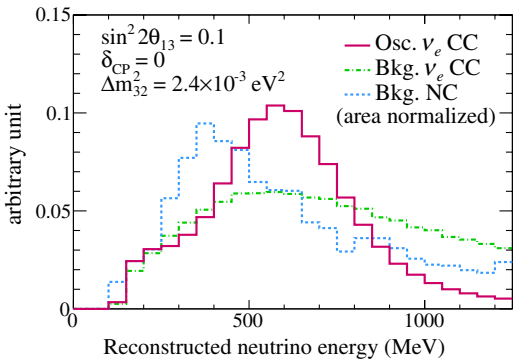

FIG. 31 (color online). The MC reconstructed neutrino energy distributions of $\nu_\mu \rightarrow \nu_e$ CC signal, intrinsic ν_e CC background and NC background components in the ν_e candidate event sample. The histograms are normalized to the same area.

$$N_i^p(\vec{o},\vec{f}) = \sum_j^{\text{flux type}} \left[\sum_{k=1}^{E_\nu \text{bins}} b_{j,k} \cdot \left\{ \sum_{l=1}^{\text{Int modes}} P^{\text{osc}}_{j,k,l}(\vec{o}) x^{\text{norm}}_{k,l} w_{i,j,k,l}(\vec{x}) \cdot d_{i,j,k} \cdot T^p_{i,j,k,l} \right\} \right]. \quad (19)$$

Here, $T^p_{i,j,k,l}$ are the nominal Monte Carlo templates that predict the event rate as a function of

(i) momentum/angular bins (i). The momentum bins are 100 MeV/c wide from 0 MeV/c to 1500 MeV/c (15 in total), and the angular bins are 10° wide from 0° to 140° with one bin for $\theta_e > 140°$ (15 in total). The bins are ordered by increasing θ_e in groups of increasing momentum.

(ii) flux type (j) with categories for ν_e signal, ν_μ background, ν_e background, $\bar{\nu}_\mu$ background and $\bar{\nu}_e$ background.

(iii) true neutrino energy (k) with 200 bins (50 MeV wide) from 0 GeV to 10 GeV and one bin from 10 GeV to 30 GeV.

(iv) interaction mode (l) with categories for CCQE, CC1π, CC coherent, CC other, NC1π^0, NC coherent and NC other.

The systematic parameters are $\vec{f} = (b_{j,k}, x^{\text{norm}}_{k,l}, \vec{x}, d_{i,j,k}, f^s)$. The $b_{j,k}$ vary the flux normalization, and the $x^{\text{norm}}_{k,l}$ are cross section normalization parameters. The $\vec{x}$ are cross section parameters such as M_A^{QE} and p_F where the effect on the prediction is modeled with response functions, $w_{i,j,k,l}$, evaluated for each combination of observable bin, flux type, neutrino energy bin and interaction mode. The $d_{i,j,k}$ are systematic parameters that vary the normalization of the prediction for each combination of observable bin, flux type and interaction mode. These parameters are used to model variations due to final state interactions and SK efficiency uncertainties. The momentum scale variation according to the parameter f^s is not shown in Eq. (19). The parameter f^s scales the momentum range of the bins and the bin contents are recalculated assuming a flat momentum dependence in each bin.

We compute three-neutrino oscillation probabilities, $P^{\text{osc}}_{k,l,m}(\vec{o})$, which include matter effects, according to the numerical technique defined in Ref, [111], for a given set of the oscillation parameters, $\vec{o}$. The δ_{CP} dependence is evaluated by scanning the value of δ_{CP} and fitting for $\sin^2 2\theta_{13}$ with δ_{CP} fixed at each scan point. The remaining oscillation parameters are always held fixed to the values listed in Table XIII.

Based on Eq. (19), we predict both the total number of events and the normalized (p_e, θ_e) shape distribution [probability density function (PDF)]. The predicted number of events and the predicted (p_e, θ_e) distribution are used in the likelihood function of the oscillation fit. The effect of the systematic uncertainties on the predicted number of events and (p_e, θ_e) PDF are studied by recalculating the rate and PDF under variations of the systematic parameters according to the prior probability distribution of the parameters. Table XVI summarizes the uncertainty on the predicted number of events for each systematic error source assuming $\sin^2 2\theta_{13} = 0$ and $\sin^2 2\theta_{13} = 0.1$.

Uncertainties related to the nuclear model are applied independently for the SK prediction and are not constrained by the fit to ND280 data since the primary target nuclei are different in the ND280 (^{12}C) and SK (^{16}O) detectors. These uncertainties include the nuclear model uncertainty (x_{SF}), the uncertainty on the Fermi momentum in the relativistic Fermi gas model (p_F), the uncertainty on the $N\pi$ invariant mass for resonant production in the nuclear medium (W_{eff}), the uncertainty on the rate of non-pionic decays of Δ resonances in the nuclear medium ($x_{\pi\text{-less}}$), and uncertainties on the final state interactions of pions in the nucleus. The nuclear model related uncertainties contribute errors on the event rate prediction of 4.8% for $\sin^2 2\theta_{13} = 0$ and 7.0% for $\sin^2 2\theta_{13} = 0.1$.

The uncertainty on background only predicted number of events ($\sin^2 2\theta_{13} = 0$) is larger than that of signal + background due to the larger uncertainties on the NC backgrounds (32%); the uncertainty on CC background events (14%) is comparable to that of the CC signal events. The inclusion of the ND280 measurements reduces the uncertainty on the total predicted event rate due to the flux and CCQE, CC1π^+ cross section model from 18.3% to 8.5% (22.6% to 5.0%), assuming $\sin^2 2\theta_{13} = 0$ ($\sin^2 2\theta_{13} = 0.1$). The far detector efficiency uncertainty

TABLE XVI. Summary of the contributions to the total uncertainty on the predicted number of events, assuming $\sin^2 2\theta_{13} = 0$ and $\sin^2 2\theta_{13} = 0.1$, separated by sources of systematic uncertainty. Each error is given in units of percent.

	$\sin^2 2\theta_{13} =$	
Error source	0	0.1
Beam flux & ν int. (ND280 meas.)	8.5	5.0
ν int. (from other exp.)		
$x_{\text{CC other}}$	0.2	0.1
x_{SF}	3.3	5.7
p_F	0.3	0.0
$x^{\text{CC coh}}$	0.2	0.2
$x^{\text{NC coh}}$	2.0	0.6
$x^{\text{NC other}}$	2.6	0.8
x_{ν_e/ν_μ}	1.8	2.6
W_{eff}	1.9	0.8
$x_{\pi\text{-less}}$	0.5	3.2
$x_{1\pi E_\nu}$	2.4	2.0
Final state interactions	2.9	2.3
Far detector	6.8	3.0
Total	13.0	9.9

has been reduced from 14.7% (9.4%) in the previous analysis [21] to 6.8% (3.0%) assuming $\sin^2 2\theta_{13} = 0.0$ ($\sin^2 2\theta_{13} = 0.1$) due to new CC ν_e and π^0 SK atmospheric control samples; the FSI uncertainty has also been reduced from 10.1% (5.4%) in the previous results to 2.9% (2.3%) in this analysis, as correlations between reconstructed bins are now taken into account (Sec. V C 1).

We also consider the effect on the (p_e, θ_e) PDF, or "shape" of (p_e, θ_e), as the systematic parameters are changed. Figure 32 (Fig. 33) shows the variation of the one-dimensional angular slices of the total signal + background as a function of momentum for $\sin^2 2\theta_{13} = 0.1$ ($\sin^2 2\theta_{13} = 0$). The main contributions to the shape systematic uncertainties for $\sin^2 2\theta_{13} = 0$ are the SK detector efficiency and W_{eff} parameters in the neutrino interaction models which introduce uncertainties on the (p_e, θ_e) distribution of ν_μ (NC) background. For $\sin^2 2\theta_{13} = 0.1$, the dominant contributions to the shape systematic uncertainties are the ν_μ flux, CCQE and CC1π cross section parameters, x_{SF}, and the SK detector uncertainties.

B. ν_e likelihood

We define an extended likelihood as the product of the likelihoods for the observed number of ν_e candidate events ($\mathcal{L}_{\text{norm}}$), the shape of (p_e, θ_e) distribution of those events ($\mathcal{L}_{\text{shape}}$) and the constraint term for the nuisance parameters ($\mathcal{L}_{\text{syst}}$). The normalization term, $\mathcal{L}_{\text{norm}}$, is defined by the Poisson probability to observe the number of ν_e candidate events, N_{obs}, given a predicted number of events, $n = \sum_{i,j}^{N_{p\theta}} N_{i,j}^{p}(\vec{o}, \vec{f})$:

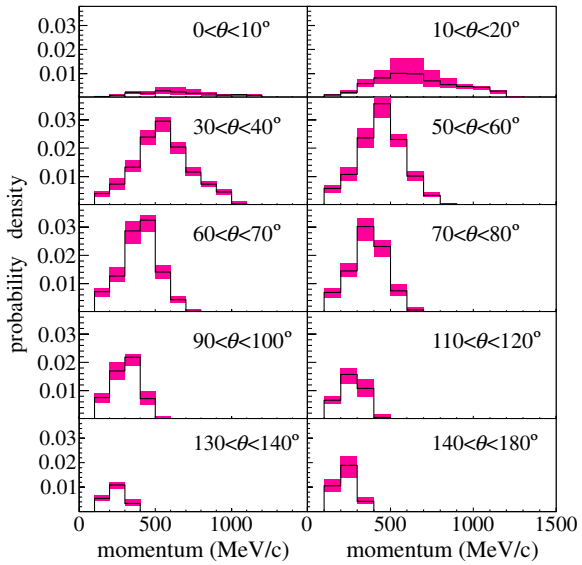

FIG. 32 (color online). The PDF as a function of momentum for different angular bins [10 of 15 (p_e, θ_e) bins are shown] and $\sin^2 2\theta_{13} = 0.1$. The shaded areas represent one sigma deviations that are evaluated by fluctuating all of the systematic parameters according to a multivariate normal distribution using their prior values and covariance matrix.

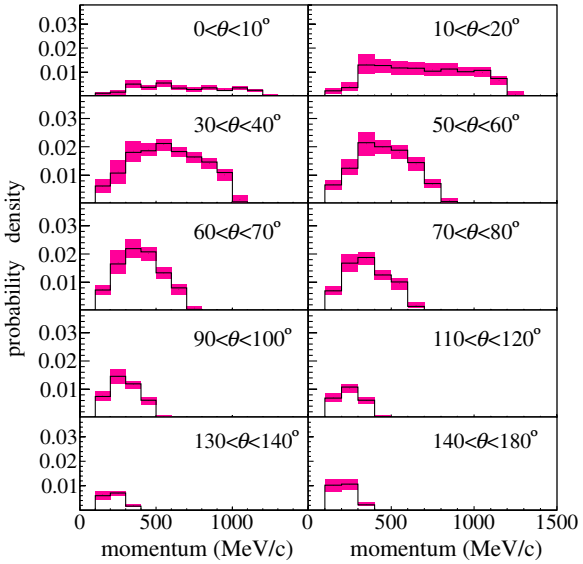

FIG. 33 (color online). The PDF as a function of momentum for the same bins as in Fig. 32 and $\sin^2 2\theta_{13} = 0$. The shaded areas represent one sigma deviations that are evaluated by fluctuating all of the systematic parameters according to a multivariate normal distribution using their prior values and covariance matrix.

$$\mathcal{L}_{\text{norm}}(\vec{o}, \vec{f}) = \frac{(n^{N_{\text{obs}}})e^{-n}}{N_{\text{obs}}!}. \tag{20}$$

The shape term, $\mathcal{L}_{\text{shape}}$ is defined by the product of the probabilities that each event has a particular value of the momentum and angle (p_e, θ_e). We use a Bayesian marginalization technique in order to incorporate the systematic uncertainties, by integrating over all systematic parameters. Then, the only free parameter in the marginalized likelihood is $\sin^2 2\theta_{13}$:

$$\mathcal{L}'(\vec{o}) = \int \mathcal{L}_{\text{norm}}(\vec{o}, \vec{f}) \times \mathcal{L}_{\text{shape}}(\vec{o}, \vec{f}) \times \mathcal{L}_{\text{syst}}(\vec{f}) d\vec{f}. \tag{21}$$

Here we assume $\mathcal{L}_{\text{syst}}$ is a multivariate normal distribution of the systematic parameters defined by the parameters' prior values and covariance matrix. The oscillation parameters are obtained by maximizing the marginalized likelihood.

We have studied the increase in sensitivity of the analysis from the use of kinematic (p_e, θ_e) information and from the ND280 fit. The difference of the log likelihood at the best fit and at another value of $\sin^2 2\theta_{13}$ is calculated as

$$-2\Delta \ln \mathcal{L} = -2[\ln \mathcal{L}'(\sin^2 2\theta_{13}) - \ln \mathcal{L}'(\sin^2 2\theta_{13}^{\text{best}})]. \tag{22}$$

The likelihood in $-2\Delta \ln \mathcal{L}$ can include just the normalization term, or the normalization and shape term, and the systematic term in the likelihood can include the ND280 measurements or not. Figure 34 shows the average $-2\Delta \ln \mathcal{L}$ curves for these three cases, for toy MC data

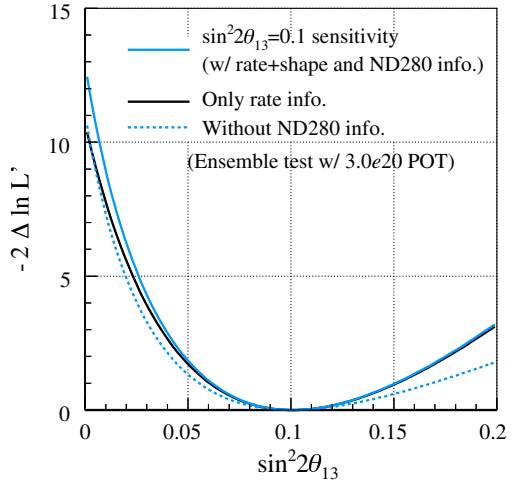

FIG. 34 (color online). The $-2\Delta \ln \mathcal{L}$ average sensitivity curve for toy MC data generated at $\sin^2 2\theta_{13} = 0.1$ with $\delta_{CP} = 0$, normal hierarchy and 3.01×10^{20} POT. The likelihood is shown for three cases: where rate, shape and ND280 information is used, where only rate and ND280 information is used, and where rate and shape information is used without ND280 information.

generated at $\sin^2 2\theta_{13} = 0.1$. We obtained a 20% improvement to $-2\Delta \ln \mathcal{L}$ at $\sin^2 2\theta_{13} = 0$ when kinematic information is included; this is equivalent to a 20% increased beam exposure. Similar studies show a comparable increase of 19% for the use of ND280 information in the likelihood to reduce the systematic errors.

C. Results for $\sin^2 2\theta_{13}$

We performed the fit to the observed 11 ν_e candidate events by allowing $\sin^2 2\theta_{13}$ to vary and scanning the value of δ_{CP}. Figure 35 compares the (p_e, θ_e) kinematic distributions observed in data with the prediction at the best-fit value of $\sin^2 2\theta_{13}$.

Because of the potential bias in the determination of $\sin^2 2\theta_{13}$ near the physical boundary of $\sin^2 2\theta_{13} = 0$, we calculate the confidence intervals following the Feldman-Cousins method [112]. The 68% and 90% confidence intervals calculated using the Feldman-Cousins method and constant $-2\Delta \ln \mathcal{L}$ method are found to be equivalent. Assuming $\delta_{CP} = 0$, the best-fit values of $\sin^2 2\theta_{13}$ with the 68% confidence intervals are

$$\sin^2 2\theta_{13} = 0.088^{+0.049}_{-0.039} \quad \text{(normal hierarchy)},$$
$$\sin^2 2\theta_{13} = 0.108^{+0.059}_{-0.046} \quad \text{(inverted hierarchy)}.$$

The 90% confidence intervals are

$$0.030 < \sin^2 2\theta_{13} < 0.175 \quad \text{(normal hierarchy)},$$
$$0.038 < \sin^2 2\theta_{13} < 0.212 \quad \text{(inverted hierarchy)}.$$

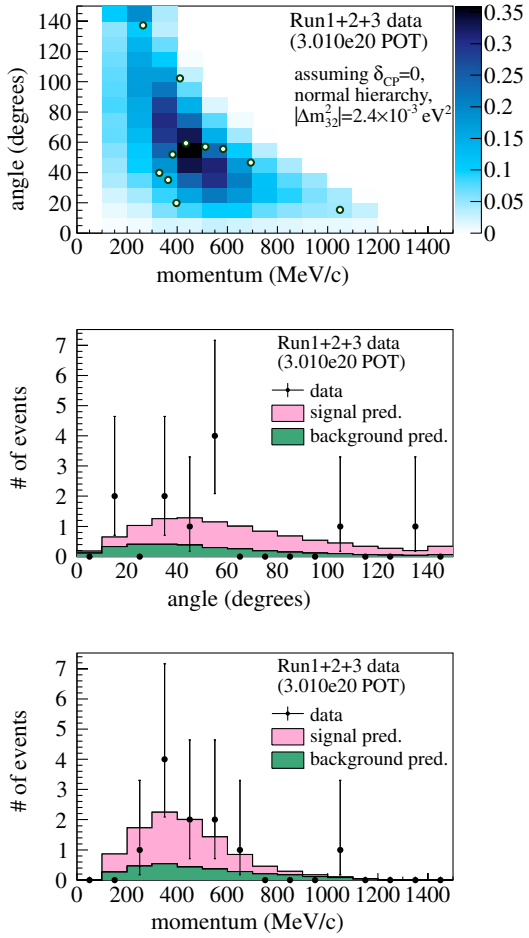

FIG. 35 (color online). The (p_e, θ_e) distribution of the ν_e events (dots) (top) overlaid with the prediction. The prediction includes the rate tuning determined from the fit to near detector information and a signal assuming the best-fit value of $\sin^2 2\theta_{13} = 0.088$. The angular distribution (middle) of the ν_e events in data overlaid with prediction, and the momentum distribution (bottom) with the same convention as above.

Figure 36 shows the 68% and 90% confidence intervals for $\sin^2 2\theta_{13}$ and the best-fit $\sin^2 2\theta_{13}$ for each value of δ_{CP}.

To compare the data with the best-fit (p_e, θ_e) distribution, assuming normal hierarchy and $\delta_{CP} = 0$, we perform the KS test. We reorder the 2D (p_e, θ_e) distribution into a 1D histogram, and generate 4000 toy MC experiments with the input value of $\sin^2 2\theta_{13} = 0.088$ (best-fit value) and where the observed number of events is 11. We then calculate the maximum distance for each toy experiment and determine the fraction of toy experiments for which the maximum distance is equal to or more than 0.22, the value obtained for a KS test done on data. The p value is 0.54 and therefore the (p_e, θ_e) distribution of data is consistent with the best-fit distribution.

Figure 36 shows the $-2\Delta \ln \mathcal{L}$ curve as a function of $\sin^2 2\theta_{13}$, for $\delta_{CP} = 0$. We consider an alternate test of the background hypothesis using the value of $-2\Delta \ln \mathcal{L}$ at

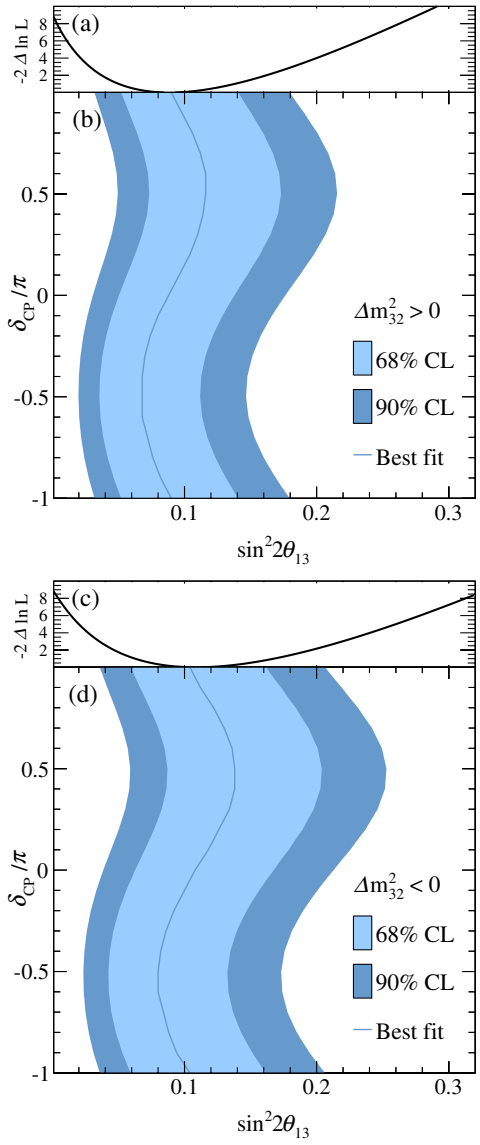

FIG. 36 (color online). The 68% and 90% confidence intervals for $\sin^2 2\theta_{13}$ scanned over values of δ_{CP} assuming normal hierarchy [top, (b)] and inverted hierarchy [bottom, (d)] with all other oscillation parameters fixed at the values in Table XIII. The best-fit value of $\sin^2 2\theta_{13}$ for each value of δ_{CP} is also shown for the (p_e, θ_e) analysis. The $-2\Delta \ln \mathcal{L}$ curve for normal hierarchy [top, (a)] and inverted hierarchy [bottom, (c)] at $\delta_{CP} = 0$ are also shown vs $\sin^2 2\theta_{13}$.

$\sin^2 2\theta_{13} = 0$. The probability of obtaining a $-2\Delta \ln \mathcal{L}$ at $\sin^2 2\theta_{13} = 0$ equal to or greater than the value observed in data, 8.8, is calculated using the distribution of $-2\Delta \ln \mathcal{L}$ from pseudoexperiments generated with $\sin^2 2\theta_{13} = 0$, $\delta_{CP} = 0$, normal hierarchy and fitted with the signal + background model. This test makes use of the different (p_e, θ_e) distributions of signal compared to background, assuming three active neutrino mixing, and yields a similar probability of 1×10^{-3} to the rate-only test presented earlier.

D. Alternate analysis methods

In addition to the (p_e, θ_e) analysis, we performed an analysis using the reconstructed neutrino energy spectrum, and a rate-only analysis. Since $E_\nu^{\rm rec}$ is closely correlated to the true neutrino energy for QE interactions, it provides the simplest projection for observing the energy dependence of the oscillation probability. This analysis also provides a consistency check of the use of spectral information in the fit. We also provide an update to the previous ν_e appearance analysis [21], where only rate information was used.

The likelihood including neutrino energy spectrum information is defined as

$$\mathcal{L}(\vec{o}, \vec{f}) = \mathcal{L}_{\rm norm}(\vec{o}, \vec{f}) \times \mathcal{L}_{\rm shape}(\vec{o}, \vec{f}) \times \mathcal{L}_{\rm syst}(\vec{f}). \quad (23)$$

In this analysis, we perform a one dimensional scan of $\sin^2 2\theta_{13}$ for each value of δ_{CP} while the other oscillation parameters are fixed. At each $\sin^2 2\theta_{13}$ point, the negative log likelihood $-2 \ln \mathcal{L}(\vec{o}, \vec{f})$ is minimized by allowing the nuisance parameters, $\vec{f}$, to vary. The best-fit value of $\sin^2 2\theta_{13}$ is the point where $-2 \ln \mathcal{L}(\vec{o})$ is minimized and $-2\Delta \ln \mathcal{L}$ is used to construct a confidence interval for $\sin^2 2\theta_{13}$ according to the Feldman-Cousins method.

Figure 37 shows the observed $E_\nu^{\rm rec}$ distribution for the ν_e events with the best-fit of the $E_\nu^{\rm rec}$ analysis applied. The observed spectrum agrees with the best-fit expectation, confirmed by a KS test with a p value of 0.7. The best-fit values of $\sin^2 2\theta_{13}$, assuming $\delta_{CP} = 0$, are

$$\sin^2 2\theta_{13} = 0.092^{+0.049}_{-0.039} \quad \text{(normal hierarchy)},$$
$$\sin^2 2\theta_{13} = 0.112^{+0.058}_{-0.047} \quad \text{(inverted hierarchy)}.$$

The 90% confidence intervals are

$$0.033 < \sin^2 2\theta_{13} < 0.179 \quad \text{(normal hierarchy)},$$
$$0.040 < \sin^2 2\theta_{13} < 0.215 \quad \text{(inverted hierarchy)}.$$

The rate-only measurement only uses the number of ν_e events at SK to determine $\sin^2 2\theta_{13}$. This analysis uses the normalization likelihood ratio:

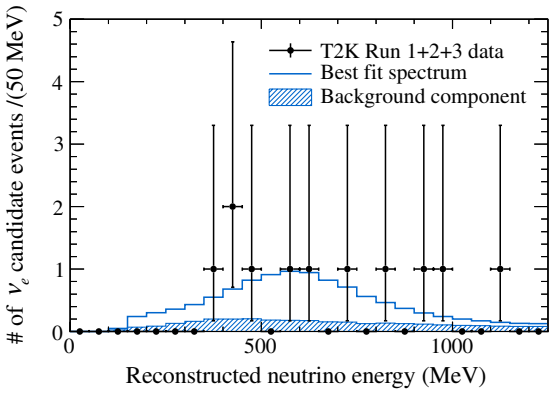

FIG. 37 (color online). The observed $E_\nu^{\rm rec}$ distribution and prediction, assuming $\sin^2 2\theta_{13} = 0.092$, $\delta_{CP} = 0$, and normal hierarchy. The background component is also shown.

$$\Delta\chi^2 = -2\log\frac{\mathcal{L}_{\rm norm}(\vec{o},\vec{f})}{\mathcal{L}^{\rm best}_{\rm norm}(\vec{o},\vec{f})}, \quad (24)$$

where $\mathcal{L}_{\rm norm}$ is defined in Eq. (20). The value of $\Delta\chi^2$ is calculated for the 11 observed ν_e candidates, in a one dimensional scan of $\sin^2 2\theta_{13}$ for each point of δ_{CP} with all other oscillation parameters fixed. The confidence intervals are determined using the Feldman-Cousins method.

The best-fit values of $\sin^2 2\theta_{13}$, assuming $\delta_{CP} = 0$, are

$$\sin^2 2\theta_{13} = 0.097^{+0.053}_{-0.041} \quad \text{(normal hierarchy)},$$
$$\sin^2 2\theta_{13} = 0.123^{+0.065}_{-0.051} \quad \text{(inverted hierarchy)}.$$

The 90% confidence intervals are

$$0.034 < \sin^2 2\theta_{13} < 0.190 \quad \text{(normal hierarchy)},$$
$$0.044 < \sin^2 2\theta_{13} < 0.236 \quad \text{(inverted hierarchy)}.$$

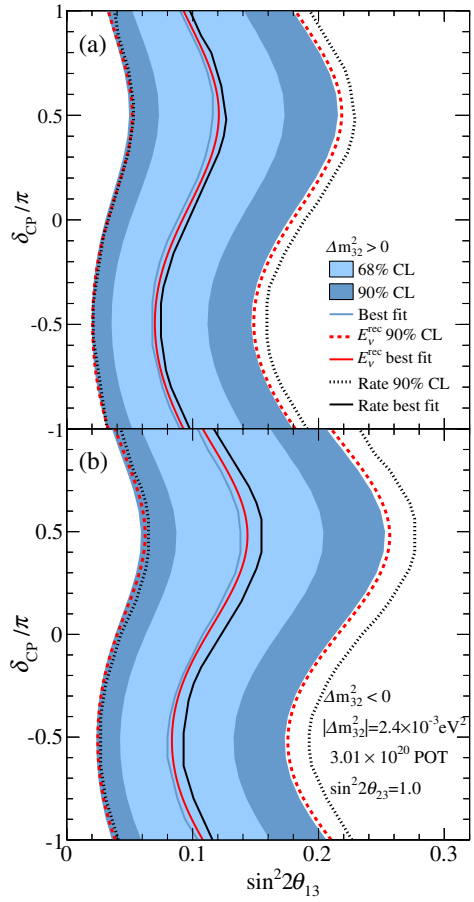

FIG. 38 (color online). The 68% and 90% confidence interval regions for $\sin^2 2\theta_{13}$ scanned over values of δ_{CP} assuming normal hierarchy (a) and inverted hierarchy (b) with the best-fit value of $\sin^2 2\theta_{13}$ shown for the (p_e, θ_e) analysis. The 90% confidence interval region for the $E_\nu^{\rm rec}$ analysis and rate-only analysis are overlaid. The best-fit values of $\sin^2 2\theta_{13}$ for the $E_\nu^{\rm rec}$ analysis and the rate-only analysis are also shown. All other oscillation parameters are fixed at the values in Table XIII.

Figure 38 shows the three analyses are consistent with each other. The rate-only analysis has a higher best-fit value of $\sin^2 2\theta_{13}$ than the $E_\nu^{\rm rec}$, (p_e, θ_e) analyses. This results from the additional discriminatory power of the kinematic information to identify events as slightly more similar to the background distribution than the predicted oscillation signal. In addition, the difference between the best-fit and the 90% upper confidence interval for the rate-only analysis is larger than the other two analyses. This is due to a slight (2%) overcoverage of the rate-only analysis.

X. CONCLUSION

In summary, we have reported the first evidence of electron neutrino appearance in a muon neutrino beam with a baseline and neutrino spectrum optimized for the atmospheric mass splitting. We observed 11 candidate ν_e events at the SK detector when 3.3 ± 0.4(syst) background events are expected, and rejected the background-only hypothesis with a p value of 0.0009, equivalent to a 3.1σ significance. We have employed a fit to the ND280 near detector data that constrains the parametrized neutrino flux and interaction models used to predict the event rates at SK. The ND280 constraint on the ν_e candidates reduced the overall systematic uncertainty to 10%–13% depending on the value of $\sin^2 2\theta_{13}$, an important step towards precision measurements of ν_e appearance. The excess of events at SK corresponds to a best-fit value of $\sin^2 2\theta_{13} = 0.088^{+0.049}_{-0.039}$ at 68% C.L., assuming $\delta_{CP} = 0$, $\sin^2 2\theta_{23} = 1.0$ and normal hierarchy.

This result represents an important step towards constraining the unknown parameters in the three-neutrino oscillation model. The evidence of electron neutrino appearance opens the door for a rich program of experimental physics in this oscillation channel. T2K measurements of this channel will be an important input to global fits which also combine muon neutrino disappearance measurements and reactor-based measurements of θ_{13} via $\bar{\nu}_e$ disappearance to begin to constrain δ_{CP} and the octant of θ_{23}. Future measurements of the appearance probability for antineutrinos will provide a further constraint on δ_{CP} and the mass hierarchy.

ACKNOWLEDGMENTS

We thank the J-PARC accelerator team for the superb accelerator performance and CERN NA61 colleagues for providing essential particle production data and for their fruitful collaboration. We acknowledge the support of MEXT, Japan; NSERC, NRC and CFI, Canada; CEA and CNRS/IN2P3, France; DFG, Germany; INFN, Italy; Ministry of Science and Higher Education, Poland; RAS, RFBR and the Ministry of Education and Science of the Russian Federation; MEST and NRF, South Korea; MICINN and CPAN, Spain; SNSF and SER,

Switzerland; STFC, U.K.; NSF and DOE, USA We also thank CERN for their donation of the UA1/NOMAD magnet and DESY for the HERA-B magnet mover system. In addition, participation of individual researchers and institutions in T2K has been further supported by funds from ERC (FP7), EU; JSPS, Japan; Royal Society, UK; DOE Early Career program, and the A. P. Sloan Foundation, USA Computations were performed on the supercomputers at the SciNet [115] HPC Consortium. SciNet is funded by the Canada Foundation for Innovation under the auspices of Compute Canada; the Government of Ontario; Ontario Research Fund - Research Excellence; and the University of Toronto.

APPENDIX: NEUT MODEL EXTERNAL DATA COMPARISONS AND TUNING

We fit external pion scattering data and neutrino scattering data with the NEUT model while allowing subsets of the systematic parameters described in Table IV to vary. These fits constrain the NEUT FSI, CCQE and resonant pion production models. The details of these fits are described here.

1. FSI model

The NEUT FSI model includes parameters which alter the pion interaction probabilities for absorption, charge exchange, and quasielastic scattering [78]. The values of these parameters and their uncertainties are determined from fits to pion scattering data. Figure 39 shows the tuned cascade model compared to macroscopic measurements of the pion absorption cross section and the maximum variation of the model parameters chosen to cover the uncertainties on the data.

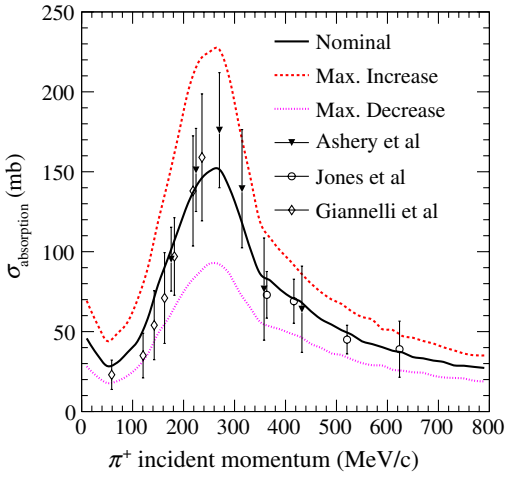

FIG. 39 (color online). Pion absorption cross section as a function of pion momentum overlaid with π^+-^{12}C scattering data, Ashery *et al.* [79], Jones *et al.* [80], and Giannelli *et al.* [81].

In total, we consider 16 variations of the FSI model parameters to cover the uncertainties on macroscopic pion scattering data. For each of the modified FSI parameter sets and the nominal NEUT model, we evaluate with weights the effect on ND280, SK or external predicted observables by calculating the covariance matrix of the predicted observables. FSI covariance matrices are generated for MiniBooNE, ND280 and SK predictions. The external data covariance matrices use observable bins from external data, such as reconstructed $(T_\mu, \cos\theta_\mu)$ bins for MiniBooNE. The ND280 covariance matrix corresponds to the two ND280 selections' reconstructed $(p_\mu, \cos\theta_\mu)$ bins and the SK covariance matrices correspond to the ν_e selection with either reconstructed (p_e, θ_e) or E_ν^{rec} bins:

$$V_{ij} = \frac{1}{16}\sum_{k=1}^{k=16}(p_i^{\text{nom}} - p_i^k)(p_j^{\text{nom}} - p_j^k), \qquad \text{(A1)}$$

where p_i^k is the expected event rate in the ith observable bin assuming the kth FSI parameter set, and p_i^{nom} is the expected event rate in the same bin assuming the nominal FSI parameter set. For the oscillation analysis, we add these FSI covariance matrices to the detector efficiency and reconstruction covariance matrices evaluated for ND280 (Sec. VI C) and SK (Sec. VIII) selections.

2. CCQE model

As discussed in Sec. V C 2, we fit the MiniBooNE measurement of the CCQE double-differential cross sections in bins of muon kinetic energy and angle $(T_\mu, \cos\theta_\mu)$ [82] with the NEUT model. While the CCQE model can be directly constrained with T2K ND280 data, we also fit the MiniBooNE measurement since the MiniBooNE detector's 4π acceptance provides coverage for backwards produced muons that are currently excluded in the ND280 selection.

To compare the NEUT model of CCQE interactions with MiniBooNE data, we use the MiniBooNE flux prediction [113] to generate CCQE interactions. We fit the MiniBooNE double-differential cross section data with the NEUT prediction, allowing M_A^{QE} and the overall cross section normalization to vary, by minimizing the χ^2 defined as

$$\chi^2(M_A^{\text{QE}}, \lambda) = \sum_{i=0}^{N}\left(\frac{D_i - \lambda M_i(M_A^{\text{QE}})}{\sigma_i}\right)^2 + \left(\frac{\lambda - 1}{\sigma_\lambda}\right)^2. \qquad \text{(A2)}$$

Here, the sum runs over the N bins in the $(T_\mu, \cos\theta_\mu)$ differential cross section, D_i is the cross section measured by MiniBooNE in the ith bin, M_i is the NEUT prediction in that bin and σ_i is the reported shape-only component of the error on the measured cross section. The second term adds a penalty to the normalization parameter λ, which is constrained within the MiniBooNE flux uncertainty, $\sigma_\lambda = 10.7\%$. The best-fit parameter values are

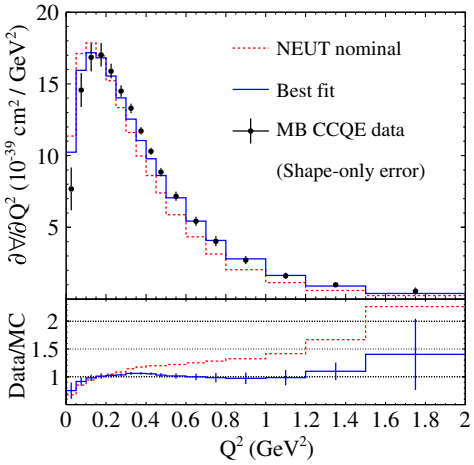

FIG. 40 (color online). The CCQE cross section as a function of Q^2 (top) as measured by MiniBooNE (points), with the NEUT nominal and NEUT at the best-fit of the MiniBooNE CCQE $(T_\mu, \cos\theta_\mu)$ spectrum. Ratio of data to NEUT (bottom) for nominal (dashed line) and best fit (solid line).

$M_A^{\mathrm{QE}} = 1.64 \pm 0.04$ GeV and $\lambda = 0.88 \pm 0.02$. Figure 40 shows the measured MiniBooNE cross section as a function of Q^2 for the nominal and best-fit value of M_A^{QE}, which is well reproduced except at lowest values of Q^2. However, this value of M_A^{QE} is significantly larger than the value of $M_A^{\mathrm{QE}} = 1.35 \pm 0.17$ GeV obtained by the MiniBooNE Collaboration in a fit to the single-differential $\mathrm{d}\sigma/\mathrm{d}Q^2$ spectrum, with an uncertainty that is smaller by a factor of 4. We postulate that the difference in central values is due to deficiencies in the nuclear

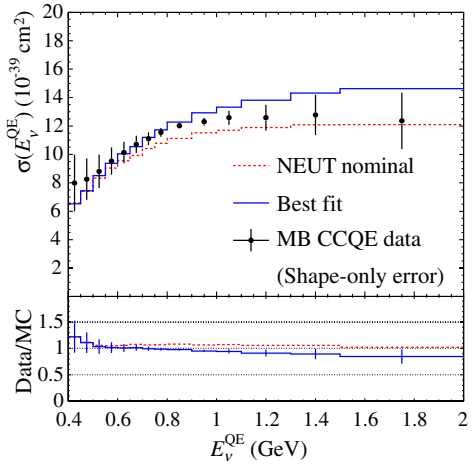

FIG. 41 (color online). The CCQE cross section as a function of neutrino energy (top) as measured by MiniBooNE (points), with the NEUT nominal and NEUT at the best fit of the MiniBooNE CCQE $(T_\mu, \cos\theta_\mu)$ spectrum. Ratio of data to NEUT (bottom) for nominal (dashed line) and best fit (solid line).

model at low Q^2, which MiniBooNE addressed by adding an empirical parameter κ to modify Pauli blocking, and the lack of full correlations between the measured $(T_\mu, \cos\theta_\mu)$ bins which are not included in the provided uncertainties. We assume the lack of bin correlations also causes the discrepancy in the fitted uncertainty, and this is supported by the relatively small $\chi^2 = 26.9$ that is observed for 137 degrees of freedom. Furthermore, the fitted prediction for the total CCQE cross section as a function of energy is poor, as illustrated in Fig. 41. The fitted model is systematically higher than the MiniBooNE data above 1 GeV, although agreement is improved near the T2K peak energy of 600 MeV.

As is discussed in Sec. VI, a CCQE-like selection of interactions in ND280 has power to constrain the CCQE cross section model. Since the fit to MiniBooNE data poorly reproduces the energy dependent cross section and lacks the full correlation of data points, we do not directly tune the NEUT model with the fitted value for M_A^{QE}. Instead, we set large prior uncertainties on the CCQE model parameters and allow the ND280 data to constrain the model. We set M_A^{QE} to the NEUT nominal value (1.21 GeV), with the prior uncertainty set to the difference between the nominal value and best-fit value from the MiniBooNE fit, viz. $(1.64 - 1.21 = 0.43)$ GeV. We set the uncertainty on the low energy CCQE normalization, x_1^{QE}, to the size of the MiniBooNE flux uncertainty (11%).

3. Single pion production model

As discussed in Sec. V C 3 we consider measurements of single pion production cross sections on light nuclei in the T2K energy range by MiniBooNE [91–93], and K2K [94]. We perform a joint fit to the MiniBooNE measurements of charged current single π^+ production (CC1π^+), charged current single π^0 production (CC1π^0) and neutral current single π^0 production (NC1π^0), and we check the fit results with the K2K measurement.

An important feature of the MiniBooNE single pion measurements is that they are defined by the particles exiting the target nucleus, not the particles produced at the neutrino interaction vertex. The measurements do not include corrections for FSI, but do include uncertainties of interactions of the pions in the detector. To derive the NEUT predictions for these selections, we generate interactions according to the MiniBooNE flux as was done for the CCQE fits. Instead of selecting generated events based on the true neutrino interaction mode, such as CC1π^+, we select the events based on the presence of a single pion exiting the nucleus. Hence, multiple interaction types are present in the prediction for each of the MiniBooNE measurements. For example, CC1π^+ interactions chiefly result in a single charged pion exiting the nucleus, but these events may instead pass the CC1π^0 selection if π^+ undergoes single charge exchange within the nucleus.

This interdependence within the MiniBooNE selections, as well as the fact that all three are predicted by the same model in NEUT, justifies the use of a joint fit to the three measurements.

We fit to the measured $d\sigma/dQ^2$ spectra from CC1π^+ and CC1π^0 samples and the $d\sigma/dp_{\pi^0}$ spectrum from the NC1π^0 samples. MiniBooNE provides uncertainties for each of the measurements. In the case of the CC1π^0 and NC1π^0 measurements, covariance matrices account for correlations between the measured points in the spectra arising from the MiniBooNE flux model and detector response. MiniBooNE only provides diagonal errors for the CC1π^+ measurement. We construct a covariance matrix for the CC1π^+ by assuming a 10% flux uncertainty correlated across all bins and by adding an additional uncorrelated uncertainty to the diagonal terms to recover the diagonal errors provided by MiniBooNE. While the flux is shared for the three measurements, at this time no correlation between the three measurements was considered.

For each of the three measured distributions (k) we construct the χ^2 based on the data and NEUT prediction:

$$\chi^2_k = \sum_i \sum_j [D^k_i - M^k_i(\vec{x})](C^k_{ij})^{-1}[D^k_j - M^k_j(\vec{x})]. \quad \text{(A3)}$$

Here, i and j sum over the bins in the kth measurement, D^k_i are the measured differential cross sections, C^k_{ij} is the covariance matrix describing the uncertainty on the measurement and $M^k_i(\vec{x})$ are the NEUT predictions for each measurement.

The cross section parameters that are allowed to vary in the fit, $\vec{x}$, along with their prior values and prior uncertainties for penalty terms are listed in Table V. Contributions to the predictions from CC multipion/DIS ($x_{\text{CC other}}$) interactions, NC coherent interactions, NC1$\pi^\pm$ interactions and NC multipion/DIS interactions are relatively small, so penalty terms are used for the associated parameters according to the prior uncertainties.

We minimize the total χ^2 that includes the χ^2 for each of the measurements and the penalty terms:

$$\chi^2_{\text{total}} = \chi^2_{\text{CC1}\pi^+} + \chi^2_{\text{CC1}\pi^0} + \chi^2_{\text{NC1}\pi^0} + \sum_k \frac{(s_k - s^{\text{nom}}_k)^2}{\sigma^2_k}, \quad \text{(A4)}$$

where, for each penalized parameter k, s_k is the value of the parameter, s^{nom}_k is the nominal value, and σ_k is the prior uncertainty assigned to the penalty parameter.

In practice, the inclusion of the NC1π^0 covariance matrix in the fit results in a best fit which lies outside the range of the data points. This behavior results from strongly correlated measurements combined with a model which does not correctly describe the data [114]. To achieve a fit that better reproduces the central values of the data points, we only use the diagonal terms of the NC1π^0 covariance matrix in our fit. The missing correlations also result in uncertainties on the fit parameters which do not cover the uncertainties in the data points. To remedy this, we multiply the fit parameter uncertainties by a scale factor of 2 (2.5) for CC (NC) parameters, while keeping their correlations the same. These scale factors ensure that the flux-integrated cross section uncertainty matches that given by MiniBooNE (16% for each measurement).

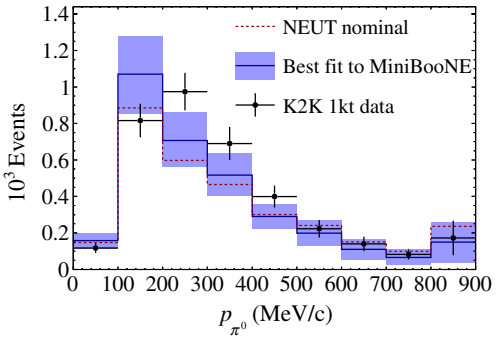

FIG. 42 (color online). Differential $d\sigma/dp_{\pi^0}$ cross section measured by K2K and the nominal and best fit from the MiniBooNE single pion fits NEUT predictions, with error band showing the uncertainties after the fit to MiniBooNE data.

The results of the fit are discussed in Sec. V C 3. We propagate the fitted values and uncertainties for M^{RES}_A, $x^{\text{CC1}\pi}_1$ and $x^{\text{NC1}\pi^0}$ to model the cross section in the fit to ND280 data described in Sec. VII. In addition, we keep parameter W_{eff} at its nominal value, but assign an uncertainty equal to the difference between the best fit value and the nominal value.

We compare the results of the fitted NEUT pion production model to the NC K2K measurement. The $d\sigma/dp_{\pi^0}$ distribution measured by K2K in the 1000 ton water Cherenkov detector is shown with the nominal and tuned NEUT model in Fig. 42. As with the MiniBooNE data, the data prefer a peak at higher momentum and fewer events in the high momentum tail compared to the nominal NEUT prediction. The use of NEUT assuming the best-fit parameters from the MiniBooNE single pion production fits does not significantly improve the agreement between NEUT and the K2K data. However, the discrepancy is covered by the uncertainties on the single pion production and FSI model.

[1] B. Cleveland, T. Daily, R. Davis, Jr., J. R. Distel, K. Lande, C. K. Lee, P. S. Wildenhain, and J. Ullman, Astrophys. J. **496**, 505 (1998).
[2] K. S. Hirata *et al.* (Kamiokande-II Collaboration), Phys. Rev. Lett. **63**, 16 (1989).
[3] J. Abdurashitov *et al.* (SAGE Collaboration), Phys. Lett. B **328**, 234 (1994).
[4] P. Anselmann *et al.* (GALLEX Collaboration), Phys. Lett. B **327**, 377 (1994).
[5] S. Fukuda *et al.* (Super-Kamiokande Collaboration), Phys. Rev. Lett. **86**, 5651 (2001).
[6] Q. R. Ahmad *et al.* (SNO Collaboration), Phys. Rev. Lett. **89**, 011301 (2002).
[7] C. Arpesella *et al.* (Borexino Collaboration), Phys. Rev. Lett. **101**, 091302 (2008).
[8] Y. Fukuda *et al.* (Super-Kamiokande Collaboration), Phys. Lett. B **436**, 33 (1998).
[9] K. Hirata *et al.*, Phys. Lett. B **205**, 416 (1988).
[10] R. Becker-Szendy *et al.*, Phys. Rev. D **46**, 3720 (1992).
[11] S. Ahlen *et al.*, Phys. Lett. B **357**, 481 (1995).
[12] W. Allison *et al.*, Phys. Lett. B **391**, 491 (1997).
[13] R. Wendell *et al.* (Super-Kamiokande Collaboration), Phys. Rev. D **81**, 092004 (2010).
[14] S. Abe *et al.* (KamLAND Collaboration), Phys. Rev. Lett. **100**, 221803 (2008).
[15] M. H. Ahn *et al.* (K2K Collaboration), Phys. Rev. D **74**, 072003 (2006).
[16] P. Adamson *et al.* (MINOS Collaboration), Phys. Rev. Lett. **108**, 191801 (2012).
[17] P. Adamson *et al.* (MINOS Collaboration), Phys. Rev. Lett. **106**, 181801 (2011).
[18] K. Abe *et al.* (T2K Collaboration), Phys. Rev. D **85**, 031103 (2012).
[19] A. A. Aguilar-Arevalo *et al.* (LSND Collaboration), Phys. Rev. D **64**, 112007 (2001).
[20] A. Aguilar-Arevalo *et al.* (MiniBooNE Collaboration), Phys. Rev. Lett. **105**, 181801 (2010).
[21] K. Abe *et al.* (T2K Collaboration), Phys. Rev. Lett. **107**, 041801 (2011).
[22] N. Agafonova *et al.* (OPERA Collaboration), Phys. Lett. B **691**, 138 (2010).
[23] K. Abe *et al.* (Super-Kamiokande Collaboration), Phys. Rev. Lett. **110**, 181802 (2013).
[24] M. Apollonio *et al.* (CHOOZ Collaboration), Eur. Phys. J. C **27**, 331 (2003).
[25] P. Adamson *et al.* (MINOS Collaboration), Phys. Rev. Lett. **107**, 181802 (2011).
[26] P. Adamson *et al.* (MINOS Collaboration), Phys. Rev. Lett. **110**, 171801 (2013).
[27] J. Beringer *et al.* (Particle Data Group), Phys. Rev. D **86**, 010001 (2012).
[28] F. P. An *et al.* (Daya Bay Collaboration), Phys. Rev. Lett. **108**, 171803 (2012).
[29] J. K. Ahn *et al.* (RENO Collaboration), Phys. Rev. Lett. **108**, 191802 (2012).
[30] Y. Abe *et al.* (Double Chooz Collaboration), Phys. Rev. Lett. **108**, 131801 (2012).
[31] M. Freund, Phys. Rev. D **64**, 053003 (2001).
[32] K. Abe *et al.* (T2K Collaboration), Nucl. Instrum. Methods Phys. Res., Sect. A **659**, 106 (2011).
[33] D. Beavis *et al.*, Technical Report No. 52459, BNL, 1995.
[34] A. K. Mann, *Prepared for 3rd NESTOR Workshop, Pylos, Greece, 1993.*
[35] R. L. Helmer, *Proceedings of the 9th Lake Louise Winter Institute, Lake Louise, Canada, 1994*, edited by A. Astbury *et al.* (World Scientific, Singapore, 1995), p. 291.
[36] M. Otani *et al.*, Nucl. Instrum. Methods Phys. Res., Sect. A **623**, 368 (2010).
[37] K. Abe *et al.* (T2K Collaboration), Nucl. Instrum. Methods Phys. Res., Sect. A **694**, 211 (2012).
[38] S. Aoki *et al.*, Nucl. Instrum. Methods Phys. Res., Sect. A **698**, 135 (2013).
[39] S. Assylbekov *et al.*, Nucl. Instrum. Methods Phys. Res., Sect. A **686**, 48 (2012).
[40] P. Amaudruz *et al.* (T2K ND280 FGD Collaboration), Nucl. Instrum. Methods Phys. Res., Sect. A **696**, 1 (2012).
[41] N. Abgrall *et al.* (T2K ND280 TPC Collaboration), Nucl. Instrum. Methods Phys. Res., Sect. A **637**, 25 (2011).
[42] Y. Fukuda *et al.* (Super-Kamiokande Collaboration), Nucl. Instrum. Methods Phys. Res., Sect. A **501**, 418 (2003).
[43] D. W. Allan and M. A. Weiss, *Proceedings of the 34th Annual Symposium on Frequency Control, 1980*, p. 334 (unpublished).
[44] K. Abe *et al.* (T2K Collaboration), Phys. Rev. D **87**, 012001 (2013).
[45] N. Abgrall *et al.* (NA61/SHINE Collaboration), Phys. Rev. C **84**, 034604 (2011).
[46] N. Abgrall *et al.* (NA61/SHINE Collaboration), Phys. Rev. C **85**, 035210 (2012).
[47] A. Ferrari, P. R. Sala, A. Fasso, and J. Ranft, Reports No. CERN-2005-010, No. SLAC-R-773, and No. INFN-TC-05-11.
[48] G. Battistoni, F. Cerutti, A. Fasso, A. Ferrari, S. Muraro, J. Ranft, S. Roesler, and P. R. Sala, AIP Conf. Proc. **896**, 31 (2007); we used FLUKA2008, which was the latest version at the time of this study. A new version, FLUKA2011, has been already released now and the comparison with data would be different.
[49] R. Brun, F. Carminati, and S. Giani, CERN Report No. CERN-W5013, 1994.
[50] C. Zeitnitz and T. A. Gabriel, Nucl. Instrum. Methods Phys. Res., Sect. A **349**, 106 (1994).
[51] S. Bhadra *et al.*, Nucl. Instrum. Methods Phys. Res., Sect. A **703**, 45 (2013).
[52] K. McDonald and D. Russell, Lect. Notes Phys. **343**, 122 (1989).
[53] T. Eichten *et al.*, Nucl. Phys. **B44**, 333 (1972).
[54] J. V. Allaby *et al.*, CERN Technical Report No. 70-12, 1970.
[55] I. Chemakin *et al.* (E910 Collaboration), Phys. Rev. C **77**, 015209 (2008).
[56] R. J. Abrams, R. Cool, G. Giacomelli, T. Kycia, B. Leontic, K. Li, and D. Michael, Phys. Rev. D **1**, 1917 (1970).
[57] J. Allaby *et al.*, Phys. Lett. **30B**, 500 (1969).
[58] B. Allardyce *et al.*, Nucl. Phys. **A209**, 1 (1973).
[59] G. Bellettini, G. Cocconi, A. N. Diddens, E. Lillethun, G. Matthiae, J. P. Scanlon, and A. M. Wetherell, Nucl. Phys. **79**, 609 (1966).
[60] B. M. Bobchenko *et al.*, Sov. J. Nucl. Phys. **30**, 805 (1979).
[61] A. Carroll *et al.*, Phys. Lett. **80B**, 319 (1979).

[62] J. W. Cronin, R. Cool, and A. Abashian, Phys. Rev. **107**, 1121 (1957).
[63] F. F. Chen, C. P. Leavitt, and A. M. Shapiro, Phys. Rev. **99**, 857 (1955).
[64] S. Denisov, S. V. Donskov, Y. P. Gorin, R. N. Krasnokutsky, A. I. Petrukhin, Y. D. Prokoshkin, and D. A. Stoyanova, Nucl. Phys. **B61**, 62 (1973).
[65] M. J. Longo and B. J. Moyer, Phys. Rev. **125**, 701 (1962).
[66] A. V. Vlasov *et al.*, Sov. J. Nucl. Phys. **27**, 222 (1978).
[67] R. P. Feynman, Phys. Rev. Lett. **23**, 1415 (1969).
[68] Y. Hayato, Acta Phys. Pol. B **40**, 2477 (2009).
[69] C. Llewellyn Smith, Phys. Rep. **3**, 261 (1972).
[70] R. Smith and E. Moniz, Nucl. Phys. **B43**, 605 (1972).
[71] R. Smith and E. Moniz, Nucl. Phys. **B101**, 547(E) (1975).
[72] D. Rein and L. M. Sehgal, Annals Phys. **133**, 79 (1981).
[73] M. Gluck, E. Reya, and A. Vogt, Eur. Phys. J. C **5**, 461 (1998).
[74] M. Nakahata *et al.* (KAMIOKANDE Collaboration), J. Phys. Soc. Jpn. **55**, 3786 (1986).
[75] T. Sjostrand, Comput. Phys. Commun. **82**, 74 (1994).
[76] A. Bodek and U. Yang, arXiv:hep-ex/0308007.
[77] L. Salcedo, E. Oset, M. Vicente-Vacas, and C. Garcia-Recio, Nucl. Phys. **A484**, 557 (1988).
[78] P. de Perio, AIP Conf. Proc. **1405**, 223 (2011).
[79] D. Ashery, I. Navon, G. Azuelos, and F. W. Schlepütz, Phys. Rev. C **23**, 2173 (1981).
[80] M. K. Jones *et al.*, Phys. Rev. C **48**, 2800 (1993).
[81] R. A. Giannelli *et al.*, Phys. Rev. C **61**, 054615 (2000).
[82] A. A. Aguilar-Arevalo *et al.* (MiniBooNE Collaboration), Phys. Rev. D **81**, 092005 (2010).
[83] V. Lyubushkin *et al.* (NOMAD Collaboration), Eur. Phys. J. C **63**, 355 (2009).
[84] M. Martini, M. Ericson, G. Chanfray, and J. Marteau, Phys. Rev. C **80**, 065501 (2009).
[85] M. Martini, M. Ericson, G. Chanfray, and J. Marteau, Phys. Rev. C **81**, 045502 (2010).
[86] J. Amaro, M. Barbaro, J. Caballero, T. Donnelly, and C. Williamson, Phys. Lett. B **696**, 151 (2011).
[87] A. Bodek, H. Budd, and M. Christy, Eur. Phys. J. C **71**, 1 (2011).
[88] J. Nieves, I. R. Simo, and M. V. Vacas, Phys. Lett. B **707**, 72 (2012).
[89] D. Meloni and M. Martini, Phys. Lett. B **716**, 186 (2012).
[90] O. Lalakulich, U. Mosel, and K. Gallmeister, Phys. Rev. C **86**, 054606 (2012).
[91] A. A. Aguilar-Arevalo *et al.* (MiniBooNE Collaboration), Phys. Rev. D **83**, 052007 (2011).
[92] A. A. Aguilar-Arevalo *et al.* (MiniBooNE Collaboration), Phys. Rev. D **83**, 052009 (2011).
[93] A. A. Aguilar-Arevalo *et al.* (MiniBooNE Collaboration), Phys. Rev. D **81**, 013005 (2010).
[94] S. Nakayama *et al.* (K2K Collaboration), Phys. Lett. B **619**, 255 (2005).
[95] T. Golan, C. Juszczak, and J. T. Sobczyk, Phys. Rev. C **86**, 015505 (2012).
[96] Q. Wu *et al.* (NOMAD Collaboration), Phys. Lett. B **660**, 19 (2008).
[97] M. Hasegawa *et al.* (K2K Collaboration), Phys. Rev. Lett. **95**, 252301 (2005).
[98] K. Hiraide *et al.* (SciBooNE Collaboration), Phys. Rev. D **78**, 112004 (2008).
[99] Y. Kurimoto *et al.* (SciBooNE Collaboration), Phys. Rev. D **81**, 111102 (2010).
[100] P. Musset and J.-P. Vialle, Phys. Rep. **39**, 1 (1978).
[101] J. E. Kim, P. Langacker, M. Levine, and H. H. Williams, Rev. Mod. Phys. **53**, 211 (1981).
[102] P. Adamson *et al.* (MINOS Collaboration), Phys. Rev. D **81**, 072002 (2010).
[103] E. Moniz, I. Sick, R. Whitney, J. Ficenec, R. Kephart, and W. Trower, Phys. Rev. Lett. **26**, 445 (1971).
[104] A. M. Ankowski and J. T. Sobczyk, Phys. Rev. C **74**, 054316 (2006).
[105] M. Day and K. S. McFarland, Phys. Rev. D **86**, 053003 (2012).
[106] S. Agostinelli *et al.*, Nucl. Instrum. Methods Phys. Res. Sect. A **506**, 250 (2003).
[107] J. Allison *et al.*, IEEE Trans. Nucl. Sci. **53**, 270 (2006).
[108] S. Baker and R. D. Cousins, Nucl. Instrum. Methods Phys. Res. **221**, 437 (1984).
[109] Y. Ashie *et al.* (Super-Kamiokande Collaboration), Phys. Rev. D **71**, 112005 (2005).
[110] T. Barszczak, Ph.D. thesis, University of California, Irvine, 2005.
[111] V. D. Barger, K. Whisnant, S. Pakvasa, and R. Phillips, Phys. Rev. D **22**, 2718 (1980).
[112] G. J. Feldman and R. D. Cousins, Phys. Rev. D **57**, 3873 (1998).
[113] A. A. Aguilar-Arevalo *et al.* (MiniBooNE Collaboration), Phys. Rev. D **79**, 072002 (2009).
[114] G. D'Agostini, Nucl. Instrum. Methods Phys. Res., Sect. A **346**, 306 (1994).
[115] D. G. C. Loken *et al.*, J. Phys. Conf. Ser. **256**, 012026 (2010).